ETH zürich

Diss. ETH No. 27234

Ice spheres in snow mechanics: microstructural analyses, experiments, and simulations

A thesis submitted to attain the degree of
DOCTOR OF SCIENCES of ETH ZURICH
(Dr. sc. ETH Zurich)

presented by

Carolin Laura Willibald
M.Sc. Physics, Albert-Ludwigs-Universität Freiburg
born on December 26th, 1987
citizen of the Federal Republic of Germany

accepted on the recommendation of
Prof. Dr. Jürg Dual, examiner
Prof. Dr. Johan Gaume, co-examiner
Dr. Henning Löwe, co-examiner
Dr. Martin Schneebeli, co-examiner

2021

Let us go out
and enjoy the snow, until
we tumble over.

— Bashō

Contents

Abstract

Fast deformations of snow are relevant for many snow mechanical applications, such as understanding avalanche formation, avalanche dynamics, and mobility in snow. During fast deformation, snow typically undergoes fracture and has to be treated therefore as both a sintered and granular material. These large deformation processes can conveniently be studied with the Discrete Element Method (DEM), in which the material is commonly represented by spherical particles. This constitutes a fundamental problem of how the complex, non-spherical microstructure of snow can be mapped onto spheres with suitable particle and contact properties to facilitate model validation by experiments.

The present thesis addressed this problem by designing and analyzing a spherical model snow type, referred to as ice beads, as an experimental realization of "true" sphere microstructures required in DEM models. The new snow type was mechanically and structurally characterized in the sintered as well as in the granular state with focus on particle and contact properties. The work combined microstructure characterization through X-ray tomography image analysis, mechanical compression and angle of repose experiments, sintering experiments, and DEM simulations to assess the potential of ice beads for validation of micromechanical DEM snow models. The analyses were carried out in four steps and included prominent natural snow types for comparison.

To reduce experimental uncertainties, particles with highly spherical shapes were needed. A new method was developed for producing ice beads, to meet the requirements of very round particles. With an automated routine, particles and contacts could be objectively determined in 3D X-ray tomography images. This was the basis for detailed analyses and an efficient microstructure reconstruction in DEM.

Particle shape was used as a parameter to explain the differences in granular dynamics between natural snow and spherical particles, i.e. ice beads or DEM particles. In angle of repose experiments it was shown that sintering during short contact times (seconds) does indeed influence granular dynamics of snow. The experiments could be well explained by an empirical model based on shape and sintering (temperature).

The strength and deformation of sintered snow are determined by inter-particle contacts. This relation was investigated in unconfined compression experiments of sintered samples. The sintered contacts of the samples should have been fully determined in the 3D tomography images, however, the discovered porosity in the contacts inhibited the quantification of contact sizes. The porosity was explained as an instable growth process during sintering that depends on particle size. This particle-size-dependence was investigated in a detailed analysis of the sintering process in ice bead samples to examine the sizes for which porous bonds can be avoided in future experiments. An improved estimate of the contacts by higher-resolution tomography was derived, which was key for the DEM validation.

Eventually, the compression tests were simulated in DEM models. Based on the 3D X-ray images of the ice bead samples, identical microstructures could be examined in experiments and DEM simulations for the first time. The results revealed that the microstructures must be reconstructed in models with a high degree of detail; particularly important are the contacts which represent a key component of the microstructure. If the microstructures are adequately simulated, models can reproduce experimental observations by only using experimentally constrained particle and contact parameters in the DEM model. For a more detailed comparison between experiments and simulations the porosity in the contacts should be avoided in future experiments.

The results of the thesis show that the simplified microstructures of ice beads facilitate the validation of micromechanical properties required for DEM modeling, like particles (size and shape) and contacts, in the sintered and granular state. This is an essential step towards faithfully simulating natural snow in DEM. The outlook comprises suggestions for future improvements, particularly in view of simulating natural snow.

Zusammenfassung

Schnelle Verformung von Schnee ist relevant für die meisten Anwendungsgebiete der Schneemechanik, zum Beispiel für das Verständnis von Lawinenentstehung und -dynamik, oder zur Optimierung von Mobilität in Schnee. Während schneller Verformung kommt es meistens zu Bruch im Schnee, weshalb er sowohl als gesintertes als auch als granulares Material betrachtet werden muss. Für numerische Simulationen solcher Prozesse eignet sich die Diskrete Elemente Methode (DEM), in der das Material üblicherweise mit Kugeln dargestellt wird. Daraus ergibt sich die zentrale Frage, wie komplex geformte Schneemikrostrukturen durch Kugeln mit entsprechenden Partikel- und Kontakteigenschaften dargestellt werden können, um DEM Modelle mit Experimenten zu validieren.

Dieses Problem wurde in der vorliegenden Doktorarbeit angegangen, indem Eiskügelchen als eine neue Schneeart eingeführt wurden, mit welchen typische DEM Mikrostrukturen experimentell untersucht werden konnten. Um das Potenzial diese Modellschnees für die Validierung mikromechanischer DEM Modelle zu ermitteln, wurde er strukturell und mechanisch sowohl im granularen als auch im gesinterten Zustand charakterisiert, mit Schwerpunkt auf Partikel- und Kontakteigenschaften. Die Mikrostrukturen wurden durch Röntgentomographiebilder (3D-CT-Bilder) analysiert und mechanische Kompressions- und Schüttwinkelexperimente, sowie extra Sinterexperimente und DEM Simulationen wurden durchgeführt. Zum Vergleich wurde auch natürlicher Schnee untersucht.

Um die experimentellen Unsicherheiten so gering wie möglich zu halten, war die Rundheit der Partikel massgeblich. Zur Herstellung möglichst kugelförmiger Eisteilchen wurde eine neue Methode entwickelt. Die Partikel und Kontakte konnten automatisiert in den 3D-CT-Bildern bestimmt werden, was für alle weiteren Forschungsfragen essentiell war.

In den Experimenten zur Charakterisierung von granularem Schnee war die Partikelform entscheidend. Damit liessen sich Unterschiede in den Fliesseigenschaften von natürlichem Schnee und den Eiskügelchen, bzw. den runden DEM Partikeln, erklären. Weiterhin konnte in den Schüttwinkelexperimenten nachgewiesen werden, dass Sintern auch während kurzen (Sekunden) Kontaktzeiten auftritt und die Fliesseigenschaften von Schnee beeinflusst. Diese Experimente konnten mit beiden Einflussfaktoren, Partikelform und Sintern, durch ein empirisches Modell erklärt werden.

Für die Festigkeit und Verformbarkeit von gesintertem Schnee sind die gesinterten Kontakte zwischen Partikeln ausschlaggebend, was in Kompressionsexperimenten untersucht wurde. Die gesinterten Kontakte sollten in den 3D-CT-Bildern der experimentellen Proben quantifiziert werden, was jedoch durch die unerwartete Porösität in den Kontakten nicht möglich war. Diese Porösität wurde auf eine Instabilität im Kristallwachstum während des Sinterns zurückgeführt, die ab einer gewissen Partikelgrösse auftritt. In einer detaillierten Analyse des Sinterprozesses wurde untersucht, mit welchen Partikelgrössen poröse Kontakte in zukünftigen Experimenten vermieden werden können. Zudem konnte aus den hochaufgelösten 3D-CT-Bildern ein Mass für die Kontaktflächen bestimmt und für die Modellvalidierung verwendet werden.

Schlussendlich wurden die Kompressionstests in DEM-Modellen simuliert. Mithilfe der 3D-CT-Bilder der Eiskügelchen konnten erstmals identische Mikrostrukturen in Experimenten und DEM-Simulationen untersucht werden. Dabei wurde deutlich, dass die Mikrostrukturen sehr detailgetreu rekonstruiert werden müssen und insbesondere die Kontakte zwischen den Partikeln einen zentralen Aspekt der Mikrostruktur darstellen. Gelingt es die Kontakte gut zu simulieren, können experimentelle Details in den Simulationen abgebildet werden, basierend auf experimentell bestimmten Partikel- und Kontakteigenschaften. Für einen detaillierteren Vergleich von Simulationen und Experimenten müssen die porösen Kontakte künftig vermieden werden.

In dieser Arbeit wurde gezeigt, dass die vereinfachten, wohldefinierten Mikrostrukturen der Eiskügelchen die Validierung mikomechanischer DEM modelle ermöglichen. Dies ist ein wichtiger Schritt um auch natürlichen Schnee zuverlässig mit DEM simulieren zu können. Der Ausblick beinhaltet Vorschläge für weitere Verbesserungen, insbesondere bezüglich Simulationen von natürlichem Schnee.

1 Introduction

Snow fascinates with its tiny crystals of marvelous beauty that together can change our landscape overnight. Why can we build a snowman on one day but not on another day? Why do we get a sunburn in snow more easily? Why can we build an igloo that keeps us warm in a cold winter night? Why is fluffy powder often just a one-day pleasure? Why are avalanches so difficult to predict? And why is snow so important for the climate on earth?

Answers to these questions originate in the warm temperature of snow that makes it fascinating also from a scientific point of view. Material scientists classify snow as a hot material, since it is always close to the melting point. This has large implications on the properties of snow: snow changes its shape rapidly and forms different structures which we experience as different snow types with different properties; snow sinters and connects individual snow crystals to a complex microstructure. That these processes occur under natural conditions and on relatively short time-scales, during minutes, hours, and days, makes snow an ambivalent material. On one hand, observing processes like sintering is much easier in snow than in other materials such as metals, which exhibit similar behavior only at uncomfortable temperatures of several hundred to over thousand degree Celsius. On the other hand, snow always changes its shape and physical properties within very short times such that these changes cannot be neglected and make it difficult to predict the behavior of snow.

For a detailed and accurate description of the material properties of snow, the complex and quickly changing microstructure of snow has to be explicitly taken into account. The geometry of the microstructure and the material properties of ice together determine the thermal, optical, and mechanical properties of snow. The optical properties are impor-

tant, for example, for remote sensing of snow and the prediction of snow melt; thermal properties of snow are relevant for its insulating effect on sea ice, permafrost, animals and plants beneath the snow; mechanical properties of snow are important for avalanche prediction and protection, construction of infrastructures (roads, houses, bridges), handling snow in piste preparation or road clearing. The present thesis focuses on the latter topic, snow mechanics, and its microstructural foundation.

1.1 Snow mechanics

The goal of snow mechanics is to understand the response of snow under load for predicting deformation and failure of the material. Research on snow mechanics dates back to the 1930s [5], when first experiments were performed to establish constitutive relations of snow. Since then, research has been motivated by the need to understand and predict avalanches, to create adequate infrastructures, or to optimize mobility on snow in designing appropriate car tires or a perfect ski wax.

Diverse factors strongly influence the mechanical behavior of snow. The density has a strong influence, which is obvious to anybody who experiences snow - imagine soft, freshly fallen snow, or dense, almost icy firn. Snow is often considered as a foam of ice [55], where the porosity ranges from 90 - 20% air (fresh snow to dense firn). Given this wide range, density is a primary indicator for mechanical properties [78, 105]. Besides density, the mechanical behavior of snow strongly depends on deformation rates: at low deformation rates, snow can sustain considerable strains and stresses while deforming in a ductile manner; in contrast, at high deformation rates only small strains and stresses can be reached before brittle failure. The so-called ductile-brittle-transition occurs at strain-rates between 10^{-4} and $10^{-3}\,\mathrm{s}^{-1}$, depending on temperature [86, 103]. The temperature and strain rate dependence are in principle coupled [55]. These three examples (density, strain rate, temperature) indicate the large parameter space that has to be considered for the investigation of snow behavior. Many experiments have been conducted to investigate the relations between stress and strain and to formulate failure criteria, which were summarized in the review papers [78, 90, 99, 105].

Snow mechanical approaches can be classified into two categories [105]. The experiments mentioned above belong to the first category, which comprises experiments in which behavior of snow is observed and described at the macro-scale, in order to find values for the parameters of the constitutive equations. However, the validity is limited to the respective experimental conditions (e.g. density, strain rates, temperature etc.). The second category comprises experiments that consider snow microstructure in order to understand micromechanical processes to predict macromechanical behavior. This approach is able to actually explain or derive the macro-scale behavior from the microstructure that is valid, in the best of all worlds for all snow types and possible conditions. In addition, the latter approach significantly widens the interest and relevance of snow mechanics, because it can be compared to other materials. Both categories of experiments and approaches are required to derive homogenized, macroscale descriptions of snow in terms of constitutive equations and relevant microstructural parameters beyond the density.

The necessity of pursuing the second approach, which includes the microstructure, becomes obvious from the limitations of using only the density as predictor for macroscopic behavior. The large scatter of elastic modulus, strength, and viscosity against density [78] limits the scope of validity of density as indicator for mechanical properties. In two independent studies it has been observed that compressive load in snow is transmitted only by a small portion of snow grains in the structure [2, 60]. In these descriptions, some grains form "dead ends", which contribute with their mass to the density, but not to bearing load. In other experiments, an increase of strength in time was observed, while the density of the samples remained constant [24, 119]. The increasing strength was in both cases attributed to the microstructural evolution via sintering. The observation of an increase in unconfined compressive strength by a factor ten in time dismissed density as primary indicator [24]. These observations triggered new ideas - and problems: the contact area between grains helped to explain the observed increased strength [119] - but how to determine it efficiently?

With this, a central question of snow micromechanics can be stated: how does the material behavior depend on the microstructure and processes therein, and how can the microstructure be characterized?

1.2 Snow microstructure

Snow consists of ice crystals that precipitate as snow flakes in a large variety of fascinating shapes [69]. On the ground, the single hexagonal crystals grow together (sinter) and form a complex polycrystalline ice skeleton, which we refer to as the snow microstructure. The microstructure constitutes the porous medium snow and defines any physical properties of snow. Being composed of ice, snow has many similarities with other crystalline materials, such as metals.

A special characteristic of snow is that it is thermodynamically always close to its melting point. This is expressed in the homologous temperature (ratio of actual temperature and temperature of melting point in K), which for snow is even at -50°C very high with 0.82. For this reason, snow is classified as a hot material. The high homologous temperature implies that ice crystals have considerable thermal energy and surface molecules are volatile [8]. The high temperature has large implications on structural, and consequently on physical properties of snow. Rearrangement of the volatile surface molecules is caused by local differences in the energetic state of the surface. This may cause different modes of mass transportation [8, 30, 61, 69]. These processes, commonly referred to as snow metamorphism, lead to various geometries of the snow microstructure which we experience as different snow types.

Snow types differ in the connectivity of the microstructures, grain sizes, grain shapes, and physical properties [21]. Microstructures and grain shapes can be observed, for example, with X-ray tomography images and under a normal light microscope (Fig. 1.1): Fresh snow looks like the crystals in the upper row of Figure 1.1 - settled, rounded grain snow (middle row) several days after snow fall consists of well connected grains - faceted grain snow (bottom row) forms coarser structures.

The images in Figure 1.1 show snow in two fully different states: snow as sintered, solid-like material in the 3D μCT images, and as a granular material of disintegrated grains under the microscope. Snow is a granular material during snowfall (consisting e.g. of star-shaped particles as the upper right photography shows), or after fracture of the sintered microstructure (as shown in the fragmented particles in of rounded and faceted grain snow in the middle and lower image). Both states, sintered and granular, possess different microstructural and mechanical proper-

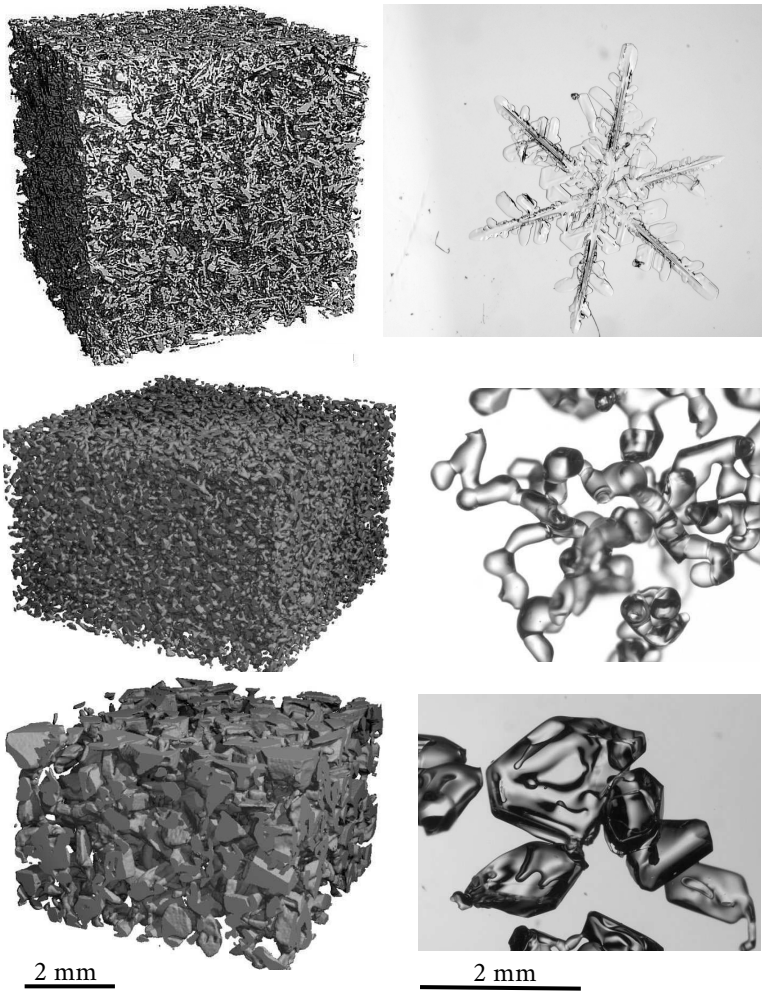

Fig. 1.1: Diversity of snow types originates from different grain shapes; here from top to bottom: Fresh snow, rounded grain snow, faceted grain snow. Snow crystals can be observed in microscope images (right column) only if they are freshly fallen like the star-shaped crystal in the first row or as fragmented particles. The differences in crystal size are typical for these snow types, which is indicated with the scale at the bottom. The left column shows typical microstructures visualized by 3D tomography imaging. (Images: SLF Snow Physics.)

ties. The transitions between these two states are caused either by brittle fracture under mechanical load, or by sintering and metamorphism.

1.2.1 Sintering

If snow crystals are in contact, they grow together by sintering - a process that is typical for hot materials [8, 30]. As during metamorphism, molecules are redistributed within the microstructure to minimize its energy. In fact, sintering must be regarded as an early stage of metamorphism and these two processes go hand in hand. The schematic in Figure 1.2(A) illustrates the mass-redistribution during sintering on two particles in contact that were initially spherical. Molecules from the body of the spheres are moved to the contact region and fill the space between the particles around the contact point. This results in a reduction of the total surface area. If vapor transport is the dominant process, it is driven by different equilibrium vapor pressures at the particle surfaces near and far from the contact point, due to different curvatures (Gibbs-Thomson-effect). However, different mass transportation mechanisms contribute to the sintering process [43, 61], which are comprehensively summarized by Blackford et al. [8]. The predominance of transportation mechanisms varies with the stage and conditions of sintering. For snow, it has been found that sintering proceeds mainly via the vapor phase, so called vapor-diffusion sintering [8, 15, 43]. Two sintered ice particles are shown in the microscope image in Figure 1.2(B). A grain boundary can clearly be seen as a rim where the two particles sintered (taken from [8]).

The sintered contact area increases in time, the effect of sintering is stronger on smaller particle sizes and at higher temperatures [8, 114]. Sintering rates vary for different snow types and grain shapes, with different initial contact areas and local surface curvatures [41]. While the sintered necks grow in time during minutes, hours, and months, the grains in the microstructure become better connected and the microstructure gains strength (e.g. [24, 41, 45]).

While sintering on time-scales of minutes to months is quite well investigated for snow within the wealth of metamorphism studies, very little is known about fast sintering within seconds. In laboratory experiments with two spherical ice particles brought into contact for durations in the sub-second range, a measurable effect of sintering was observed [32, 114].

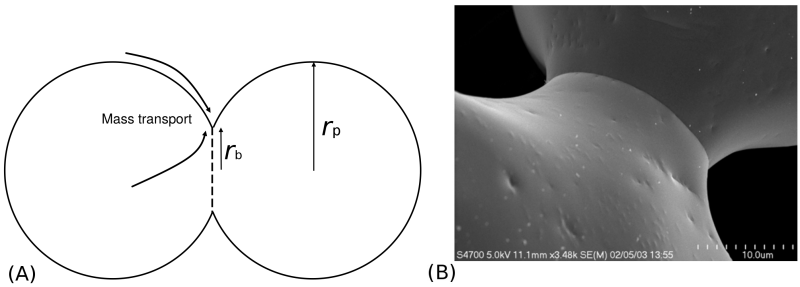

Fig. 1.2: Two sintered ice particles: mass transportation from the bulk to the contact region between two particles increases the circular contact area (indicated with the bond radius r_b) as sketched in (A); the resulting neck clearly shows the grain boundary between the two particles (B - scanning electron microscopy image, taken from [8])

This was explained by instantaneous freezing of a liquid-like layer on the particle surface [19, 44, 93], which forms a solid, crystalline contact between two particles [114]. The observed time-dependence was explained by the formation of an initial contact area due to elastic deformation of the particles, which increases in time via creep when the particles are pushed against each other. The creep deformation strongly depends on temperature and the applied contact forces. Since high contact forces were applied on the particles in the latter experiment, the role of fast sintering in snow mechanics is still barely understood. However, few studies report the observation of cohesion in snow during dynamical, macroscopical processes such as avalanches [58, 112], which is explained by fast sintering at temperatures close to $0°C$. On the grain scale, this effective "cohesion" was observed during short contact times in angle of repose experiments [63].

Mechanically, sintering is relevant on all time scales. It strengthens the structure over time and transforms snow from a granular into a solid-like material. Such a transition may also happen during deformation, e.g. during avalanche release or flow on short time-scales. Consequently, the sintering state of the microstructure needs to be carefully characterized.

1.2.2 Microstructure characterization

Due to the diversity of snow types, investigated snow has to be characterized in any scientific study of snow. Various studies focus on the characterization of snow microstructure to find microstructural metrics and suggest methods to measure them (e.g. [28, 37, 47, 71, 95, 116]). However, there is no set of parameters that specifies snow exactly for all purposes, i.e. under mechanical, optical or thermal view points.

The difficulty of finding relevant microstructural parameters becomes obvious when looking at grain size, a rather simple property - on first sight. Upon further inspection the ambiguity becomes apparent: what is a grain in a sintered microstructure? In the traditional snow classification [21], several grains are "sampled" by hand from the snow pack for investigation in loose, disintegrated form under a magnifying glass. Thus, the determination of grain size is a subjective method, based on a mechanical fragmentation process and the destruction of the sintered state. In the international classification, grain size is defined as the largest extension of the grain [21]. This definition presumes that the largest extension is visible under the microscope or magnifying glass, which only captures a 2D projection of the 3D particle. The grain extension as metric for grain size is somehow characteristic for the snow type [21] and can be helpful when considering snow mechanics, at most at a qualitative level, e.g. to guess how well grains are connected [104]. For optical snow properties it is known that the grain extension is simply the wrong metric. In this case, the surface area and the volume of grains are relevant [123]. This leads to another metric for grain size, namely the optical equivalent grain size, which is defined by the inverse of the specific surface area, the ratio of sample surface to sample volume. This example illustrates that not even for an apparently simple property - grain size - there is an unambiguous metric. The way of characterizing snow depends on the specific purpose.

Despite the ambiguity of defining grains and contacts in a sintered microstructure, the concept of grains (grain size, grain shape, inter-granular contact) is important for many applications. The ambiguity becomes clearer when looking at the microscopy image of rounded grains in Figure 1.1: it shows fragmented pieces of snow, which still consist of several sintered crystals; the sintered contacts are large, thus, the crystals form a rather continuous structure, where irregular shaped grains and con-

tacts between grains can hardly be discerned. Nonetheless, the shape of the crystals is so central that it is used to classify snow types by visual judgment of disintegrated snow particles [21]. In this way, physical properties are assigned to snow types, instead of directly deducing physical properties from parametrized features of grains or microstructures. Such an indirect way is taken, because of the difficulty to characterize irregular grain shapes by adequate shape parameters to predict the physical properties. This is a general problem for describing granular materials [3, 96, 107]. In snow, characterizing grain shapes is even more complex, since it is not clear what a grain and a contact actually is in a sintered microstructure. Today, sintered microstructures can be characterized in 3D images from computed tomography, without breaking snow particles.

3D micro-computed tomography imaging

Since about 20 years [11], micro-computed-tomography (μCT) imaging is an invaluable tool to observe snow in three dimensions without destructing the structure. This allows us to investigate how the particles are connected and form a structure, or how the structure evolves in time (e.g. [92, 127]) to understand mass fluxes and metamorphism in snow. Digital 3D images have opened entirely new doors: a) to determine a variety of microstructural characteristics in a reproducible, objective way, b) for transferring a certain microstructure into numerical models, to directly calculate physical parameters or behaviors on the structure itself. With both possibilities, 3D μCT images introduced a new dimension into snow science.

The μCT images allow for a digital reconstruction of the two-phase microstructure of snow: the ice skeleton and air. From the digitized microstructure, classical parameters like density and specific surface area can be derived now in a rather standardized way [37, 42, 95]. Many other methods, adapted from other fields of research or developed for specific purposes, can be applied to the images.

Considering grain size as example again, it can be derived with diverse methods: via the specific surface area (optical equivalent grain size), by investigating the distance of each point in the ice matrix to the next air voxel (using predefined distance transform functions), or via correlation lengths obtained by calculating 3D correlation functions on the images [95]. These size metrics are well-defined length scales of the continuous

microstructure. They can be used to unambiguously define a "grain size" even though it is hardly possible to select a "grain sized" unit in the 3D structure by eye. This is mainly due to the fact that the continuous microstructure in 3D μCT images does not resolve crystallographic grain boundaries which makes grain identification by eye ambiguous.

The identification of grains in the continuous structure is necessary for determining grain shapes or inter-granular contacts and contact sizes - parameters which are of great interest for various applications. One possibility of objectively identifying grains in the continuous structure is the so-called watershed segmentation, which detects constrictions in the structure that are often formed at the sintered contact between two grains [106, 116]. Another method is the evaluation of the minimum cut-density [33]. These procedures are applied to obtain a particulate microstructure as basis for further investigations.

Methods for using μCT images to gain new information about snow microstructures are continuously evolving. The μCT images make problem specific investigations of snow microstructure possible and enable the definition and introduction of new parameters. Many existing methods and tools (e.g. Paraview, Python libraries) provide great computational support. Correlation lengths, for example, can be used to determine structural anisotropy [71], which helped in explaining thermal [71], or mechanical [29] properties of snow. Another example is the quantification of surface curvatures [59], which was combined with highly resolved temperature gradients [52, 92] to investigate vapor fluxes and crystal growth during metamorphism. Using these quantities (curvature, temperature gradients) from time-lapse μCT scans allowed for comparison with analytical laws for crystal growth to verify our understanding of microstructural evolution [59].

Many of the mentioned methods (e.g. determination of temperature gradients, anisotropy, and specific surface area) are meanwhile well established in snow science and allow for a comprehensive characterization. Thus nowadays, 3D images constitute the perfect starting point to develop a micromechanical understanding of snow by comparing microstructure based numerical models to real experiments. Besides comprehensive and objective snow characterization, μCT images changed snow mechanics by also enabling virtual experiments.

1.3 Snow micromechanics

Micromechanics aims at predicting the macromechanical behavior of a heterogeneous material, such as composites, polycrystals or snow by explicitly taking into account the heterogeneities (microstructure). These materials consist of clearly distinguishable constituents and a micromechanical approach takes their given geometries and properties to predict the global behavior. One important task is to understand the spatial distribution of stress and strain in the microstructure under a given global load, to know where damage and failure occurs. Then, the concept of the representative elementary volume has to be considered, which is regarded as the subvolume of sufficient size to statistically resolve geometrical and stress homogeneities for a reliable prediction of the material behavior.

In snow, micromechanical approaches must combine the geometry of the snow microstructure and mechanical properties of ice. For the polycrystalline microstructure, one usually considers properties of polycrystalline ice already at the level of an individual geometrical snow grain (e.g. [29, 49]), without accounting for the crystallographic microstructure of snow.

Research focuses on finding appropriate microstructural parameters for micromechanical descriptions. The sintered contacts between snow grains are an important part of the microstructure with great relevance for the mechanics [24]. The contacts are the weak parts in the structure where fracture occurs most likely [38]. Thus, the number and the size of the bonds are important microstructural parameters and formulations were made to relate the local strength of the microstructure, which incorporates these parameters, to the global strength of snow [6, 24, 28]. Such relations are used to parametrize snow in numerical models, e.g. in the discrete element method where snow microstructures are often simplified with spherical particles. Number and sizes of their contacts are parameters, which are used to discern the behavior of different snow types in simulations [49, 118]. However, this is a rather empirical approach that relies on guessing these parameters due to the aforementioned difficulties in identifying particles and contacts in the microstructure.

Empirical concepts of particles and contacts are also used for the interpretation of the SnowMicroPen [47], which is a convenient tool for acquiring data of a natural snow pack in the field. It consists of a long

rod which measures the force on its tip as it is driven into the snowpack with high spacial and temporal resolution. The recorded mechanical signal is used to characterize the snow, via microstructural parameters. By interpreting the force peaks as fracture of sintered grains, the signal is related to a length-scale of snow grains from which important snow characteristics are deduced [95], for example, specific surface area and density. In this way, a snowpack can easily be characterized (compared to the efforts of a time-consuming snow profile), but it relies on profound knowledge about microstructural and mechanical parameters, which still demands improvements [72, 88].

Although the SnowMicroPen was designed to characterize sintered snow (e.g. density, specific surface area, and strength), the method is based on fracture of the microstructure, which is followed by grain rearrangement at the tip where the force is measured [41]. Thus, for evaluating the force signal, one should not only consider the (local) strength of sintered snow, but also granular dynamics. However, little is known about snow mechanics in the granular state on the grain scale, e.g. the role of grain shapes and mechanisms such as fast sintering on time scales of (sub-)seconds. One early experiment in which the influence of grain shape, grain size, cohesion, and friction on the granular dynamics were investigated [63] has to be mentioned here. The study indicates that sintering takes place within very short contact times. Meanwhile, other studies [32, 114] confirmed this observation. Fast sintering causes single grains to cluster together and form agglomerates which change the flow properties [58, 63, 112]. Current research is becoming increasingly aware of this fact and the necessity to include sintering for describing granular snow, e.g. in the interpretation of the SnowMicroPen signal [89], in numerical simulations [83], and in minimal models for compression experiments [73].

1.4 Snow micromechanical modeling

Snow micromechanics nowadays benefits from virtual experiments on digital snow using numerical models. By capturing microstructures via μCT imaging, the digitized microstructures can be fed into numerical models, such as Finite Element Models (FEM), to calculate physical properties directly on the structure. Approaching snow mechanics in this

way led to invaluable new insight. For example, by FEM simulations of elastic stress, stress localizations within the sample can be detected and mechanical properties of extremely fragile snow layers can be derived, which are experimentally hardly manageable but crucially important for avalanche prediction [102]. Simulations of tensile tests revealed intergranular sintered contacts as weak parts in the structure where main damage occurred [38]. FEM simulations of creep resolved that main deformation occurs within the crystals not only at the grain boundaries [115]. Moreover, it has been shown with microstructure-based FEM simulations that the elastic modulus of snow can be determined more reliably in simulations than in experiments [29, 57, 111, 124].

The advantages of combining microstructural 3D imaging and numerical modeling are convincing. Detailed information about a material's state that includes all aspects of a microstructure (not only few parameters), help to understand basic mechanisms in the microstructure, and provide us microscopic relations that are experimentally not accessible. However, validated models need to be at hand, which do not exist for all purposes yet.

Today various approaches are used to capture snow behavior in numerical models and are chosen for the specific purposes. A generalized model that is able to describe the behaviors of diverse snow types under various conditions does not yet exist. Finite element models, for example, are commonly used to investigate highly resolved microstructural processes for small displacements. However, fast deformations that include fracture and grain rearrangement, important for most snow mechanical problems, cannot be captured by FEM models with reasonable efforts. The Discrete Element Method (DEM) is capable of describing a wide range of deformations - e.g. creep, fracture, granular flow - but, so far, it comes along with limitations in microstructure representation. Initially, it was applied to describe snow creep deformation [46] and later also to investigate optical properties of snow [53]. DEM has become popular for simulating fast and large deformation of snow on various scales.

On the slope scale, DEM is used to simulate avalanche flow, e.g. to investigate pressure on obstacles [64]. Here, the discrete elements represent snow agglomerates. On a smaller scale, DEM is used to examine fracture mechanisms as preconditions of avalanches. New knowledge about the interaction of a slab on top of a weak-layer (necessary layering for most common slab-avalanches) could be gained by investigating frac-

ture mechanisms in the weak-layer and mechanical properties of the slab [9, 26, 83]. It could be shown that for compression-dominated loading and low loading rates strength significantly increased through sintering (rebonding), whereas for shear-dominated loading little influence on the loading rate was found [83]. On this scale, the discrete elements are randomly arranged and parametrized to match snow properties such as density and elasticity. With more detail on a micro-scale and grain-level, fracture is simulated where DEM particles represent snow grains. Then, the particles bear mechanical properties of ice [36, 49, 77, 118]. At this grain level, the arrangement of the DEM particles for microstructure representation becomes a subject of research itself.

For microstructure representation on the grain-scale, grain arrangement, grain shapes, and contacts have to be defined in DEM. The grain shape has to be accounted for since it affects inter-particle contacts and interactions [36] and differs significantly from the spherical shape of DEM particles. At this point, the snow micromechanical descriptions can be split into two approaches. In one approach, detailed microstructure representation is used to investigate micromechanical processes [36, 77]. Via μCT images real grains are mimicked with high detail and recreated with several discrete elements [33, 75]. The compromise is a high computational cost and the consequence the restriction to small sample volumes of few mm^3. By simulating the behavior of different snow types (with similar densities) the relevance of microstructure was underlined [76] and force-chains that are formed by several grains in the microstructure could be detected [77]. By a detailed analysis of the latter, it was shown that buckling of the force chains can cause volumetric collapse, whereas stable force chains lead only to a localized failure in which the contacts of the force chains to the surrounding material play a crucial role [77]. In the other approach, DEM is seen as a generic tool to understand dominant processes in snow as a crushable material, e.g. to study the interaction with car tires [79, 118]. Then a grain is represented by a sphere and parametrized with the radius (representing typical grain sizes), a rolling friction parameter that accounts for non-spherical particle shapes, and the density of the sphere packings matches typical snow densities [49, 118].

The two approaches differ in purpose but share the same limitation: none of the models can be validated with real experiments. The development of the models based on generalized sphere packings always

requires the fit of free parameters, which are related to particle and contact properties of the spheres. In other words, a sphere based DEM model can only be validated when sphere based microstructures are used in experiments.

1.5 Research gap

Discerning microstructural and mechanical influence on macroscopic observable behavior is crucial for describing basic mechanisms for diverse snow types and external conditions. The concept of grains, shapes, and contacts determines how we interpret snow behavior, e.g. the mechanical signal of the SnowMicroPen, or how we parametrize models, especially DEM, but it conflicts the real microstructure of snow. This discrepancy complicates the description and simulation of snow mechanics, as outlined in the context of DEM modeling in the following.

For simulating snow behavior under brittle deformation, including fracture and grain rearrangement, different microstructural parameters are required to describe sintered and granular snow. Granular snow is dominated by particle interactions for which grain shapes are relevant, whereas the mechanics of the sintered microstructure are dominated by spatial distributions of particles and bonds, and bond sizes. These parameters need to be determined.

The characterization of irregular particle shapes lacks standardized methods and parameters [3, 65, 107], is often restricted to 2D projections of 3D particles (e.g. photographs, microscopy images) and a small number of particles [66]. This motivated a recent study, in which a huge number of classified snow grains was digitized to obtain a data set and distribution functions of various shape metrics which are relevant for modeling radiation in snow [66]. However, the investigated metrics (e.g. eccentricity, major and minor axis of momentum-equivalent ellipsoids) cannot yet be connected to other physical properties, e.g. granular flowability. Extra experimental investigations are required to establish a relation between such shape metrics and physical properties. A very common means for investigating such relations is the analysis of the angle of repose, a characteristic of a granular material that depends on particle (e.g. shape, size) and material properties (e.g. friction, cohesion) [3]. For other materials it has been used, for example, to establish

a relation between particle shapes and electrical conductivity [107] or for model parameter calibration, e.g. [3, 23]. However, for granular snow little experimental information on the grain scale exists. Lacking data for mechanically relevant shape parameters, grain shapes in DEM are either recreated from μCT data [36, 77] (with the disadvantages outlined before) or taken into account by a rolling friction parameter for spherical particles, whose limited usefulness is known from research on other materials, e.g. [125]. For snow, this parameter has to be guessed [49, 83, 118].

To describe sintered snow as a microstructure of grains and contacts similar as it is seen in DEM, individual grains need to be identified. The approaches described above (based on watershed [106, 116] and minimum cut-density segmentation [33]) involve a lot of interpretation of what a grain and what a contact is. The absence of reliable microstructural data from experiments for model calibration follows from the lacking definition (what is a grain?) and forces model developers to empirical approaches [49, 64, 83, 118]. Bond sizes are therefore commonly fitted to match macroscopic strength measurements [49, 118]. However, a sophisticated parametrization of bond sizes would be useful to efficiently simulate the behavior of different snow types [118].

In addition to the difficulty of including long-term sintering (for times $>$ minutes) in DEM via bond sizes, the need to account for fast sintering [114] (for times $<$ few seconds) is becoming increasingly evident. So far, it was unclear whether fast sintering (measured with high contact forces for spherical ice particles [114]) is relevant for snow mechanics during high strain rate deformation, where contact times are short but also contact forces are low. Recent studies highlighted the necessity to account for fast sintering [13, 73, 83, 89] as significant influence in the respective (numerical) tests was observed. It has been stressed [13] that an equivalent experimental observation of the effect of fast sintering would not have been feasible, as the micromechanical processes are not sufficiently resolved. Effects of irregular grain shapes (sharp edges), friction, and fast sintering need to be quantified to overcome microstructural ambiguity and facilitate validation of these models.

Constraining microstructural uncertainties is essential for profound knowledge about snow micromechanics and mechanical modeling. Facilitating microstructure-based model validation is a crucial step for using

numerical models to reliably predict snow behavior and to further investigate micromechanical processes.

1.6 Approach and outline of this thesis

This thesis aims at advancing the micromechanical understanding of snow by eliminating microstructural uncertainties. To address the limitations raised in the previous section, the present thesis designs and analyzes a new model snow type, spherical ice beads. The goal of the thesis is to provide an experimental realization of the microstructures (sphere assemblies) which are used in DEM to facilitate an unambiguous model validation. The particle properties (size, shape, contacts) have been characterized in μCT images. Mechanical experiments were performed along with natural snow types for comparison. The effect of sintering was investigated in the bonded contacts after different sintering times (days), and in the granular state (seconds) under variation of temperature. By varying the temperature in the granular experiments, sintering and shape effects could be discerned. The macroscopic mechanical behavior of the sintered state was characterized by unconfined compression experiments, which were compared to the predictions of different DEM models.

The mechanical and structural examination was approached in three steps (1-3), after which their potential for DEM model validation was evaluated in a final step 4.

1) The ice bead production method is introduced. The ice beads are characterized to verify their particle properties required by DEM, including the analysis of particle sphericity and size-distribution, number of contacts, and crystallographic structure. Mechanical properties of the microstructure in the sintered state are investigated in unconfined compression tests with variation of sintering time. A comparison to natural snow types is included. (Chapter 3)

2) Properties of the granular state are investigated in angle of repose experiments with ice beads and the natural snow types. Two factors are discerned that influence granular dynamics of snow on a

microstructural level: non-spherical grain shapes and the effect of sintering during short contact times. (Chapter 4)

3) Sintering and bond formation of the ice beads is investigated via high-resolution μCT images, including time lapse imaging of the sintering process. The occurrence of sintering anomalies (porous bonds) that were before revealed in the unconfined compression tests (where the μCT resolution was too low for a detailed analysis), are here discussed in relation to Mullins-Sekerka theory that predicts unstable crystal growth (sintering) depending on the particle size. Particle sizes and thermal conditions for which this phenomenon occurs are examined to gain confidence for the interpretation of the compression experiments and for future ice bead sintering experiments. (Chapter 5)

4) The unconfined compression tests of six ice bead samples are simulated in micromechanical DEM models. The microstructures are defined by particle position and size, which could efficiently be extracted from the μCT images. Using these microstructures and realistic material properties of ice, the main experimental observations are reproduced. (Chapter 6)

In this order, these four steps are detailed in the remainder of the thesis, after an overview of the used materials and methods in the next chapter, and followed by an overall conclusion and outlook.

1.7 The SnowDEM project

The presented research was performed within the SNF project *SnowDEM*. This is a joint project that combines the snow scientific expertise of the SLF with the numerical competence of the xDEM group at the University of Luxembourg to develop a micromechanical snow model with the Discrete Element Method (DEM). The project comprises two doctoral dissertations. This thesis presents snow mechanical experiments and microstructural analyses to investigate main micromechanical processes and facilitate detailed model validation.

Materials and methods

2

A variety of experimental, characterization, and numerical methods were combined for the research of this thesis. Each of the following chapters contains a specific methods section, where the applied tools and techniques are detailed within their specific context. Since several of them were repeatedly used, this chapter provides an methodological overview with additional background information. Additionally, the choice and production of snow types used for all experiments is explained.

2.1 Snow samples

Throughout the research of this thesis, ice beads and three natural snow types were used. For the sake of reproducibility, all of them were produced in the lab.

2.1.1 Ice beads

With the ice beads, we aimed at creating well-defined model snow. Spherical particles possess the simplest shape, which can be easily characterized in experiments and facilitates straightforward comparison with DEM microstructures. Therefore, the main prerequisites of the ice beads were a spherical particle shape and a mono-disperse size distribution. We developed a new method for producing such particles, since we did not find the two requirements fulfilled in the spherical ice particles presented in the literature. In a few experimental studies of ice spheres, the particles were created by spraying water into liquid nitrogen [16, 43, 62]. The resulting particles had a wide particle size distribution and did not fulfill our demands of sphericity (concluded from visual inspection of the

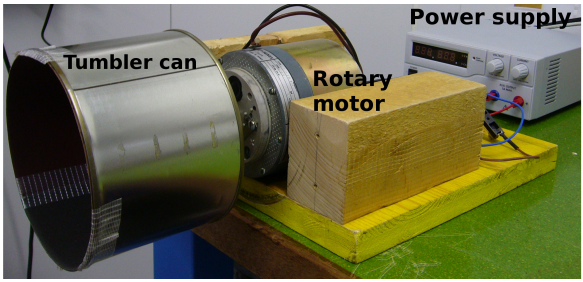

Fig. 2.1: Photograph of the tumbling machine: An aluminum can is mounted on a rotary motor. During tumbling the can is closed with a cap.

depicted particles; sphericity was not characterized in either of the cited studies). Therefore a mechanical abrasion method [31] was investigated. The constructed tumbling machine is shown in the photograph in Figure 2.1. A sketch of the machine and the technical details are provided in Chapter 3.2.1.

The main challenge in establishing this method was to find appropriate initial particles. Several tests were performed until we found a satisfying solution. In a first attempt, snow with rounded grains and melt forms was collected from a natural snowpack in late spring. However, the particles did not round off sufficiently, but instead formed unsatisfying "potato snow" depicted in Figure 2.2. Using frozen water droplets improved the result. The ideal method was found to be producing water droplets with a syringe on a Teflon sheet. Using the syringe, the particles were approximately equally sized. The hydrophobic Teflon sheet maximized the contact angle, which made the droplets as round as possible. After tumbling, these particles rolled nicely on a flat surface, which indicated their spherical shape (the detailed characterization of sphericity is presented in Chapter 3.3.1). This was established as satisfactory method.

If a surface is used which is less hydrophobic than Teflon is used, droplets with a smaller contact angle are created. Such particles become ellipsoidal during tumbling. This particle shape did not serve our purpose. However, it would indeed be interesting to conduct experiments with non-spherical particles with clearly defined shapes.

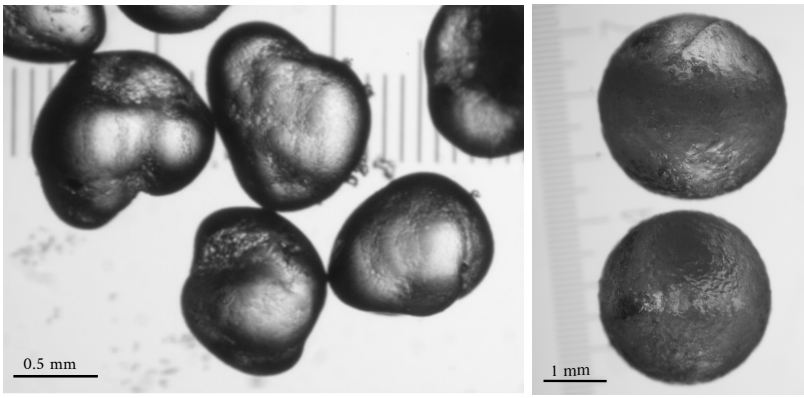

Fig. 2.2: Microscopy images of tumbled particles: left image shows "potato snow" that results from tumbling natural snow; Right image shows ice beads as they were finally produced by tumbling water droplets. Note the different magnifications of the images.

2.1.2 Nature identical snow types

The natural snow types were used in the experiments to investigate the behavior of real snow in contrast to the ice beads. Therefore, we chose two of the most common snow types, rounded and faceted grains [21]. In order to have the same snow available throughout the duration of the research for this thesis, the snow was produced in the lab instead of collecting it from the field. The snowmaker [101] available in the lab provides us with fresh snow year round. In the snowmaker, dendritic crystals grow on nylon threads as moist air is blown over the threads. The main difference to crystal growth in clouds is that the crystals grow unidirectionally towards the air stream, whereas crystals in clouds grow in isotropic conditions. Nevertheless, this snow resembles natural snow not only visually, but also in common characterization parameters (e.g. crystal size, density, specific surface area). This is why it is referred to as nature identical snow [101]. It served as the base material for creating different snow types by storing them in different thermal conditions and promote different types of metamorphism. The metamorphism conditions required to grow rounded and faceted snow are described in Chapter 3.2.2 and 4.2.1.

The two snow types differ in typical grain size [21]; rounded grains are commonly smaller than faceted grains. Since both particle shape and size have an influence on the mechanical behavior, we investigated the faceted grains in two size ranges. The smaller range was chosen to match that of the rounded grains. Eventually, three types were used: rounded grains (RG) and faceted grains (FC) differed in size and shape, whereas the smaller faceted grains (FCS) had similar shape to FC and similar size to RG.

Size selection

Sizes were selected by sieving. To obtain a narrow size range, snow was usually sieved with two consecutive sieves, a sieve with a larger mesh above a sieve with a smaller mesh. The ice beads could be sieved directly after production. In contrast, the nature identical snow types, which formed a sintered microstructure during metamorphism, had to be fragmented before sieving.

2.2 Experiments

All experiments were performed in the SLF cold labs. Six climate chambers are available, which can be cooled down to -40°C . A variety of devices are available for mechanical testing and snow characterization. This provided the infrastructure for the two sets of mechanical experiments and the performed microstructure characterization.

2.2.1 Compression experiments

For the compression experiments, the so-called fast friction tester was used. This machine was developed to perform diverse mechanical tests on snow samples, including direct shear and compression tests. The machine allows for force and displacement controlled deformation along a horizontal and the vertical axis. It is being used for diverse experiments and was described in detail, for example in [117]. We used it to perform deformation-controlled, uniaxial, unconfined compression tests of sintered snow samples. The settings used are described in Chapter 3.2.4.

In order to scan the experimental samples in the μCT before compression, a special sample holder was designed that can be used in both devices. A sketch of the cylindrical sample holder is presented in Chapter 3.2.1, Figure 3.1. The main challenge was the requirement that the cylindrical wall must be stable for μCT scanning (i.e. no tilting during rotation), but easy to be slid down before the compression test. This was finally achieved by fixing the wall with a small screw to the base of the sample holder.

2.2.2 Angle of repose experiments

With the angle of repose experiments, we chose a common type of experiment to characterize granular materials. The angle of repose is analyzed for various purposes, but a standardized measurement method does not exist. Thus, the method has to be chosen and adapted to the specific purpose [3, 96].

We examined the influence of grain shape and cohesion on the granular flow of snow. This is observable in a free, static angle of repose (in contrast to the "dynamic angle" in a rotating drum, or the internal angle that forms within a container). Technically, this is a simple experiment and the necessary tools are available in the lab. The details of the setup are described in Chapter 4.2.2.

2.3 Snow characterization

Characterization of snow microstructures is an essential part of snow science. Generally, we are interested in the geometry of crystals and the properties of the three-dimensional ice matrix they form in their sintered state. For the latter, micro-computed tomography imaging is the most important and versatile tool and has extensively been used in this thesis. For characterizing the crystals, we used two types of microscopes to investigate the geometry and the crystalline microstructure (texture).

2.3.1 Optical microscopy

Photographs taken with an optical microscope were mainly used for a visual quality control before conducting the experiments: while storing the

ice beads between experiments, ice dust settled on the particle surfaces, which was removed by short tumbling prior to an experiment. Particle surfaces could be seen well under the microscope. Images are shown in Figure 2.2 and Chapter 3.2.2 and 4.2.1.

2.3.2 Polarized light microscopy

As part of the ice bead characterization, we qualitatively analyzed their crystalline structure. This is a destructive method. Thus, only 31 particles were investigated. The analysis is based on polarized light microscopy (described e.g. in [97]). The necessary devices are available in the cold lab. Details of this analysis are presented in Chapter 3.2.8.

2.3.3 Micro-computed tomography

Micro-computed tomography (μCT) imaging has been used in snow science since 1999 [11]. It has become a powerful technique that allows for a wide spectrum of structural analyses and even for simulating digitized microstructures in numerical models (e.g. [29, 52, 102]).

At the SLF, two X-ray micro-computed tomography scanners are available, which are operated in a cold room (Fig. 2.3). Snow samples are scanned in cylindrical sample holders that range in size from 10 to 80 mm in diameter. During scanning, a sample holder is exposed to the beam path of an X-ray source and rotated around its central axis for effectively 180°. The detector behind the sample captures the projections of the sample, from which the 3D image can be reconstructed. Scanning time depends on the chosen resolution and sample size. The minimal voxel size of 6 μm can be reached in the smallest sample holders with 10 mm. Scanning a 10 mm high sample takes approximately 2.5 hours.

The reconstructed grey image constitutes a 3D representation of the X-ray attenuation coefficients of ice and air phases. To obtain a binary image, the phases are separated by segmenting the grey-scale images. This is a critical step. The small-scale features of the microstructure, especially the strongly curved contacts between grains, are error-prone. To segment the images in a unsupervised, reproducible way, an appropriate segmentation threshold was determined by fitting the sum of three

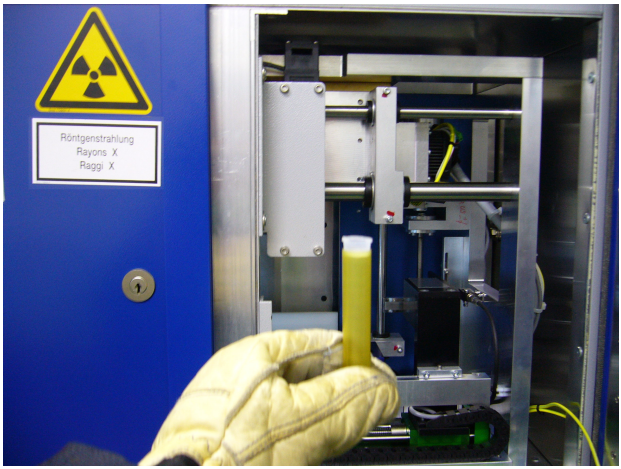

Fig. 2.3: X-ray tomography scanner with a sample holder.

Gaussian distributions to the grey value histogram [35]. This method was used for all images in this work.

The binary images were used for further investigation of the 3D snow microstructure, i.e. the geometrical properties of the ice phase. Standard parameters (e.g. density, specific surface area) were evaluated with the image processing software provided by the μCT producer Scanco Medical. Additional processing routines were developed for the specific purposes of this thesis and are outlined in the following section.

3D Image analysis

Identifying the particles in the two-phase microstructure was necessary for all research tasks. The steps described in the following were the basis for the automated particle characterization (particle shape and size, contacts and contact porosity, Chapters 3, 4, and 5), as well as for the reconstruction of the ice bead microstructures as model inputs in Chapter 6. The following steps were performed using the programming language Python. The binary images were represented as numpy arrays for efficient calculations. Moreover, existing libraries (e.g. `Skimage`) supported image analysis, also in 3D, with useful functions and algorithms.

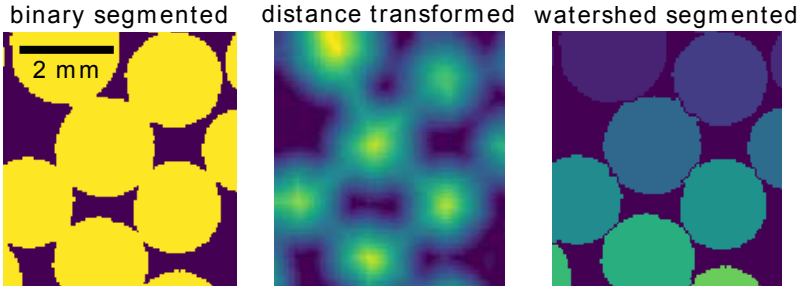

Fig. 2.4: Main steps of the image processing routine visualized in 2D slice: particles in the binary image are segmented with a watershed algorithm that starts at the local maxima of the distance transformed structure (particle center). Colors: The binary image shows ice in yellow, air in violet; the distance transformed image indicates the distances of ice voxels to the next air voxel, where lighter colors represent higher values; the watershed segmented image shows the identified regions in different colors.

Identification of particles in a continuous structure can be done with a so-called watershed algorithm. This algorithm detects constrictions in a structure, which are commonly located where particles are in contact. For spherical particles, this works very well [110]. In snow, the identification of grains is ambiguous, but has also been tackled with watershed segmentation before [106, 116].

As preparation for the watershed algorithm, a distance transform is performed on the ice phase of the 3D images. This identifies, for each voxel in ice, the shortest distance to the next voxel of the air phase. In the resulting image (Fig. 2.4), local maxima are searched, i.e. the voxels that have largest distances to the ice phase, which are at the center of the ice structure (in the particle center). From these local maxima, the watershed algorithm starts to "flood" the ice phase along the gradient of the distance transform, until reaching the air phase, or the flooded region of the neighboring local maximum. The latter is reached at constrictions and indicates the boundary between two adjacent particles. The utilized algorithm has the option to represent the identified "watershed" with a one-voxel thick area between two neighboring particles. These watersheds were analyzed to obtain an estimate of the contact area (Chapter

5). The identified regions are then labeled such that all voxels of a region obtain the same integer value. These labels identify the particles. The routine is visualized in Figure 2.4.

The identified particles can then easily be extracted from the volume for individual analysis. This can be achieved by filtering the image for the value of the label of the desired particle: all voxels with other values are set to zero. With predefined functions (e.g. from the `regionprops` toolbox) the particle can be analyzed, for example, by calculating its perimeter, center of mass, or volume. The determination of the so-called "bounding box" that defines the smallest cubic subvolume that contains the entire particle was helpful. This made calculations on the particle more efficient and was used to detect neighboring particles by identifying the labels of other particles contained within this subvolume.

The watershed segmentation of the 3D microstructures was used for all analyses. Other techniques, as outlined above, were then used and combined for further quantification depending on the particular goals. They are detailed in the following chapters. For example, particle shapes were characterized in Chapter 3.2.6 and 4.2.3, bond porosity was analyzed in Chapter 5.2.2, and particle positions and sizes were calculated as DEM model inputs as presented in Chapter 6.2.2.

2.4 Numerical methods

Numerical simulations were conducted with FEM and DEM models. FEM simulations were employed to obtain additional physical properties of the investigated samples. Snow micromechanical DEM models were used to simulate the unconfined compression experiments with the ice bead.

2.4.1 Finite element simulations

FEM models are used for numerical solutions of partial differential equations on objects with complex geometries. Therefore, the objects are decomposed into a mesh (finite elements) of simpler and well-defined geometries for which necessary equations can be solved more easily. From these solutions and the interactions of the finite elements, macroscopical properties of the objects can be derived [25].

The digitized snow microstructure acquired from 3D μCT scanning can be used as the model input, where the voxels represent the finite elements of a hexahedral mesh. We used two types of models, both of which have been previously validated for snow. The elastic modulus [29] is presented in Chapter 3.2.7. The experiments presented in Chapter 5.2.3 were complemented with FEM simulations of the temperature field within the samples[52, 92].

2.4.2 Discrete element simulations

The discrete element method was originally developed in the context of molecular dynamics for simulating movements and interactions of large numbers of particles [17]. In contrast to the FE method, DEM models simulate the behavior of loosely interacting particles (discrete elements). In the simplest case, these particles are spherical, but more complex particle shapes can be simulated as well (e.g. [36, 65]). The application field of this method broadened, especially for simulating granular matter. With the possibility to bond particles by beams, as described in [94], the method became even more versatile.

For simulating snow, the main advantage of DEM models over FEM models is the capability to simulate loosely interacting and bonded particles; this is a precondition for simulating brittle deformation and fracture of snow.

For snow, DEM was used for the first time in 2005 [46]. Due to its capability to simulate granular as well as bonded particles, it has become increasingly popular. Various models have been developed. We used the open source code Liggghts [56] and the xDEM code developed in the LuxDEM group [50]. Both are described in Chapter 6.2.1.

Ice spheres as model snow: tumbling, sintering and mechanical tests

3

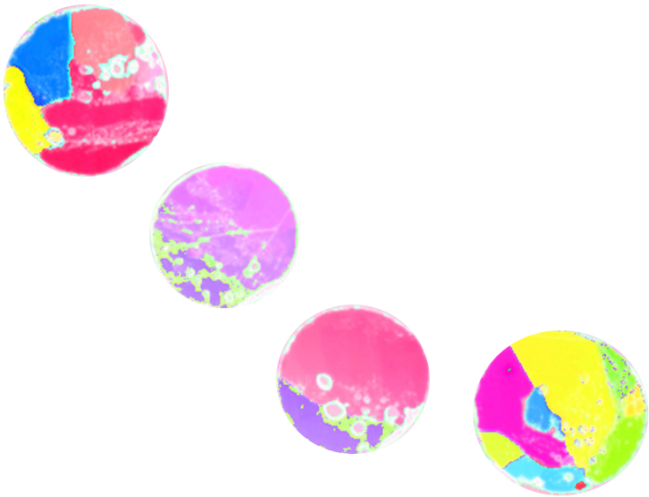

Published in Frontiers in Earth Science:
Willibald, C., S. Scheuber, H. Löwe, J. Dual, and M. Schneebeli (2019), *Ice spheres as model snow: tumbling, sintering, and mechanical tests*, Frontiers in Earth Science 7, 229, doi:10.3389/feart.2019.00229.

Abstract

The snow microstructure is crucial for the mechanical behavior of snow, but is usually simplified in numerical models. In Discrete Element Models (DEM), often used in snow mechanics, the microstructure is typically represented by sphere assemblies. This renders a model validation difficult, as the real snow crystal shapes affect the actual contacts and consequently the macromechanical behavior. To approach this problem from the experimental side, we created simplified microstructures comprising spherical ice particles and examined this model snow under structural and mechanical aspects. We developed a new method to create uniform ice spheres and performed a detailed particle characterization using 3D computed tomography (CT). We examined sintered sphere assemblies to relate microstructural and macromechanical properties in a geometrically well-defined system. Microstructural variation was created by varying the sample density and sintering time, to study the role of the number and size of contacts. 3D CT scans were taken of sintered sphere samples, which were then tested in unconfined compression experiments together with a nature identical snow type as a reference. The scans were evaluated regarding the number of particles and contacts, and were used to compute the elastic modulus, as additional mechanical property. The results of the particle characterization showed the spherical shape and sharp size-distribution of the particles, which are the main prerequisites for model validation. The CT image analysis showed the reproducibility of the sphere assemblies and can be applied for efficient reconstruction of the experimental samples as initial condition for simulations. The mechanical properties conform with the reference snow and the expectations from literature, however, the CT scans revealed a complex geometry of the sintered contacts with measurable impact on the mechanical properties.

3.1 Introduction

Snow mechanics is still an active field of research, despite its considerable history over the past 90 years [78, 105]. Avalanche risk forecasting, snow mobility, snow sports or snow and firn compaction, in general, are just a few of the applications that require quantitative characterization of the dominant mechanical processes. The main challenge thereby comes from the versatile and changeable nature of snow microstructure. Snow is a porous material that consists of an ice skeleton and air. The skeleton forms from single ice crystals that grow at mutual contacts via (early stage) sintering and later evolve in time via (late stage) sintering which are commonly subsumed in the term snow metamorphism. The geometry of the microstructure manifests itself in diverse snow types and physical properties. A reliable mechanical model would only need to combine a geometrical description (snow microstructure) with mechanical properties of ice to fully predict the mechanical behavior of snow [14, 38, 102].

The geometrical characterization of snow microstructure has considerably advanced in recent years, mainly due to micro-computed tomography (CT). CT imaging allows us to constrain the microstructure in simulations for comparison with experiments. Combining microstructural and mechanical properties of snow has considerably enhanced the comprehension of snow mechanics [38, 57, 111, 121]. For example, it has been shown that the sintered contacts between the grains are the mechanically weakest parts where the structure fractures [38]; or that the elastic moduli can be fully predicted from the microstructure measured by CT and the elastic properties of ice [29]. However, the incorporation of the microstructure comes along with high methodological and computational effort. A detailed reconstruction [36] is restricted to small volumes, whereas in a simplified representation [116] the precision is limited by the complexity of the snow crystal shape that renders an unambiguous identification of grains and contacts impossible. Quite generally, if a model utilizes a microstructure model comprising grains, the mapping onto the real bicontinuous geometry obtained from CT images remains the main difficulty.

The difficulty of incorporating the microstructure is an inherent problem of discrete element modeling (DEM) of snow. DEM has become

a powerful tool to model snow mechanics [26, 36, 46, 50, 80] and has also been employed in snow optics [53]. DEM is widely used to simulate granular materials by calculating particle dynamics and interactions. For snow, DEM is appropriate because the granular particles can also be bonded and thereby represent the sintered, solid-like structure of snow, and yet fracture can be described, as under fast deformation. Then the two key ingredients that need to be specified in DEM modeling are particles and contacts between them. In the simplest and computationally most efficient case, the particles are spherical. The remaining difficulty is then to map the experimental microstructures onto a sphere assembly that captures properties of real snow. The existing approaches include e.g. generic (ballistic) deposition models [83] or configurations drawn from Baxter's sticky hard spheres [28]. While these approaches capture some aspects of the microstructure, they do not overcome the complex shape of the snow crystals that affects the particle interactions, and thus the mechanical response is strongly simplified. The effects of the snow particle shape and the actual micro-mechanical contacts cannot be resolved. This was pointed out by Hagenmuller et al. [36] who studied diverse snow microstructures and their mechanical properties through DEM compression tests. They underlined the necessity of mechanical experiments in combination with CT scans to reduce the uncertainties of the microscopic contact parameters and to validate models. This problem, namely the comparability of experiments and simulations, can be tackled in two ways. First, on the modeling side, the representation of microstructure in DEM could be made more sophisticated [75] to represent the true microstructure by only using spheres. Second, it is possible to explore the problem also from the experimental side, and experimentally create synthetic microstructures that closely resemble ideal sphere assemblies.

Snow made of spherical ice particles has been prepared and used in several studies on sintering, the formation of solid necks at the contact points [15, 43, 54, 62]. The spheres were commonly produced by spraying water into liquid nitrogen or oxygen to obtain particles in a diameter range of 20 μm up to 4 mm. Ideally grown necks were observed in conformance with the theoretical prediction [43]. This renders systems of sintered ice spheres as ideal candidates for DEM models since the key entities of particles and contacts are well-defined. The contact size can even be modified by varying the sintering time. These are ideal precon-

ditions to examine microstructural and mechanical properties of an artificial microstructure comprising spheres. However, the size-dependent sintering process is faster on smaller particles, and the deviations from the ideal spherical shape, due to mass transportation from bulk to neck growth, are more pronounced on smaller particles. Therefore, rather large spheres seem practical to examine contact properties of a sphere assembly while preserving the spherical particle shape for a longer time.

In the present paper, we examine the potential of spherical model snow as a mean to close the gap between experiments and simulations of snow mechanics, that remains despite detailed CT imaging of the microstructure. The ice spheres with clearly defined shapes and contacts, seem to be an ideal intermediate step, to examine contact properties and facilitate a close model validation. We present a new method to create spherical model snow and idealized microstructures, together with a careful characterization of geometrical (spheres, contacts) and mechanical (elasticity and strength) properties. We seek to provide experimental data that can be used for actual DEM simulations. To this end, we developed a novel method for ice bead production and performed a detailed characterization of the particles in terms of particle size and sphericity, using CT images. For the mechanical characterization, unconfined compression experiments of sintered ice bead samples were performed in combination with 3D CT scans. The scans were used to analyze the microstructure and relate it to the mechanical response, and to compute the elastic modulus through FEM simulations as an additional macro-mechanical parameter. Two important contact parameters relevant for DEM (number of contacts, mechanical properties of contacts) were experimentally manipulated: some of the ice bead samples were densified to increase the number of contacts, and different sintering times were investigated to influence the size of the contacts between the particles. As a reference we performed experiments also with nature identical snow.

The results of the particle characterization, namely high sphericity and narrow size distribution, are ideal prerequisites for an experimental DEM analogon. The CT image analysis showed the reproducibility of the sphere assemblies, and can be applied for efficient reconstruction of the experimental sphere assemblies, as initial condition for simulations. However, the CT images revealed a complex geometry of the bonds after the manipulation by sintering with measurable impact on the mechanical properties.

The paper is organized as follows: The next section starts with the description of the production of the ice beads and snow samples, followed by the specification of the compression experiment. The CT-based methods for particle and structure analysis, as well as the simulation of the elastic modulus are explained together with a qualitative analysis of the ice bead crystallography. The order of particle and structure characterization, simulations of elastic modulus and compression tests is given in the result section as well as in the subsequent discussion.

3.2 Material and methods

3.2.1 Ice bead production

To meet the requirements of very round ice particles with a narrow size distribution, we constructed a tumbling machine to round off frozen water droplets, similar as in industrial methods like tumbling or barrel finishing [31]. The droplets were obtained by dropping deionized, purified water with a syringe on a Teflon sheet at -20°C. Using the syringe, the particles had approximately the same initial size. For the tumbling machine we mounted an aluminum can with a diameter of 15.5 cm on a rotary motor, sketched in Figure 3.1(A). The can is coated with sand paper (ISO grit P100) on the inside and closed with a cap during tumbling. The rotational velocity ($\approx 3\,\mathrm{s}^{-1}$) was chosen such that the granular flow kept in the rolling regime and no particles stick to the wall due to the centrifugal force. During tumbling the particles become smaller and round off by abrasion to a spherical shape. Tumbling velocity and time determine the size of the particles. For our analysis we produced ice beads in the size range of $2 - 2.2$ mm and we stopped the tumbling process once the particles passed a 2.2 mm sieve. Dust and smaller particles were sieved out with a 2 mm sieve. The frozen water droplets need to be tumbled for approximately 24 h at -20°C to turn into ice beads in this size range. A microscopy image of one exemplary particle is shown in Figure 3.2(B).

Within the scope of the present application, ice beads can be reused as they were not destroyed in the experiments. We did neither observe fractured particles after the experiment nor any changes of the regarded particle characteristics, like size or shape. However, before using them

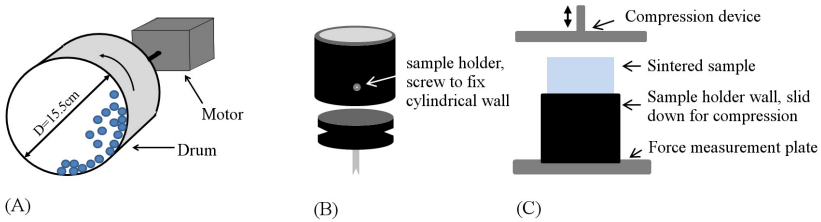

Fig. 3.1: (A) Sketch of the tumbling machine consisting of a cylindrical drum and a rotary motor. (B) Sketch of the sample holder and (C) the experimental set-up for the compression tests.

in a next experiment, they were tumbled again for about half an hour to smooth the surface which became rough during sintering.

3.2.2 Nature identical snow

As reference for the analysis and the mechanical tests, we included a prevalent and widely investigated snow type in the analysis with isothermally metamorphed rounded grains. The snow was produced in the lab using fresh, dendritic snow from a snowmaker [101] as base material. It was sieved into a Styrofoam box and stored at -5°C over three month. Rounded grains developed in a sub-millimeter size range (Figure 3.2(A)). According to Schleef et al. [101], who performed a comprehensive comparison of lab-produced and natural snow, we refer to this snow as "nature identical snow" and classify it as large rounded grains RG according to Fierz et al. [21].

For the compression tests, the snow was sieved with two sieves with mesh sizes of 1.4 mm and 0.7 mm, to obtain separated particles in a restricted size range. A 2D cross-section of a 3D binary CT image is presented in Figure 3.3(D). CT images were used to characterize the snow structure in terms of density and specific surface area (SSA).

3.2.3 Sample preparation

With the freshly tumbled ice beads we prepared cylindrical samples (Figure 3.2(C)) for the compression experiments. The sample holders consisted of a round base with a diameter of 33.6 mm and a cylindrical

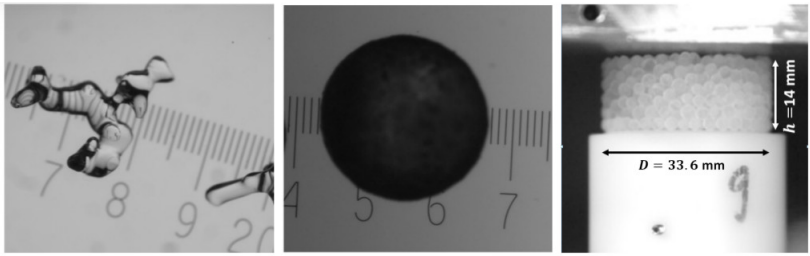

(A) (B) (C)

Fig. 3.2: Microscopy images of exemplary particles of nature identical snow (A) and ice beads (B), same scale (mm) in both images. (C) Sample of unconfined sintered ice beads, after removal of sample holder wall, before compression test.

wall around. The wall could be fixed on the base to fill in and sinter the particles, and slid down to perform the unconfined compression test (Figure 3.1(B-C)). The fixed cylinder wall determined the sample height of 14 mm. With the ice beads, we created two sample classes, namely compacted and uncompacted samples. For the uncompacted samples (referred to as poured beads), the wall was fixed and the particles were poured in. Before they were sealed with a lid to avoid evaporation, particles that stick out were carefully removed to flatten the surface, without pushing them into the sample. For the compacted samples (referred to as tapped beads) the cylindrical wall was held higher than 14 mm for filling in the particles and tapping them 30 times on the table, to densify the structure. After the tapping the wall was slid down and fixed to the same height of 14 mm, to flatten the surface and close the sample with a lid. The samples of the nature identical RG snow were prepared in the same way as the poured ice bead samples: the snow was sieved into the sample holder with the fixed wall and the surface was flattened by removing additional particles.

For sintering, the samples were then placed in a Styrofoam box in a -10°C cold room. The temperature during the entire sintering process was measured for the tapped samples. The fluctuation in the box was ± 0.5°C . For all sample classes we investigated different sintering times t_s. We chose two main sintering times with a higher number of samples and some sintering times in between, with less samples, to cover a

wider time-range. The numbers of samples per sintering time are listed in Table 3.1. The number of samples with CT scans is written in the parentheses and also counted in the total number of samples. We have chosen different main sintering times for ice beads and RG snow. This reflects the differences in sintering behavior of different snow types [41]. In the experiments we aimed to cover the time ranges with highest sintering rates, which are different for ice beads and nature identical snow.

Tab. 3.1: Overview of the tested samples per sintering time t_s. Number in parentheses is the number of samples with CT scan.

Samples	5 min	2 h	4 h	8 h	1 d	2 d	3 d	5 d	10 d
Poured	-	-	-	-	4	6	13 (2)	12 (2)	5 (2)
Tapped	-	-	-	-	-	-	-	7 (7)	7 (6)
RG snow	11	6	20 (3)	6	16 (3)	7	-	5	-

3.2.4 Unconfined uniaxial compression experiments

Unconfined compression experiments were performed to derive with the compressive strength a macro-mechanical property of the samples. The experiments were conducted at -10°C with a friction and compression testing machine described by Theile et al. [117]. To compress a sample it was fixed on a force measurement plate, where the outer wall of the sample holder was removed by sliding it down, as sketched in Figure 3.1(B-C). The unconfined specimen was then compressed to a depth of 8 mm with a constant velocity of 10 mm/s. A force - displacement curve was recorded with a sampling rate of 10 kHz. For the stress - strain conversion, the force was normalized by the circular sample area. Taking the sample area as contact area included the simplification of a constant area. The change of the actual contact area, due to falling out particles during compression, could not be recorded.

3.2.5 Micro-computed tomography

For some samples, 3D CT scans were taken before the compression tests by using a Scanco Medical CT 40 scanner, that is operated in a cold

room. The X-ray scanner was held constant at -10±1°C. The trade-off between scanning time and resolution led to a scanning duration of three hours and a voxel size of 18 μm, resulting in a sample dimension of about (2000×2000×800) voxel. With that, the entire cylindrical sample was scanned to allow for a complete reconstruction of all particles in the experimental samples, as input for DEM simulations, (Figure 3.3(A)). The scans were timed as close as possible to the compression tests (t_s − 3 h) to capture the final sintering state in the images, but some variations were unavoidable.

3.2.6 3D Image analysis

First, the grey images (Figure 3.3(B)) need to be segmented to define ice and air phase. For each image, the appropriate threshold was determined by fitting the sum of three Gaussian distributions to the greyscale histogram, as described by Hagenmuller et al. [35]. A sub-volume of the binary image was then used to compute the elastic modulus, as described below, and to determine the specific surface area SSA via interface triangulation. The triangulation based method is a standard evaluation of the CT images that is provided by the vendor software from Scanco Medical [42], for which a deviation of 5% was determined for a reference object with known surface area [37]. For the structural analysis of the samples, the image resolution was decreased by a factor two, for numerical reasons. The downscaling was performed on the grey images and therefore acted like a filter. The preservation of the mean grey value before and after downscaling implies the invariance of the air-ice ratio, thus the scaling should not affect the derived parameters (number and size of particles and number of bonds). For the scaling eight voxels were integrated into one before the threshold was determined and the images segmented, as described above. A 2D slice of the downscaled binary image is shown in Figure 3.3(C), where the ice phase is green (1) and the air is blue (0).

The subsequent image analysis was done in Python. The particles needed to be identified to determine the size distribution of the beads and to characterize the structure in terms of the number of particles n_p and the number of contacts n_b. In a first step, air bubbles in the ice phase had to be removed as they disturbed the segmentation process. This is achieved by identifying the largest connected air component and

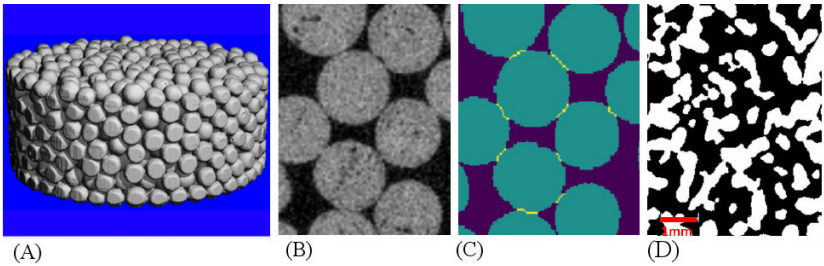

Fig. 3.3: CT images of the samples: (A) binary 3D image of experimental cylindrical ice bead sample (the particles at the rim appear flat, due to the chosen section, to cut out the sample holder wall). (B) 2D slice of ice bead sample, grey image with 18 μm resolution; (C) downscaled and segmented binary image, ice beads were identified using a watershed algorithm and the watersheds as contacts between the particles are depicted as yellow lines. (D) Binary microstructure of nature identical snow (white ice phase), identification of particles and contacts is ambiguous.

assigning all other voxels the ice value 1. On the bubble-free image a watershed algorithm was applied to identify the particles. This common algorithm is contained in the Python Scipy library. It is often used for similar problems and works well on clear defined shapes [110], as the ones of the ice beads. With a distance transform on the ice phase, local maxima are found around the center of the particles. From these points the watershed algorithm starts to "flood" the ice phase, until a constriction - a watershed - is reached. Such a watershed should be located at the contact, the narrow part between two particles. When the contacts were found the particles were identified. The watersheds themselves were counted as the contacts and are depicted as yellow lines in Figure 3.3(C).

To determine the size r_p of the ice beads, the voxels belonging to each particle were counted. Knowing the voxel size, we calculated the particle volume and translated this to the radius of an ideal sphere with equivalent volume. This method works well, given the spherical particle shape. For the sample density ρ the ice volume fraction ϕ was determined and multiplied by the density of ice, $\rho = \phi\rho_{ice}$.

3.2.7 FEM simulation of the elastic modulus

A voxel-based Finite Element (FE) code [25] was used to compute the elastic moduli of the samples. This was done to obtain a second macro-mechanical property, independent from the compression experiments. It has been shown by Gerling et al. [29] that this microstructure-based method can be considered as a reliable estimate of the true elastic modulus of snow. In the FEM code, effective elastic moduli are computed from volume-averaged stresses when the sample is subjected to a prescribed volume-averaged strain. We used the same parametrization as Gerling et al. [29] by assuming a microstructure made of isotropic, polycrystalline ice, with the ice bulk and shear moduli $K = 8.9\,\mathrm{GPa}$ and $G = 3.5\,\mathrm{GPa}$. The simulations were performed on a cubic sub-volume of the binary images with the original resolution of $18\,\mu\mathrm{m}$. For obtaining equivalent cutouts, we analyzed the vertical density profiles of the samples and cut the uppermost slices off at a comparable density value. The x- and y-dimensions were the same for all images and chosen such that a maximum cube was cut out of the cylindrical sample volume. The sample dimension was then $(1200\times1200\times650)$ voxel, corresponding to $(21.6\times21.6\times11.7)\,\mathrm{mm}$, with slight variations in the z-dimension.

3.2.8 Qualitative ice bead crystallography

As the internal crystalline structure of the ice beads is of potential relevance for model validation, we provide a fabric analysis, as part of the particle characterization. The analysis is based on polarized light microscopy [97]. This method for visualizing the internal crystalline structure exploits the crystal-axis-orientation dependent optical properties of ice. Thin sections of ice were illuminated under different angles and from the refraction of the translucent light the crystal orientation was deduced. Due to the absence of a calibration of the microscope, only a qualitative picture can be provided. This is, however, sufficient to visualize differences in intensity and to identify differently oriented grains. We examined 31 particles, a random selection of which is shown in Figure 3.4. The ice bead slices we analyzed in this way consisted of 1 to 10 crystals. While we observed several mono-crystalline beads, we could not find an ice bead consisting of more than 10 crystals. The expectation value and standard deviation was (2.3 ± 1.5) crystals per bead.

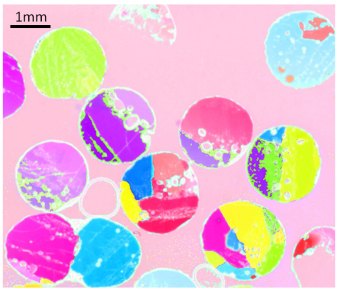

Fig. 3.4: Visualization of crystalline structure of several ice beads, ground to 50 μm thick slices. A mono-crystal is represented by one color.

3.3 Results

3.3.1 Characterization of ice beads and RG snow

The key requirements for the particles are a spherical shape and a narrow size distribution. To assess these properties, we analyzed the particle radius r_p and the specific surface area SSA. The particle radii r_p of the beads were calculated from all CT samples, with the average and standard deviation

$$\bar{r}_p = (1.12 \pm 0.1)\,\mathrm{mm}.$$

For the specific surface area SSA we obtained from all CT samples the average and standard deviation

$$\overline{\mathrm{SSA}} = (3.1 \pm 0.1)\,\mathrm{m^2 kg^{-1}}.$$

With a deviation of 6% this is very close to the SSA of an ideal sphere with the mean radius $\bar{r}_p$ of the ice beads, with $2.9\,\mathrm{m^2 kg^{-1}}$. Since the SSA, the surface to volume ratio, for a given volume is minimal for a sphere, this result implies that the ice beads are close to an ideal spherical shape. From these results, a measure of sphericity can be derived, by the ratio of the surface of a volume-equivalent sphere and the surface of an object [120]. For an ideal sphere, the sphericity is one, for the ice beads the computed sphericity is 0.92.

The nature identical snow was characterized in terms of density and SSA, both derived from the CT images. The respective mean values

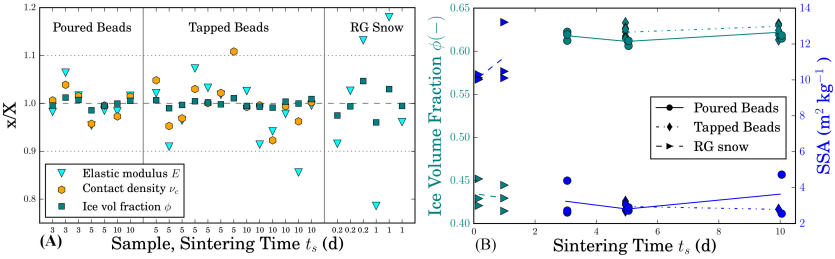

Fig. 3.5: (A) Structural parameters, $x = \nu_c$, ρ, and E normalized by the mean X of all images of one sample class are shown for all samples of the poured (left) and the tapped beads (middle) and for RG snow (right). The dotted lines indicate ±10%; the sintering time is denoted on the abscissa. (B) Ice volume fraction and SSA of all samples against the sintering time.

of the six samples are given by: $\overline{\rho} = (399 \pm 50)\,\mathrm{kg/m^3}$ and $\overline{\mathrm{SSA}} = (10.7 \pm 1.2)\,\mathrm{m^2 kg^{-1}}$.

The SSA of all CT samples, from RG snow and ice beads, is presented in Figure 3.5(B) together with the respective sintering time. The dotted lines indicate the averages and shows that the SSA is rather constant and no trend with sintering time can be seen.

3.3.2 Characterization of the ice bead structures

To demonstrate the reproducibility of the ice bead structures, we determined the number of particles n_p, the number of bonds n_b and the ice volume fraction ϕ as structural parameters from the CT images, Table 3.2. From these values we calculated the contact density $\nu_c = \phi Z_c$, as used by Gaume et al. [28], with the coordination number $Z_c = 2n_b/n_p$. For all samples these values, normalized by the mean of the respective sample class, are shown in Figure 3.5(A), for the poured (left) and tapped beads (middle). The standard deviation of less than 10% as indicated in the dotted lines underlines the reproducibility of the structures. The sintering time of the samples can be read on the abscissa. To relate these parameters to the elastic moduli, all values were determined from the cubic sub-volumes of the images which were used for the computation of the elastic moduli.

Tab. 3.2: Mean and standard deviation of the ice volume fraction ϕ, contact density ν_c and elastic modulus E.

	Poured Beads	Tapped Beads	RG Snow
ϕ	0.62 ± 0.01	0.63 ± 0.01	0.43 ± 0.05
ν_c	3.47 ± 0.1	3.6 ± 0.13	-
E (GPa)	1.03 ± 0.04	1.0 ± 0.11	0.44 ± 0.01

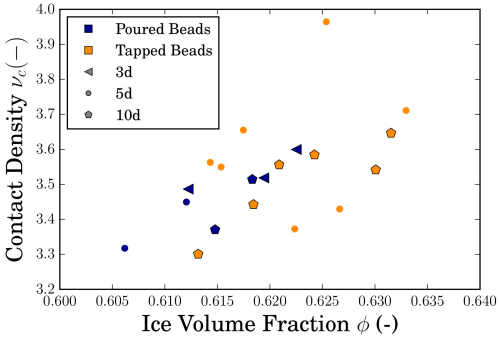

Fig. 3.6: The distinctiveness of poured and tapped samples in the contact density against the ice volume fraction: the tapped samples have by tendency higher densities and more contacts, but also more variability. The sintering time is indicated in the symbols.

To show the differences between the two sample classes, the contact density ν_c is plotted against the ice volume fraction ϕ in Figure 3.6. Although there is no sharp transition, it reveals the trend that the tapped samples have a higher density and more bonds per particle than the poured.

For the nature identical snow only density and elastic modulus are shown in Figure 3.5(A) (right), since no contact density could be determined. For both parameters the scatter is higher than for the ice bead samples and E exceeds the ±10% range.

3.3.3 FEM simulations of the elastic modulus

The results for the elastic modulus are shown in Figure 3.7, in (A) against the sintering time t_s of the respective sample and in (B) against the ice volume fraction ϕ. The contact density ν_c of the ice bead samples is color-coded and magnified in the inset. For the ice beads and the RG snow the values of E are clearly separated and each in a narrow range, between 0.34 and 0.52 GPa for RG snow and 1.2 and 1.5 GPa for the ice beads. Figure 3.7(A) distinguishes the two ice bead classes in symbols and colors and reveals a rather large scatter of elastic moduli for the tapped samples, compared to the poured. A relation with the sintering time cannot be extracted which indicates that the effect of sintering is not resolved in the images. Figure 3.7(B) shows the increase of E with the ice volume fraction, as expected from the literature [29, 57]. The inset shows the elastic moduli for the ice beads as a function of the two investigated parameters with a potential influence on E: on the abscissa is the ice volume fraction and the contact density in the colors. The general picture looks as expected: an increase of E with ϕ and ν_c. However a closer look and an intercomparison of the points reveals that examples can be found with similar ice volume fractions, and contact densities but different elastic moduli.

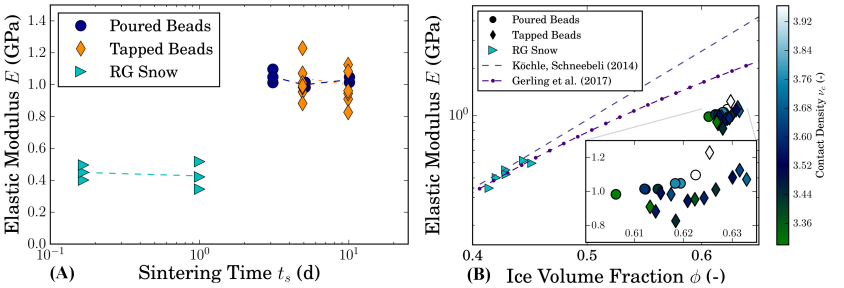

Fig. 3.7: Elastic moduli computed on the CT images: (A) against the logarithmic sintering time, the lines indicate the averages; (B) against the ice volume fraction, with the color-coded contact density for the ice beads. The inset shows a magnification of the ice bead results.

3.3.4 Compression experiments

For a visual inspection of the compression curves we show an example of a poured ice bead sample in Figure 3.8(A). The sample has been sintered for five days and shows the typical behavior observed in all samples: strongly pronounced peaks occur when clusters of particles fall out (Figure 3.8(B)), the stress drops until a new contact is formed and the sample further compressed. The sampling rate of 10 kHz proved to be high enough to resolve the fracture, as is depicted in magnification of the highest peak in the inset of Figure 3.8(A).

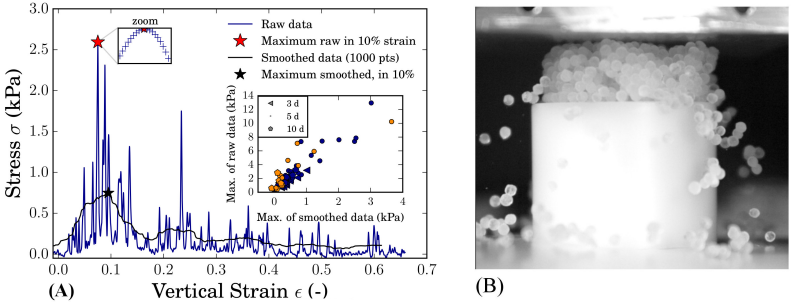

Fig. 3.8: Compression experiment of a poured ice bead sample after five days sintering. (A) Example of stress-strain curve as experimental result: the blue curve shows the raw data, the black curve its smoothed version, which was calculated with a moving average over 1000 data points. The magnification of the blue maximum shows that the sampling rate of 10 kHz resolved the fracture. The maxima within the first 10% of strain were extracted from each curve, as marked by the stars. The inset shows the relation between the maxima of raw and smoothed data. (B) Photography of sample during compression: single particles and clusters of particles break out and lead to the pronounced peaks shown in (A) and a changing contact area during compression.

In order to derive an objective characteristic of the rather irregularly shaped curves, the maximum within the first 10% strain (red star) was extracted from all curves. To examine its significance, it was compared to the maximum of the respective smoothed curve, which was calculated with a moving average over 1000 data points (black curve and star in Figure 3.8(A)). The correlation of the two maxima is presented in the

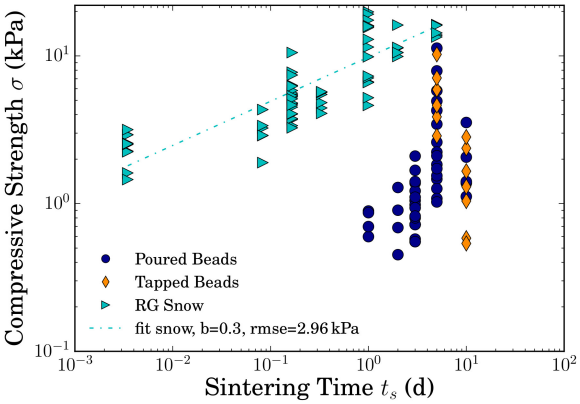

Fig. 3.9: The compressive strength of nature identical snow increases monotonously with sintering time, a power-law fit could be performed. For the ice beads, an increasing strength can only be observed up to five days. The ten-days-samples are weaker for both sample types.

inset for all ice bead samples. Despite the scatter, both definitions of strength are reasonably correlated and led to the same overall-picture (Figure 3.9), indicating the usability of the first definition. Therefore, the raw data maximum within the first 10% strain is considered as characteristic for the sample. It is presented in Figure 3.9 as compressive strength σ against the sintering time t_s, for all samples.

The log-log plot in Figure 3.9 summarizes all experiments of ice beads and RG snow. It shows the relation of compressive strength and sintering time and allows to intercompare the sample types. The RG snow sinters much faster and stronger than the ice beads, thus shorter sintering times were examined. A monotonic increase of the strength with sintering time was observed for the RG snow. In analogy to [41] we fitted the power-law $\sigma = a \cdot {t_s}^b$ to the data. For RG snow, a good fit (RMSE=2.96 kPa) was achieved with an exponent $b = 0.3$. For the ice beads no fit was possible. The strength increases monotonously only up to five days (poured) and decreases towards ten days again. The strength of the tapped samples exceeds the one of the poured after five days sintering, but it decreases after ten days to about the same value.

A high-speed video of an ice bead compression experiment is available in the supplementary material.

3.4 Discussion

3.4.1 Methods and ice bead characterization

In mechanical tests and CT-based investigations of ice bead packings, we examined the potential of spherical model snow. In the tumbling of frozen water droplets, we found a method to produce suitable, uniform ice spheres: the standard deviation of the size distribution is less than 10 % and the SSA is close to the one of a volume-equivalent ideal sphere, which implies high sphericity. Spherical shape and monodiseperse size are the main requirements for the experimental discrete element counterparts and critical for model validation. The sphericity, derived from the SSA, was constant for samples of different sintering times, implying the preservation of the spherical shape throughout the experiments (Figure 3.5(B)). The particle size can be modified by the tumbling time, and smaller particles with an optical diameter of natural snow crystals can be produced as well. The qualitative evaluation of the crystallography indicates that the ice beads consist of one to ten crystals. The growth of monocrystals would probably be favored under warmer conditions when the water freezes slower. This could be of interest for further sintering and optical experiments, or mechanical tests with the incorporation of the crystal orientation. So far, most 'spherical ice particles' presented in the literature [15, 62, 82] were produced by spraying water into liquid nitrogen and were not characterized in a similar way, which allows only qualitative comparison. A multicrystalline ice structure of particles with a 4 mm diameter was shown in SEM images [16], and on microscopy images these particles look less spherical than the ones presented here. Hobbs and Mason [43] report about mono- and poly-crystalline, monodisperse spheres with a diameter within one percent in the range of 20-300 μm. No measure for the sphericity was given. Therefore we believe that the mechanical tumbling method presented here is an interesting alternative to produce idealized model snow comprising spheres.

Besides the particle characterization, a well-working image processing with particle identification is the basis for our analysis of microstructure and contacts, as well as the reconstruction towards mapping onto models. To this end, a watershed algorithm could successfully be applied to the 3D CT images to identify the particles and characterize the sam-

ples in terms of the number of particles and contacts. The contact size, as second relevant contact parameter besides the number of contacts, is expected to change with sintering time. This was observed in the experiments through increasing compressive strength, but could not be derived from the images, which were analyzed regarding the watershed sizes (number of voxels of the watersheds, which were counted as contacts). The constant watershed sizes must be due to the image resolution of 18 μm and the fact that these narrow parts in the microstructure are most sensitive to binary segmentation, which comes along with a loss of information. However, the image processing can be applied for a complete reconstruction of the samples. Besides the contacts and number of particles, the position of all particles and contacts could be determined. Together with the high sphericity and quasi-monodispersity, this renders the system an ideal candidate for model validation: experimental samples can be reconstructed as input for (DEM) models for a close comparison.

3.4.2 Relation between microstructure and mechanics

The structural analysis of the CT images showed the reproducibility of the ice bead samples, with a standard deviation of the structural parameters of less than 10 %. The variation of density and elastic modulus of the RG snow samples was higher than for the ice bead samples. The densities of the ice bead samples lie in the range of a close random packing, which allows little structural variation. Yet, the effect of the sample compaction by tapping can be seen in higher densities and more contacts. The differences between the tapped and poured structures are small and without a sharp transition. But they are also mirrored in the mechanical properties, the simulated elastic modulus, and the experimentally measured compressive strength. While in the present paper the tapping was only employed as a proof of concept, a more systematic tapping method (using e.g. vibrations with a given frequency) may open the door for targeted manipulation of the packings.

Two main contact parameters were manipulated in the ice bead samples - the number of contacts by tapping and the size of the contacts through variation of the sintering time - and can be related to the mechanical response. The effect of sintering was not resolved in the CT images and consequently in the elastic modulus, for which a relation-

ship with the contact density and ice volume fraction was observed. The compressive strength is related to both parameters, even though only indirectly. Since the sintering time did not change the other structural parameter (SSA, density, contact density) that potentially affect the compressive strength, the increasing strength can be ascribed to the increase of the contact size. As the contact size matters but could not be quantified, no relation with contact density and compressive strength could be derived.

The Elastic moduli E were determined by voxel-based FEM simulations of 3D CT images. With a voxel size of 18 μm the image resolution was too low to resolve details of the sintering effect, as particularly the bond area is sensitive to the image resolution. Thus, no relation of E with sintering time was observed (Fig. 3.7(A)). E is dominated by the particle geometry and structural arrangement of the sample. While in snow science E is usually related to the ice volume fraction ϕ [57, 78, 111, 124], for the ice beads, we could additionally relate it to the contact density ν_c, which is shown in the colors of Figure 3.7(B). Regarding the relation with the ice volume fraction ϕ, the results of the RG snow samples are in very good agreement with the fits of Köchle and Schneebeli [57], and Gerling et al. [29] who utilized the same method. Their empirical power-law ($E = 2 \cdot 10^{-8} \cdot \rho^{3.98}$ (MPa)) fits with RMSE = 0.021 GPa our results for the RG snow samples. However, it overestimates E of the ice beads, as does the fit of Köchle and Schneebeli [57]. In both studies, the fits are restricted to a certain density range. Köchle and Schneebeli [57] even specify two fits for two ranges, which underlines the restricted validity. As their ranges do not cover the ice volume fractions of the ice bead samples, the fits are not expected to describe the elastic moduli of the beads. Yet, lower E are presumed towards higher ice volume fractions, as E must saturate at some point to the value of solid ice. The ranges of both, ice volume fraction and elastic moduli, are clearly separated for RG snow and ice beads, but the ranges of these parameters within the respective systems are small. The RG snow samples line up on the fit, i.e., clearly increasing E with ϕ. The ice bead samples, in contrast, are rather clustered. Partially this can be explained by looking at the contact density ν_c, as resolved in the magnification (Figure 3.7(B)), for which an increasing relation with E is expected [28] and seen in the results of the poured samples. For tapped samples, the relation is rather vague, due the the uncertainty intervalls of all parameters and their small ranges.

The higher variability of the tapped samples compared to the poured, is already observed in the relation of ϕ and ν_c (Figure 3.6) as well as in the relation of E and t_s (Figure 3.7(A)). This might be due to the sensitivity of the applied tapping method to small variations, whereas the pouring of the particles is better constraint.

The compressive strengths σ were extracted from the experimental stress-strain curves which are difficult to interpret on the first sight (Figure 3.8). The focus in this study was on a mechanical characteristic that allows for comparison of different sintering times and sample types, rather than on the fracture mechanism itself. Such a characteristic was found in the highest peak within the first 10% of strain and referred to as compressive strength, after an alternative evaluation of the smoothed curves and the deformational energy confirmed the results. The relation of compressive strength and sintering time (Figure 3.9) shows the reproducibility of the experiments, despite the large scatter, which however is typical for snow. The requirements for the representative elementary volume (REV) are met for the ice beads with 32 r_p and $n_p \in (1000, 1200)$ at the lower limit, which was found in 30 r_p [126] or $n_p \geq 1000$ particles [28]. In contrast, the requirements are clearly fulfilled for the RG snow samples. Yet, the experimental results have a similarly high scatter, which is considered to be the (reproducible) variability of the compressive strength. On the contrary, the scatter of the structural parameters is comparably small, within $\pm 10\%$. This indicates the relevance of the exact arrangement of the particles and the formation and mechanical importance of force bearing chains in snow structures [60].

Taking the highest peak of the stress-strain curves as compressive strength, as a characteristic of the sample, renders the comparison of different samples and sintering times possible (Figure 3.9). The compressive strengths of the ice bead samples reflect the variation of both contact parameters: tapped samples with higher contact densities exceed the poured samples; and for the poured samples an increasing strength with sintering times between one and five days was observed, assigned to the change of the contact size. A quantitative relation of strength, contact density, and contact size cannot be discussed, lacking information about the evolution of the sintered contacts. The relation of compressive strength and sintering time was examined in confined compression experiments and also related to the particle size [45]. A similar relation with time was found as we observed in the RG snow, but the increase

of compressive strength with particle size is in contrast to our results. Reasons for this are discussed in the next paragraph.

3.4.3 Effect of sintering on compressive strength and sintering anomaly of ice beads

In the relation of compressive strength and sintering time, large differences of RG snow and ice beads were observed. This relation has been investigated for snow in confined compression experiments [45], where an exponential fit was applied ($\sigma \propto e^{kt_s}$) that represented well the monotonic increase of the compressive strength with the age of snow. To the similarly progressing curve of the RG snow, however, we fitted a power-law $\sigma = a \cdot {t_s}^b$ in analogy to Herwijnen and Miller [41]. The exponent b is related to the standard sintering theory and links the locally and globally increasing strength. The obtained exponent $b = 0.3$ for the RG snow compares well to their ones for comparable snow (natural and nature identical rounded grains), considering the different densities. According to the standard sintering theory, the bond-to-grain ratio develops in time following the power-law

$$\left(\frac{r_b}{r_p}\right)^n = \frac{B(T)}{{r_p}^m} \cdot t_s, \tag{3.1}$$

with the temperature dependent B that captures geometrical and material properties. Assuming vapor transport as the dominant sintering mechanism for the regarded time scales [8, 15, 43], the exponents are $n = 5$ and $m = 3$ and the bond-to-grain ratio should grow in time with ${t_s}^{1/5}$. Hence, the relation of compressive strength and sintering time is due to the locally growing bonds and for the RG snow in good agreement with the literature.

Compared to the RG snow, the ice beads sinter much slower and weaker. First compression tests were initially performed after one day, but most of the ice bead samples fragmented when the outer wall of the sample holder was removed and could not be used for compression tests. In contrast, the RG snow could be tested after only five minutes. This difference can only partially be explained by the particle size. The size dependence of the sintering rate is prescribed by equation (3.1) that predicts decreasing sintering rates for increasing grain sizes, as do the simulation results of Herwijnen and Miller [41].

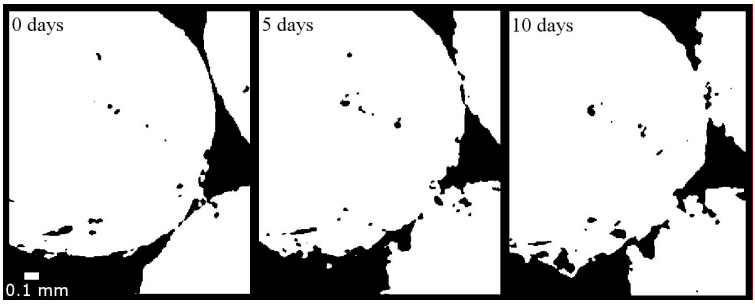

Fig. 3.10: High resolution (6 μm) CT scans of ice beads, after zero, five and ten days sintering. The 2D cross-sections of the binary images show porous bonds between the particles and their evolution.

The ice bead samples evolve similarly as RG snow but only for sintering times up to five days, with weaker but still increasing strength. Unexpectedly, the ten days samples were weaker than the five days samples, for both sample classes. This result presently lacks a sound theoretical explanation. However, the CT images and observations reported in the literature indicate that due to the porous nature of the bonds the growth is not monotonic. The results of the structural analysis and the elastic moduli - that show no variation with sintering time - do not indicate any remarkable differences in the structures of the ten days-samples, as they are not conspicuous, e.g. in the relation between E and ν_c. Moreover, different temperatures or large fluctuations of the temperature during the sintering process can be excluded from the temperature measurement of the five and ten days tapped sintering process. In both cases the temperature fluctuations were restricted to $\pm 0.5°\mathrm{C}$. The sintering theory behind equation (3.1) describes the growth of a solid neck between two particles in contact, as it developed for the RG snow. In additional CT images with higher resolution (6 μm), we observe porous bonds, several column-like structures form the contact between two particles (Figure 3.10). A very similar observation is described by Chen and Baker [15], for polycrystalline ice spheres of a 4 mm diameter under temperature-gradient and quasi-isothermal (-10°C) conditions, and by Adams et al. [1] for natural snow crystals (sieved with a 0.99 mm sieve). Chen and Baker [15] reported the growth of several "protrusions" from one particle to the other, forming a porous bond. Interestingly, they

report a retreat of the protrusions after growth of six days, but only if the protrusions could not get in contact with the opposite sphere (if the spheres were initially not in contact but separated by a small gap). The described images of the bonds were taken after six (maximum extension of the protrusions) and twelve days (retreated protrusions), which matches the time frame of our observation, the weakening of the compressive strength. Their observation is an optical one and no mechanical tests were performed. The retreat is reported only for initially separated particles. Our results show their mechanical relevance, i.e. weaker sintering of large ice particles and indicate that the reversal of bonding also takes place when the particles were in contact, i.e. that the porosity of an existing bond can increase in time. These results may help to explain the empirical observations of weakly sintered spring snow on ski slopes or roads, consisting of large and round grains, the weak layer potential of hail and graupel or even spherical ice particles in the food industry.

The porously growing bonds seem to be related to the particle size, as it has only been observed in 4 mm particles so far [15]. In other studies of sintering of ice spheres with diameters between 20-300 μm the growth of a solid neck was observed, as predicted by the theory [43, 62]. The size of our particles with 2-2.2 mm is in between. Though unexpected, our results fit the former observations, which indicate some effects for the sintering of large spheres that are not captured by sintering theory. The onset of these effects lies supposedly between particle sizes of 0.3 and 2 mm. Further investigation of this seems worthwhile to explore the size dependence and the mechanisms for these protrusions.

3.5 Conclusion

In this paper we presented a novel tumbling method for producing model snow that comprises highly spherical ice beads. We characterized the spheres and analyzed the structures and mechanics of sintered sphere assemblies. This showed that the investigated ice beads are well suited for snow model comparison, due to their clearly defined size, high sphericity and the well-working structural analysis by means of CT-imaging. The tumbling method presented here enables the production of uniform ice beads in different size ranges. Smaller and larger spherical ice particles than the ones presented here can be generated as well. The microstruc-

tures of the samples were characterized and related to the mechanical properties, by examining CT images of the samples that were used in the compression experiments. Microstructural variation was generated by densification of some samples and by variation of the sintering time. The sintered bonds of the ice beads developed with a complex geometry, contrasting the predictions from the standard sintering theory. This was observed by optical inspection of the CT images, as well as in the evolution of compressive strength with sintering time. In the compression tests, the ice bead samples exhibited after ten days sintering lower strength than after five, in contrast to the monotonic increase of the reference snow and the expectation from theory. The sintering artifacts, revealed in the CT images, impede the quantification of the contact size. Although unexpected in our experiments, similar observations are documented in the literature and indicate that the artifacts could be circumvent by utilizing smaller particles to allow for a complete quantification of the contact parameters (number and size of bonds). Despite these complications, the ice beads qualified also in the mechanical tests for model snow: until five days the ice beads developed a similar relation of strength and sintering time as the reference snow and the sintering-independent results of the elastic moduli, conform very well with the expectations from literature. Overall we believe that model snow comprising spheres with low variability in size and shape may be well exploited for applications such as DEM to address open questions regarding the calibration of contact parameters and the mapping of snow microstructure onto simplified geometries.

Angle of repose experiments with snow: role of grain shape and cohesion

4

Published in Journal of Glaciology:
Willibald, C., H. Löwe, T. Theile, J. Dual, and M. Schneebeli (2020), *Angle of repose experiments with snow: role of grain shape and cohesion*, Journal of Glaciology, 66(258), 658-666, doi:10.1017/jog.2020.36.

Abstract

Snow appears as a granular material in most engineering applications. We examined the role of grain shape and cohesion in angle of repose experiments, which are a common means for the characterization of granular materials. The role of shape was examined by investigating diverse snow types with discernible shape and spherical ice beads. Two geometrical shape parameters were calculated from X-ray micro-computed-tomography images after a particle-segmentation was performed with a watershed algorithm. Cohesion was examined by conducting experiments at six different temperatures between -40 and $-2\,^{\circ}\mathrm{C}$, assuming sintering as its cause, which accelerates with increasing temperature. As a cohesionless reference, experiments with glass beads were performed. We found that both shape and cohesion exerted about equally strong influence on the angle of repose. We utilized our results for an empirical model that describes the influence of shape and cohesion as additive corrections of the angle of repose of cohesionless spheres and explains all experiments with a correlation coefficient $r^2 = 0.95$. With temperature and the chosen shape parameter as fitting variables, previous experiments with another snow type could be consistently included. The experiments highlight the relevance of these parameters in granular snow mechanics and can be used for model calibration.

4.1 Introduction

The angle of repose is a classical measure for the investigation of granular materials [3]. As a characteristic of a granular material, it depends on particle and material properties such as size distribution and shapes of the granules, inter-particle friction, surface roughness and cohesion. These properties are examined in the angle of repose by means of experiments [96, 107], analytically [4] or numerically [131], for model parameter calibration, or to examine their influence on the flowability of a material in general. Thus, the methods and variables as well as the applications of angle of repose investigations are very diverse.

Given the broad spectrum of applications and influencing factors, angle of repose measurements are often discussed controversially. The criticism includes the restricted validity for cohesive materials, for which the lack of a clear slope angle inhibits the quantification of cohesion [96]. Moreover, the method is not standardized [3, 96]. To handle these drawbacks, it is recommended to clearly predefine the purpose of the angle of repose investigation and select the method accordingly [3], since it remains an important and interesting characteristic of granular materials.

Snow is often treated as a granular material (e.g. [34, 39]). For example, it turns into a granulate after fracture of the sintered, solid-like microstructure that is formed by accumulated snow on the ground. Its granular nature is therefore involved in most snow mechanical applications. Consequently, it has to be accounted for in numerical snow mechanical models, which motivated the work on identifying grains in a 3D snow microstructure by means of micro-computed-tomography (μCT) imaging [34, 116]. Yet to date, little experimental information is available, for an approach of granular snow mechanics on the grain scale, in particular about the role of grain shape and cohesion.

On larger scales, cohesion and its variation with temperature has been addressed by friction and strength measurements [98], or more recently in the context of avalanche rheology [58, 112]. In snow, cohesion is effectively mediated by sintering as a temperature and time-dependent process. Sintering is well investigated on time-scales of minutes, days and months (e.g. [8] and references therein). On sub-second scales, sintering has also been analyzed on the grain scale by investigating the contact of two spherical ice particles [32, 114]. In the latter experiments, sintering

strongly varied with temperature and was very weak below $-12°C$ but increased towards $-1°C$ [114]. Accordingly, sintering actually takes place within short contact times, but due to the high contact pressure, these results are not directly transferable to the granular behavior.

The variety of snow grain shapes is reflected by the variety of snow types [21]. For particles with complex shapes, such as snow crystals, no standardized measure for shape exists at this time [3]. Commonly used shape parameters such as sphericity or roundness [120] are derived from 2D projections of particles, usually from microscopy images. For snow, grain shape has never been characterized with respect to its influence on the granular behavior for diverse snow types.

Incorporating the grain shape into numerical models, such as in the discrete element method (DEM), is computationally and methodologically intensive [75]. However, given its mechanical relevance, it cannot be neglected. In DEM, the effects of shape are often accounted for by equipping spherical particles with a rolling friction coefficient (e.g. [125]). The calibration of this coefficient has been addressed for other materials with angle of repose experiments (e.g. [23]). For snow, no experimental information is available for differentiating the effects of non-spherical particles or different grain shapes.

To examine the roles of grain shape and cohesion in granular dynamics of snow on the grain scale, we performed systematic angle of repose experiments of diverse snow types over a wide temperature range (between -40 to $-2°C$). Previous angle of repose experiments with pulverized snow at different temperatures [63] are quantitatively included and discussed with our results. The snow type chosen by Kuroiwa et al. [63] complements our experiments by broadening the investigated parameter space of grain shapes. In our study, we investigated two of the most common snow types, rounded and faceted grains, and ice beads as spherical model snow. The ice beads are used to experimentally examine the differences in granular properties between real snow grain shapes and spherical particles as they are used in DEM. For a geometrical shape characterization of a large number of particles, we captured 3D μCT images of each snow type. For the segmentation of the particles, a watershed algorithm was applied, as it has been used for snow grain identification before [106, 116]. The role of cohesion is investigated by varying the temperature. By assuming that cohesion is caused by sinter-

ing, the cohesive forces should be negligible at low, and increase towards higher temperatures [114], resulting in increasing angle of repose.

This paper has the following structure: The material and methods section provides a description of snow sample production, the angle of repose experiments, the 3D μCT image analysis, and shape parameter determination. In the results section, the main findings are presented together with an empirical model that separates the effects of shape and cohesion. The discussion section follows the same order: main findings, role of shape and cohesion, and additionally contains a discussion of the role of particle size and implications of the findings in the context of snow mechanics and snow mechanical modeling.

4.2 Materials and methods

4.2.1 Preparation of snow samples

Two typical natural snow types were investigated with rounded and faceted grains, as well as spherical ice beads as model snow. All snow samples were produced in the cold lab.

For both natural snow types, fresh dendritic snow from a snow maker [101] was used as base material. To obtain rounded grains, the snow was sieved into a Styrofoam box and stored over three months in a $-2°C$ cold chamber, allowing for isothermal metamorphism. To grow faceted grains, the fresh snow was exposed to a temperature gradient for a duration of three weeks. The snow was sieved into a box with a heating plate at the bottom ($-3°C$), thick insulating Styrofoam plates as lateral walls, and was covered with a thin aluminum plate on the top to regulate the top-temperature with the $-22°C$ lab air. With a snow height of 15 cm, a temperature gradient of approximately 125 K/m was realized. According to Schleef et al. [101], we refer to these two snow types as nature identical snow. We classified them according to Fierz et al. [21] as rounded grains (RG) and faceted grains (FC).

The ice beads (IB) were produced by abrasion of frozen water droplets by tumbling them in a rotating drum as described in Chapter 3.2.1. As they were not destroyed in the experiments, the beads were reused several times without measurable impact on their properties (c.f. Chapter 3.2.1).

For equal conditions, they were tumbled for about half an hour before using them in experiments.

Between the experiments, the snow samples were stored at $-22°C$ to inhibit further metamorphism. Two to three hours before using the snow in the experiments, an adequate amount was transferred to the cold lab at the desired temperature for thermalization. Just before the experiment, the snow was sieved to prepare the granulate. Two sieve sizes were used to restrict the crystal size range as shown in Table 4.1. As listed therein, ice beads and faceted grains were investigated in two size-ranges, where the smaller ones are denoted with IBS and FCS, respectively. A microscopy image of a representative grain of each snow type is shown in the first row of Figure 4.1.

Additionally, experiments were conducted with industrial mono-sized glass beads (GB) as a cohesionless reference.

Tab. 4.1: Particle size range (sieve mesh sizes), parameters of the experimental angle of repose setup (base diameter D and falling height h) and investigated temperatures T with number of experiments per snow type.

Snow	Particle size	Setup (mm)		No. of experiments per T (°C)					
type	range (mm)	D	h	-40	-30	-22	-15	-5	-2
IB	4	70	25	8	8	8	6	6	7
IBS	2 - 2.2	50	40	8	8	8	-	8	8
RG	0.7 - 1.4	50	40	-	5	7	5	3	6
FC	1.4 - 2	50	40	8	8	8	4	8	8
FCS	0.7 - 1.4	50	40	6	8	8	-	7	8
GB	2	70	25	-	5	3	5	-	6

4.2.2 Angle of repose experiments

In our study, we focus on the influence of particle shape and cohesion on the angle of repose by comparing the angles of different snow types at various temperatures under identical experimental conditions. Our experimental setup consists of a round, freestanding base above which a sieve is mounted with a tripod to distribute the particles from a fixed height. The base was used to define a circular basal area and to allow

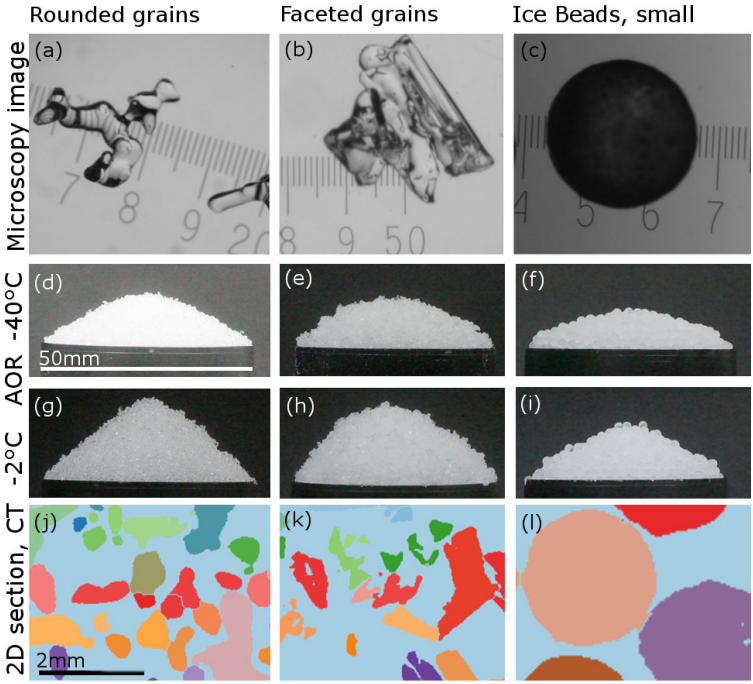

Fig. 4.1: Investigated snow samples in the columns; from left to right: RG, FC, IBS. In the rows: 1 (a-c) Microscope image of one representative grain (scale in mm). In row 2 (d-f) exemplary heaps showing the angle of repose (AOR) at $-40°C$ (RG at $-30°C$) and in row 3 (g-i) heaps at $-2°C$. Row 4 (j-l) shows 2D section of 3D μCT images after binary and watershed segmentation (same scale).

unstable particles to fall down without increasing the basal area of the heap. The base was chosen such that the for consistent measurements required ratio, $D/d \geq 20$ [3, 96], between base (D) and particle diameter (d) was fulfilled. For the large ice beads (IB), a larger base had to be used. The chosen values for height and base diameter are listed in Table 4.1. The height of the sieve above the base was constant and, for both bases, chosen such that it was slightly above the peak of the highest heap (e.g. RG at $-2°C$; IB at $-2°C$). The sieve separates the particles and prevents sintering before the heap is reached. The outlet of the

sieve covers the complete area of the base to obtain a uniform particle flow over the entire heap. The snow was filled into the center of the sieve, which was vibrated by manually rattling a spoon over the metal mesh at the edge of the sieve. About three times the mass of snow of the final heap was sieved onto the base to obtain a stationary heap. The sieving of the particles onto the heap took about 30 s. For each snow type and temperature, several angle of repose experiments were conducted, as listed in Table 4.1.

Angle of repose estimation from image analysis

After sieving, three images from different perspectives of the heap were taken. For each snow type, one example of a heap is shown for minimal and maximal temperature in Figure 4.1 (d-i). From these images, the angle of repose was determined, i.e. the slope angle of the heap towards the horizontal.

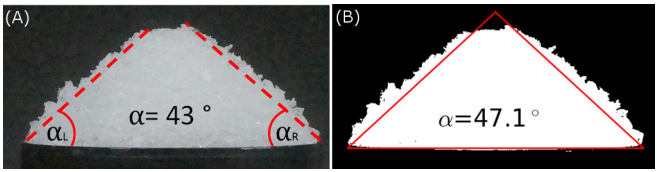

Fig. 4.2: Determination of the angle of repose α from the images with two independent methods: (A) shows the evaluation of the two lateral slopes with a line drawn by eye (method (a)); (B) shows the pojected heap-area to calculate angle of ideal area-equivalent triangle (method (b)).

Since snow does not form an ideal cone, the heaps may exhibit local variations and a flattened top that forms by the particle impact [96], which complicates the determination of the angle. We therefore evaluated the images by two different methods and determined the angle of repose using either (a) the two lateral slopes or (b) the projected heap-area. Both methods are sketched in Figure 4.2. For the slope-evaluation with method (a), a line was drawn through a representative part of the heap silhouette by eye. The angle between the line and the horizontal was determined as the slope angle. In this way, six angles per heap were determined, two for each of the three images, and their average was

taken as the angle of repose. For the area-evaluation with method (b), the projected heap-area was automatically determined from the images to calculate the angle of an isosceles triangle with equivalent base and area. In this way, three angles were determined and averaged per heap.

4.2.3 3D μCT image analysis

From all snow types we took one 3D micro-computed-tomography (μCT) scan to determine the two standard bulk characteristics, density ρ and specific surface area SSA (surface-to-mass ratio), and to examine the particle properties of shape and size. To this end, the snow was sieved into a sample holder with a diameter of 30 mm, similar to the sieving in the angle of repose experiment. The scans were taken with a Scanco Medical μCT 40 scanner[1], which is operated in a cold room at -10 ± 1°C. With the chosen voxel size of $s_{\text{vox}} = 15\,\mu$m, the scanning duration was 3.5 h for a sample height of 15 mm.

For the evaluation, a cubic section of the grey images consisting of (600×600×600) voxels, corresponding to (9×9×9) mm, was used. As a first step, the images had to be segmented to define ice and air phases. For each image, the appropriate threshold was determined by fitting the sum of three Gaussian distributions to the grey-scale histogram as described by Hagenmuller et al. [35]. The obtained binary images were then used for the analysis. The ice volume fraction ϕ (ratio of number of ice-voxels to total number of voxels) was used to determine the density $\rho = \phi\,\rho_{\text{ice}}$. The SSA was determined with an interface triangulation-based method, which is a standard evaluation of μCT images and provided in the vendor software from Scanco Medical [42]. From the SSA, the optical equivalent radius $r_{\text{opt}} = 3/(\text{SSA}\cdot\rho_{\text{ice}})$ can be derived as a measure of the particle size.

Particle segmentation

To segment the snow microstructure and identify single particles, we used the watershed algorithm in the Python library Skimage. 2D cross sections of the segmented images are presented in Figure 4.1 (j-l) for each snow type.

[1] We used 55 kVp for the peak energy and 145 μA for the current of the X-ray tube, and a sampletime of 600 ms.

Once the particles were identified, they were evaluated one by one. A small 3-dimensional sub-volume was created that contained exactly one of the segmented particles. First, the coordinates were used to check whether the particle is located at the edge of the sample volume, which implies that the particle is not outlined in its entire form. To analyse only "complete" particles, the edge-particles are ignored in the following evaluation.

The particle volume

$$V_{\mathrm{p}} = N_{\mathrm{vox}} \cdot s_{\mathrm{vox}}^3 \tag{4.1}$$

was evaluated by the number of voxels N_{vox} that constitute the particle and the voxel size s_{vox}. From the particle volume V_{p} the radius of a volume equivalent sphere was determined as r_{ws}, a measure of the particle size.

As particle shapes are classically evaluated from 2D projections [120], we determined all three projections of the particle onto the main planes, *x*-*y*, *y*-*z*, and *z*-*x*, to evaluate only the largest one. Then, in a similar fashion to the volume, the projected area of the particle A_{p} was calculated

$$A_{\mathrm{p}} = N'_{\mathrm{vox}} \cdot s_{\mathrm{vox}}^2. \tag{4.2}$$

The area of the smallest surrounding circle A_{s} was determined by the maximum extent of the particle. To this end, the largest distance of two points on the particle countour was determined using the `countours` function in the Skimage library. The particle perimeter P was calculated with the `regionprops` function in the Python Skimage library.

Shape parameters

Two common shape-parameters were calculated with the derived particle properties for each complete particle in the sample-volume. The sphericity is one important shape parameter, as defined by [120] with:

$$\psi_{\mathrm{s}} = \frac{A_{\mathrm{p}}}{A_{\mathrm{s}}}, \tag{4.3}$$

the ratio of the area of the projected particle A_{p} and the area A_{s} of the smallest surrounding circle, into which the entire projected particle fits.

This shape parameter ψ_s allows for a comparison with the experiments from [63], since ψ_s is the inverse of the parameter ϵ_a used therein. Additionally, we evaluated a second common shape parameter referred to as "shape-factor" by Shmulik et al. [107]

$$\psi_f = \frac{4\pi A_p}{P^2} \tag{4.4}$$

that contains the particle perimeter P. Both shape parameters (equation 4.3 and 4.4) are equal to one for a perfect sphere.

4.3 Results

4.3.1 Comparison of angle of repose estimates

The angle of repose of each heap was derived from the images using two independent quantities, slope and area. As an overall comparison of both methods, we show the respective angle of repose for all experiments in a scatter plot in Figure 4.3. The results of both analyses are clearly correlated with systematic lower values obtained from the slope-evaluation (method (a)).

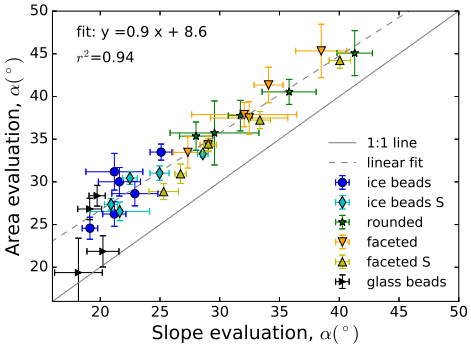

Fig. 4.3: Scatter plot of the two methods for evaluating the angle of repose.

In the following we only present the results of the slope-evaluation, since these results for cohesionless spheres (glass beads with $\alpha \approx 20\,^\circ$, ice beads with $\alpha(-40^\circ\mathrm{C}) \approx 21.5\,^\circ$) are consistently below the theoretically maximum stable angle of 23.4° [4], which, as a static angle, should be the upper limit.

4.3.2 Angle of repose of snow

All experimental results are shown in Figure 4.4 as the angle of repose of all snow types vs. temperature. One point represents the mean of all experiments at each temperature and the errorbar shows the standard deviation. Additionally shown are the results of the glass beads and the pulverized snow experiments, denoted by PS Kuroiwa[2]. The main observations of all snow curves can be summarized in two points. First,

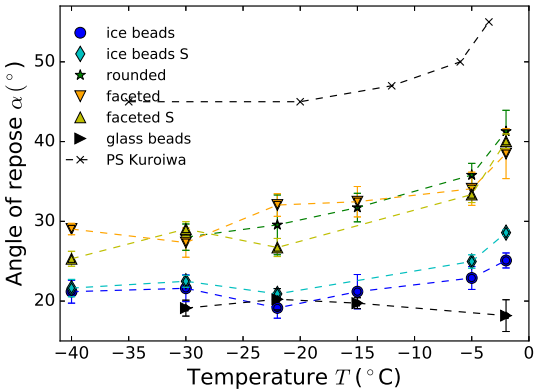

Fig. 4.4: Experimental results (mean values) for all angle of repose experiments against temperature. Error bars denote the standard deviation.

[2]Pulverised snow of Kuroiwa et al. [63]: For the angle of repose, the listed values were taken; for the particle characteristics the mid-value of the given ranges were taken, (i.e. for the shape ϵ_a = 1 - 2.5 we calculated with 1.75, corresponding to $\psi_s = 0.33$; for the particle size between 0.5 and 0.6 mm we used 0.55 mm). The experiments were conducted with a similar setup, where $D = 100$ mm and $h = 70$ mm.

the positions of the curves are clustered into three groups: the ice and glass beads exhibit the lowest angles, the faceted and rounded grains have clearly higher angles and the pulverized snow PS Kuroiwa has the highest angles. Second, the temperature-dependence of all snow types follows the same pattern: the angle of repose is rather constant at temperatures below $-15\,^{\circ}\mathrm{C}$ with some variations, but clearly increases towards higher temperatures with the highest slopes between -5 and $-2\,^{\circ}\mathrm{C}$. For the glass beads, no relation with temperature was observed.

4.3.3 Empirical model

To investigate how shape and cohesion affect the angle of repose α we assess an empirical model that treats both effects as additive corrections. With this, we follow former studies where the effects of shape (e.g. [107]) and cohesion [4, 87] are treated as corrections of the angle of repose α_0 of cohesionless spheres:

$$\alpha(\psi, T) = \alpha_0 + \Delta\alpha_\psi(\psi) + \Delta\alpha_\mathrm{c}(T). \tag{4.5}$$

The shape correction $\Delta\alpha_\psi$ should become zero for $\psi = 1$ and the cohesion term $\Delta\alpha_\mathrm{c}$ should become zero for very low temperatures. Accordingly, we employ $\alpha_0 = \bar{\alpha}_\mathrm{gb}$ as derived from the glass beads. For the shape term we assume $\Delta\alpha_\psi(\psi) = A(1/\psi - 1)$ with a free parameter A. For the cohesion term we assume an Arrhenius form $B \cdot \mathrm{e}^{-C/k_B T}$, which is reminiscent of the temperature-dependence of sintering as the assumed origin of cohesion. Besides the temperature T, it contains two free parameters B and C, and the Boltzmann constant k_B.

Based on these considerations, we fitted the following model of the angle of repose to all snow experiments, including PS Kuroiwa:

$$\alpha(\psi, T) = \bar{\alpha}_\mathrm{gb} + A \cdot \left(\frac{1}{\psi} - 1\right) + B \cdot e^{-C/k_B T}. \tag{4.6}$$

For the shape parameter, the sphericity ψ_s was chosen (if not specified otherwise), allowing for inclusion of PS Kuroiwa. A comparison of the fit and experiment is shown in Figure 4.5. With the mean values of ψ_s (Table 4.2), we obtained with a correlation coefficient $r^2 = 0.95$ the three fitting parameters $A = 13.3$, $B = 1.5 \cdot 10^{23}$, and $C = 1.2\,\mathrm{eV}$.

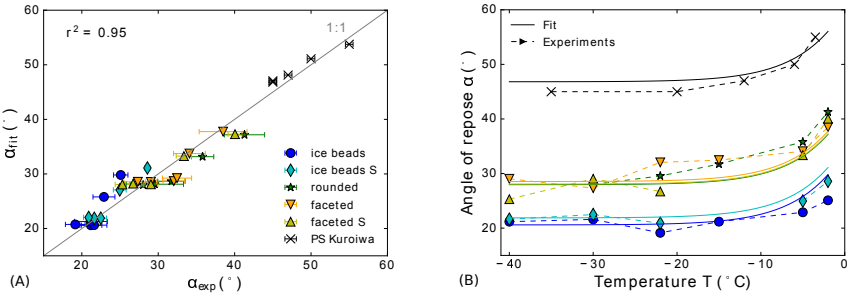

Fig. 4.5: Comparison of experiments and model fit (equation 4.6, with $\psi = \psi_s$), in (A) as a scatter plot, and in (B) against temperature.

Tab. 4.2: Snow and particle characteristics, derived from 3D μCT images and contributions of shape $\Delta\alpha_\psi$ and cohesion $\Delta\alpha_c$ from the experiments.

Snow type	ψ_s	ψ_f	r_{ws} (mm)	r_{opt} (mm)	ρ (kg/m^3)	SSA (m^2/kg)	$\Delta\alpha_c$ (°)	$\Delta\alpha_\psi$ (°)
IB	0.91	0.81	1.22	1.29	559	2.1	3.9	1.5
IBS	0.84	0.71	0.74	1.0	541	2.7	7	1.9
RG	0.61	0.56	0.28	0.26	267	10.6	13.3	8.3
FC	0.59	0.49	0.32	0.29	321	9.6	9.5	7.6
FCS	0.6	0.5	0.31	0.25	403	10.9	14.7	9.4

4.3.4 Sensitivity tests

To further illustrate both correction terms in the experiments, first the influence of shape was investigated at the lowest temperature $T_{min} = -40°C$, where cohesion is assumed to be negligible ($\Delta\alpha_c(T_{min}) = 0$). Under this assumption, equation 4.5 leads to:

$$\Delta\alpha_\psi(\psi) = \alpha(\psi, T_{min}) - \bar{\alpha}_{gb} \tag{4.7}$$

which describes the offset of the curves from the average of the glass bead experiments. This was calculated for all snow types as listed in Table 4.2. It is shown together with the shape contribution of the model against the variable $(1/\psi - 1)$, which shows the similarity for both shape factors ψ_s and ψ_f in Figure 4.6(A).

Second, the effect of cohesion was calculated at the highest temperature $T_{\max} = -2°\mathrm{C}$, where it is supposed to be maximal. According to equation 4.5, the cohesion term can then be written as

$$\Delta\alpha_c(T_{\max}) = \alpha(\psi, T_{\max}) - \alpha_0 - \Delta\alpha_\psi(\psi) \approx \alpha(\psi, T_{\max}) - \alpha(\psi, T_{\min})$$

which gives the difference of the angle of repose at maximal and minimal temperature, i.e. the maximum cohesion induced change of the angle. This was calculated for all snow types as listed in Table 4.2. It is shown in Figure 4.6(B) against the particle radius r_{opt} to examine a potential influence of particle size. The results indicate an additional influence of particle size which is not captured by the model (constant line). A qualitatively similar variation of the angle of repose with particle size is observed if only the increase at the highest temperature is considered ($\alpha(-2°\mathrm{C}) - \alpha(-5°\mathrm{C})$). These values are also shown in Figure 4.6(B).

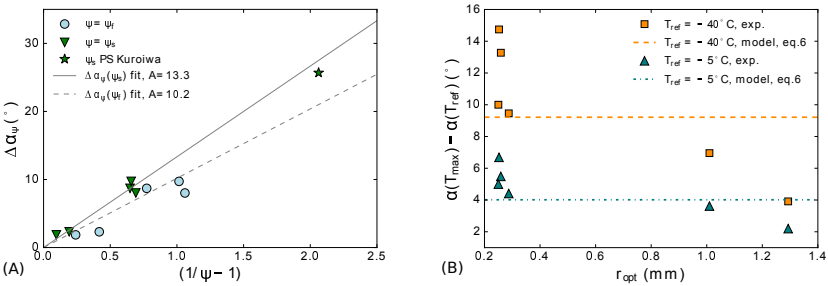

Fig. 4.6: (A): shape-contribution $\Delta\alpha_\psi$ of experiments (equation 4.7) and model ($A(1/\psi - 1)$) for both shape parameters, ψ_s and ψ_f. (B): cohesional-contribution $\Delta\alpha_c$ of experiments against μCT-derived particle radius r_{opt}: orange-squares show the maximum T-induced change and green-triangles show the change between the two highest temperatures; in the model, the cohesional-contribution only depends on T.

4.4 Discussion

Angle of repose experiments are a common means to characterize the granular behavior of a material, investigate particle and material prop-

erties, and derive parametrization for numerical models [3]. We performed systematic angle of repose experiments of diverse snow types over a wide temperature range to examine the role of particle shape and cohesion/sintering in the granular behavior of snow. Towards calibration of DEM parameters, we worked out differences in the granular behavior of natural snow and spherical particles, as well as the influence of sintering that takes place in angle of repose experiments.

4.4.1 Main findings

In the experiments, we observed a significant influence of particle shape and cohesion, with both factors increasing the angle of repose. The influence of shape was revealed by examining different snow types and spherical particles, and the cohesion, assumed to be caused by sintering, was examined by varying the temperature. Complex shaped snow particles clearly formed larger angles than the spherical particles. More specifically, the smaller the shape parameter, the larger was the angle of repose. The influence of cohesion was negligible at temperatures below $-22^{\circ}\mathrm{C}$, but increased as the temperature increased to $-2^{\circ}\mathrm{C}$.

Previously, the effect of both factors has been described as an additive correction to the angle of repose of cohesionless spheres (for the shape [107] and for cohesion [87]). Following these ideas, we assumed additive and independent corrections of both effects as a starting point for an empirical model (equation 4.5). The resulting empirical model fits the experiments very well ($r^2 = 0.95$). As fitting variables we used ψ_{s} from the μCT images and the temperature T as a proxy for sintering. This led to a quantitative understanding of the angle of repose of diverse snow types over a wide temperature range and the ability to examine shape and cohesion separately.

4.4.2 Effect of particle shape

The influence of particle shape was investigated at the lowest temperature, $-40^{\circ}\mathrm{C}$ (RG snow at $-30^{\circ}\mathrm{C}$). For the spherical particles, IB, IBS and GB, α is 21.2, 21.6 and 19.7°, respectively, and is in good agreement with former measurements of the angle of repose of dry, cohesionless spheres with $\alpha \approx 22^{\circ}$ [107]. These results are also in accordance

with the theoretically derived, geometrically maximum stable angle for spheres under static conditions of 23.4° [4], considering that the particle impact in the dynamic experiments lowers the angle. To extract the effect of particle shape in terms of the offset (equation 4.7), the glass beads were used as a reference. The values of $\Delta\alpha_\psi$ for ice beads (IB, IBS) and nature identical snow types (RG, FC, FCS) were in two separated but small ranges. This is consistent with the results of the μCT-derived shape parameters (Figure 4.6(A), Table 4.2).

In the model, the effect of shape is represented by $\Delta\alpha_\psi(\psi) = A\left(\frac{1}{\psi} - 1\right)$, which vanishes for perfect spheres with $\psi = 1$. The fit for $\Delta\alpha_\psi(\psi)$ matches the experimental offset very well for all snow types, including the pulverized snow (PS Kuroiwa). For the fit, the sphericity ψ_s is used as shape parameter because it was also available for PS Kuroiwa. If instead a different shape factor ψ_f (equation 4.4) is used in the model fit, similar results are obtained. This is demonstrated by the comparison in Figure 4.6(A).

In other studies of particle shape in angle of repose measurements [107], analogous empirical fit functions were used, which assume an additive correction of the angle of repose of spheres. A similar, non-linear relation was observed, where the angle increased as the shape parameter deviated from that of a sphere.

4.4.3 Effect of sintering

The observed temperature-dependence of α is consistent with previous results on ice sintering: Szabo and Schneebeli [114] investigated sintering of spherical ice particles with short contact times, in the second-range, at different temperatures. They measured almost no effect of sintering at $-23°\mathrm{C}$, and the largest effect at $-1°\mathrm{C}$. In our experiments, we observed quasi-constant angles for temperatures below $-22°\mathrm{C}$, as the measured variations appear rather random in all snow types and also for the non-sintering glass beads. In contrast, α clearly increased at higher temperatures, between -15 and -5, and even more between -5 and $-2°\mathrm{C}$. To account for this temperature dependence in the model, we assumed an Arrhenius form for the contribution from cohesion $\Delta\alpha_\mathrm{c}(T) = B \cdot \mathrm{e}^{-C/k_B T}$, which was motivated by sintering theory [30, 61]. The Arrhenius rate depends only on the temperature and thus provides the same relation with temperature for all snow types. The experimen-

tally observed relation of the angle with temperature, below and above $-15°\mathrm{C}$, is reflected well.

While the Arrhenius factor is included in the model on empirical grounds, the fitted parameter for the activation energy $C = 1.2\,\mathrm{eV}$ (with shape factor ψ_s in equation 4.6) is a factor of two larger than the activation energy given ([30], p. 527) for surface diffusion with 0.61 eV. Surface diffusion is one of the predominant sintering mechanisms in the early stage and assumed to be an early contributor [8, 30, 43]. In the fast sintering study of ice [114], the sintering in the sub-second time-range is explained by the freezing of a liquid-like layer on the particle surface in combination with creep of ice, which increases the contact area over time. The activation energy 1.33 eV given therein for the creep rate is consistent with our obtained value for C, and explains their experimental observations of fast sintering well. Indeed, a more comprehensive comparison with sintering would require actual contact times, which could not be assessed in our experiment. A rough estimate can, however, be obtained from the particle rate (approximate number of particles and duration of experiment) over the heap surface-area. Assuming equally distributed particle flow over the heap, a particle rests approximately one second on the heap before a next particle falls on top of it.

Often, sintering is discussed in close connection to friction, which constitutes another temperature dependent process for ice. However, its role in the angle of repose is not clear. While it is the key parameter in Mohr-Coulomb theory, which is often used for a theoretical analysis of the angle of repose [74], other studies conclude that friction plays a sub-dominant role behind particle shape and cohesion, and can therefore be neglected [87].

4.4.4 Uncertainties

Angle of repose method

Although the angle of repose method is criticised for lacking standardization, it has been and continues to be used as a common technique to characterize diverse properties of granular materials [3]. We focused on particle shape and cohesion, and investigated their influence on the angle of repose under identical experimental conditions. The uneven heap surfaces, due to particle extension and cohesion [96], complicate

the definition of the angle. However, given the correlation between the two independent angle evaluation methods from the images (Figure 4.3), the observed influences of shape and cohesion were significant. In view of the offset between the two methods in Figure 4.3, the good agreement of values for cohesionless spherical particles from literature [87, 107] with our results (IB, IBS at low T and GB) from the slope-evaluation-method supports the choice of this method over the area-method.

Watershed segmentation

The performance of the watershed-algorithm on a snow structure is difficult to estimate. From visual inspection of the segmented μCT images (Figure 4.1 (j-l)), the comparison of shape parameters with the experiment (similar α for particles with similar ψ) and the agreement of different measures for particle size (optical radius r_{opt}, watershed-derived radius r_{ws} and the size range defined by sieving, Table 4.2) let us conclude on a meaningful particle-segmentation of the structure (Figure 4.1). Applying the watershed segmentation enables the automated characterization of a large number of particles.

Role of particle size

The main features of the experiments were explained with particle shape and sintering, while the particle size has been disregarded in the empirical model. For cohesionless, spherical particles, the particle size should play no role [4, 87, 107]. This is consistent with our bead experiments (IB, IBS at $-40°\mathrm{C}$ and GB). However, size should actually be discussed in the context of both influencing factors. For non-spherical particles, larger angles were observed for smaller particles [10, 63]. Our experiments with non-spherical particles do not reveal a clear relation with particle size, due to the variation of α at low temperatures and the narrow range of the values (i.e. at $-30°\mathrm{C}$, where the curves are close together, the order of the curves is in the order of particle sizes, however it is the other way around at $-40°\mathrm{C}$). For cohesive materials, the angle is expected to increase with decreasing particle size [63, 87]. This relation is expressed with the Bond number ($F_{\mathrm{c}}/F_{\mathrm{g}}$), the ratio of the cohesive force and the gravitational force that acts on the particle. It decreases as F_{g} increases with particle sizes, assuming F_{c} =const. A similar effect

(increase of α for decreasing particle size) can also be derived from sintering theory [61], where the contact growth is a function of grain size and smaller particles sinter faster. In our experiments, a size-dependence of sintering cannot clearly be discussed. However, some observations can be noted: For both ice beads and faceted grains, the smaller particles exhibit larger angles at $-2°\mathrm{C}$ (strongest effect of sintering), and, more obviously, the total change of the angles with temperature, $\Delta\alpha_c$, increases with decreasing particle size (Table 4.2 and Figure 4.6(B)). Although the dependence on size is too weak for improving the model fit by taking it into account, the relation with particle size, as (slightly) indicated in the experiments, is in accordance with the literature for both factors.

Model uncertainties near the melting point

The behavior of snow is very sensitive to small temperature changes when T approaches $0°\mathrm{C}$. Further experiments between $-2°\mathrm{C}$ and $0°\mathrm{C}$ would have been interesting, but could not be performed in a reliable way. Even small fluctuations in the temperature would have large implications on the behavior, since melting would complicate the interpretation considerably. Other effects (e.g. from capillary forces) would not be discernible from the effects of dry sintering, which we focused on in this study. Two points which we expect to be important for temperatures between -2 and $0°\mathrm{C}$ should be mentioned here for the interpretation of the two model parameters B and C that describe the increase of α with temperature (equation 4.6). First, for temperatures between -2 and $0°\mathrm{C}$, we would expect even stronger increases in α than between -5 and $-2°\mathrm{C}$ for all snow types, which might not be captured in the presented B and C. Second, these two parameters describe the increase for all snow types in a similar way and represent the mean experimental increase for all snow types. This implies (as shown in Figure 4.6(B)) that the model overestimates the effect of sintering for the ice beads and underestimates it for the nature identical snow types. The figure, moreover, shows that not only the total change of α over the entire temperature range differs with snow type, but also the increase of α between -5 and $-2°\mathrm{C}$. The remaining differences in the increase of α with T for different snow types might be interpreted as a non-additive (coupled) effect of shape and cohesion. The number of contacts of a particle with the heap naturally depends

on particle shape and each contact contributes to cohesion by sintering. Thus, for enhanced sintering ($T > -2°C$), the model assumption (independence of shape and cohesion) might be less justified. Despite these limitations, the experiments show the significance of sintering at high temperatures and the model provides an estimate of this effect.

4.4.5 Implications on snow mechanics

The systematic angle of repose measurements of diverse snow types and temperatures give new insights for model applications and for snow mechanics in general. The characterization of the grain shape was based on the successful watershed segmentation of the 3D images, which allowed for the determination of two common shape parameters for a large number of particles. The shape parameters and the angles of repose were similar for the two natural snow types (RG and FC). This contrasts the large differences in microstructural and mechanical properties of these two snow types in the (non-granular) sintered, solid-like state [36, 41, 111]. The successful fit of the model suggests that the chosen shape parameters can be linked to the granular behavior and vice versa, as it relates shape parameters and angles, and also represents the PS Kuroiwa snow. The latter underlines the importance of shape in the angle of repose experiments, as it widens the parameter space. Thus, shape should be taken into account appropriately for modeling the granular mechanical behavior of different snow types.

Another application of the results concerns fast sintering of snow. Previous sintering experiments of ice on a sub-second time-scale [114] were not transferable to snow rheology due to the high contact pressures applied. The angle of repose experiments showed that sintering takes place at short contact times with a measurable impact on snow rheology even in the absence of high pressure. Even if the experiments do not quantify sintering explicitly, the successful fit allows for a quantitative comparison with sintering rates from the literature. The indirect observation of sintering here may shed light on previous observations related to the change of rheological properties of avalanches when temperatures approach $0°C$ [58], or on the smoothing of a landscape during snowfall [22], and can provide help for a numerical description of these processes. The effect of sintering on the angle of repose is of the same order of magnitude

as the effect of particle shape ($\Delta\alpha_c$ and $\Delta\alpha_\psi$ in Table 4.2). Similarly to the shape, it should be accounted for in numerical simulations.

4.5 Conclusion

The angle of repose experiments of all snow types and temperatures can successfully be described by an empirical model that accounts for the effect of shape and cohesion with additive corrections to the angle of repose of cohesionless spheres. This rendered the detailed investigation of both factors possible and the quantification of their influence on the experiments. Shape and cohesion exert about equally strong influence on the angle of repose of snow. These experiments showed that sintering actually takes place in snow within very short contact times (approx. 1 s) in the absence of high pressure, with measurable impact on the granular dynamics of snow. For the two nature identical snow types RG and FC, the angle of repose was similar, as predicted by the shape parameter. This is a remarkable result considering the large difference in the mechanical behavior of the sintered, non-granular microstructure for these two snow types.

Instability in sintering of ice spheres: Size-dependence and retreating bonds

5

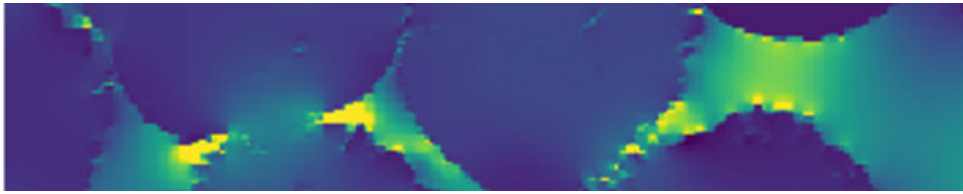

Submitted to Acta Materialia (January 2021)

Abstract

Anomalies in the sintering of ice spheres were observed in a few previous studies as protrusions and porously sintered bonds. These anomalies were explained using Mullins-Sekerka theory, which describes the evolution of a small perturbation on a crystal surface. Instability - growth of the perturbation - occurs due to enhanced vapor deposition on the exposed perturbation if a critical particle size (or rather curvature) is exceeded. The quest for the critical particle size and the potential of protrusion retreat by changing growth conditions motivates our ice sphere sintering experiments. Six samples varying in particle diameter from 1 mm to 2.3 mm were sintered over ten days at -10°C and then imaged by 3D micro-computed tomography. For two additional samples with small (1 mm) and large (2.1 mm) particles, we captured the sintering evolution through time-lapse tomography imaging. Surface and bond properties were quantified using various image analysis methods. These analyses revealed solidly sintered bonds in small, and porous bonds in large particles. The results indicate that the critical particle size must lie between 1.2 and 2.1 mm for experimentally relevant temperature conditions. Finite element simulations of the temperature field within the sample revealed higher temperature gradients between the particles in the bond region, with local maxima at the protrusion tips, which drive the protrusion growth. The temperature gradients, as well as the bond porosity decreased after an initial increase up to five days, indicating the retreat of protrusions. The results quantify microstructural aspects of this type of anomalous sintering and allow for its interpretation as self-inhibiting bond growth. As bonds affect the physical properties of a sintered material, the results are practically relevant for a wide field of applications, including sphere sintering experiments, road and piste preparation, food industry, and research on icy planetary bodies.

5.1 Introduction

Sintering is a crucial process in hot temperature materials that alters and dictates their properties through the growth of intergranular bonds. A hot material, in terms of the homologous temperature, is close to a phase transition and thermal energy is available for atomic movement, a precondition for sintering. Water-ice is a typical and ubiquitous hot temperature material in our daily lives, for example as snow or in food, where sintering plays a central role.

During sintering a solid connection is formed between single ice crystals, often called neck or bond, by transporting mass to the contact region. Various mass transport mechanisms on an atomic scale contribute to the sintering process, including vapor diffusion, surface and grain boundary diffusion, and plastic flow [8, 61]. Mathematically, these processes can be described by a generalized power law [61],

$$\left(\frac{r_\mathrm{b}}{r_\mathrm{p}}\right)^n = \frac{B(T)}{r_\mathrm{p}^m} t \tag{5.1}$$

which specifies the sintering mechanism in the two integer exponents, n and m, as well as in the temperature and material dependent B. Equation 5.1 describes the bond growth in time t in the ratio of bond radius r_b and particle radius r_p , assuming a circular or cylindrical neck geometry. In various experimental sintering studies with spherical ice particles, necks that conform this growth law were observed and used to examine the transport mechanisms [43, 54, 62]. This law was also used to investigate sintering of snow, e.g. [41, 129].

However, deviations from this sintering theory have been reported during sintering of large spherical ice particles [15] as well as for non-spherical snow particles [1]. Both studies describe the evolution of needle like structures on the particle surfaces, referred to as protrusions, which formed a porous bond in the contact region. Moreover, they report from visual observations that some of the protrusions retreated after several (∼seven) days, if they did not reach the other particle's surface. The porous nature and the retreat of the bonds explain the peculiar mechanical behavior of the weakly sintered ice spheres in compression experiments and the decrease in compressive strength after seven days

(Chapter 3.3.4). This underlines the mechanical relevance of the nature of sintered bonds.

In an investigation of the protrusions on 4 mm spheres [16], the protrusion length scale was related to the surface perturbations for which Mullins-Sekerka theory predicts an instable interface. The authors concluded that an instable ice-air interface facilitates the growth of small perturbations on the crystal surface, which led to the evolution of the observed protrusions. The theory on interface instability during diffusion or heat controlled crystal growth by Mullins and Sekerka, describes the fate of a small perturbation on a crystal surface [84, 85]. A perturbation that protrudes into a diffusion field is exposed to a higher concentration gradient than its surroundings and is therefore prone to growth. At the same time, capillary forces act on the perturbation, which tend to minimize the surface and reduce the surface energy. These competing mechanisms lead either to a stable interface when a perturbation decays, or to an unstable interface, on which a protrusion may grow. The dominance of the mechanisms depends on the length scale of the perturbation and the particle radius. A central outcome of this theory is that, for a fixed supersaturation, the instability only occurs for particle sizes larger than a critical size R_c [84]:

$$R_c = \frac{14\Gamma_k}{(c_\infty - c_0)/c_0}. \tag{5.2}$$

The particle radius R_c depends on the capillary constant Γ_k, as well as the degree of saturation, which is described by the concentrations in the far field c_∞ and at the interface c_0 [1]. However, the value Mullins and Sekerka obtain for R_c, seven times the critical radius of nucleation theory ($= 2\Gamma_k/(c_\infty - c_0)/c_0$), may only be seen as lower limit, as for prominent instabilities orders of magnitude larger values for R_c are required [84]. The radius quantifies the surface curvature H ($= 1/R$ for spheres), which strongly affects the local diffusion field and as such crystal growth. Theoretical instability studies [70, 81, 113] highlight the important roles of temperature, saturation, and thermal conductance of the system. Overall, these theoretical investigations are crucial for

[1] Note that equation 5.2 describes R_c for the second spherical harmonic $l = 2$, which defines the simplest geometry of the perturbation. An arbitrary perturbation geometry can be described by superposition of spherical harmonics, then equation 5.2 reads $R_c(l) = [(1/2)(l+1)(l+2)+1]\Gamma_k/(c_\infty - c_0)/c_0$.

understanding the evolution of surface instabilities, but a prediction of their occurrence is complicated by their sensitivity to complex growth conditions [16].

Surface instabilities during crystal growth may also occur during sintering via vapor diffusion [16]. Their dependence on particle size can explain the different outcomes of sphere sintering in the experiments described above, where solid necks were observed for sphere diameters of 0.02 to 0.7 mm [43, 62] and porous bonds for 4 mm spheres [15]. It can be expected that the critical particle size R_c lies in this range, between 0.7 and 4 mm. Unfortunately, no systematic experiments on the size dependence are available for particles in this range, although this is a common size range for ice crystals as snow grains (for example in a natural snow pack with advanced metamorphism, on ski pistes and roads in spring), or in the food industry [91, 109]. Because the quality of the sintered bonds affects physical properties (thermal, optical, and mechanical), better knowledge about sintering in this particle size range is important.

To fill this gap and investigate the size dependence and the nature of sintering and growth conditions between ice spheres, we conducted ice sphere sintering experiments with particle sizes between 1 and 2.3 mm in diameter. Sintering proceeded over ten days at -10°C and the results were captured via 3D micro-computed tomography (μCT) imaging. For six samples with different particle sizes, we only captured the final state (referred to as size series). For two additional samples with 1 and 2.1 mm particles, we observed the sintering process in time-lapse μCT scans, with images after 0, 3, 5, 7, and 10 days (time series). Using various image analysis methods, we determined the specific surface area and surface curvature, an estimate of the porosity of the bonds and the bond size. The bond size increased in time for all samples, indicating an apparently monotonic sintering process. In contrast, other bond metrics revealed contrary evolutions between small and large spheres, indicating the growth of solid bonds in the sample with 1 mm particles and porous bonds for 2.1 mm particles. The sintering conditions in the 2.1 mm sample of the time series were further investigated using Finite Element Method (FEM) simulations of the temperature field in the sample. The combination of microstructural and thermal information illustrates that even small fluctuations in the temperature of the sample environment, which can hardly be avoided experimentally, induce significant temper-

ature gradients within the sample that are concentrated in the contact region between two particles. Besides the localization of the temperature gradient, the FEM simulations revealed a decrease in the local temperature gradient after a certain time. Temperature gradients govern vapor diffusion and are critical for understanding the sintering process of ice. As such, the FEM simulations provide valuable insight into the temperature distribution within the sample. The observed non-monotonic evolution of the simulated local temperature gradient in the bond supports the interpretation of the anomalous sintering as a self-inhibited growth process.

The chapter is organized as follows. The next section describes the sample preparation, sintering conditions, and the image analysis methods. In the subsequent sections, the results are presented and discussed in view of particle size dependence, retreating protrusions, and practical implications.

5.2 Methods

5.2.1 Sample preparation

The ice spheres were produced with the tumbling method presented in Chapter 3.2.1. By varying the tumbling time, we obtained particles at different sizes. The sizes were selected by sieving: either as a size range that is defined by the sieve mesh size of two consecutive sieves used in series, or only by one sieve, where we only took the particles that remained in the mesh but passed through the sieve when shaking it. The particles were sieved directly after tumbling before they could sinter to make sure they passed the sieves one by one. Using such a simple method of segregation, different size classes could be obtained as listed in Table 5.1. The smallest and the largest sizes were used in time-lapse experiments, which focus on the continuous *t*ime evolution. The respective experiments are referred to as time series (tS) in the following. The size classes in between the smallest and largest spheres are used in an experiment to continuously assess the *d*iameter dependence of the final sintering state, this experiment is referred to as size series (dS). In total, eight samples were investigated. A sample is specified by the particle size, e.g. tS2.1 and dS2.1 for both samples with spheres of 2.1 mm

diameter. Here, and in the calculations, we used the middle value of the size range as particle size d_p.

Tab. 5.1: Selected particle size ranges (mm) that are defined by the mesh size of the used sieves.

	tS1	dS1.2	dS1.4	dS1.7	dS2	dS2.1	dS2.3	tS2.1
dS		1 - 1.4	1.4	1.4 - 2	2	2 - 2.2	2.3	
tS	1							2 - 2.2

For the size series (dS), six samples were prepared with the particle sizes d_p listed in Table 5.1. The particles were filled into cylindrical μCT sample holders with a diameter of 10 mm to a height of approximately 10 mm. The sample holders were sealed with a lid to avoid evaporation. For isothermal sintering, all six samples were placed in a Styrofoam box, which was stored for ten days in a small climate chamber. The chamber was set to -10°C and remained closed for the ten days. After ten days, the six samples were consecutively taken out for scanning in the μCT.

For the time series (tS), two samples were prepared in the same way, with particles at the upper and lower end of the particle size range (2.1 and 1 mm). For both samples, the sintering process was captured by μCT time-lapse scans. The samples remained in the μCT scanner for ten days and were scanned initially (0), after 3, 5, 7, and 10 days. The temperature in the scanner was set to -10°C.

Temperature logging

For all samples, the temperature was logged every 10 min during the sintering process. We used iButtons from the company Dallas Semiconductor (now Maxim Integrated) with a resolution of 0.5°C. In order to derive a potential temperature gradient, the temperature was measured at the top and bottom of the sample. One iButton was fixed on top of each sample holder and a second was placed beside the sample, either in the μCT scanner for tS, or in the Styrofoam box for dS.

5.2.2 3D μCT image analysis

The samples were scanned in a Scanco Medical μCT 40 scanner. The scanning duration was 2.8 h and the voxel size was 6 μm. From the resulting grey scale images, a volume of interest of (1100×1100×550) voxels was then segmented, by fitting the sum of three Gaussian distributions to the grey scale histogram [35]. The obtained binary image of the two phases, ice and air, was used for the subsequent evaluation. For *d*S1.2, the section had to be reduced to (1100×1100×400) voxels, to eliminate a scanning error at the top of the sample.

Specific surface area and surface curvature

The specific surface area SSA, the ratio of ice surface area to ice mass, was used for the investigation of the sample surface and the growth of small structures. It was calculated using a triangulation-based method that is provided by the vendor software [42].

The local curvature H was evaluated on a triangulated mesh [59]. For computational reasons, the volume of interest had to be reduced to (550×550×550) voxels for this evaluation ((550×550×400) voxels for *d*S1.2).

The specific surface area and curvature are characteristics of the entire sample surface and will be used to characterize the anomalous features of the ice-air surface during sintering. To detect also anomalous, volumetric features (like porous bonds) a non-standard analysis of the bonds is required.

Bond porosity and bond size

The quantification of the bond properties relies on automated bond-specific image analysis that was performed on the 3D binary images using the programming language Python. The analysis of the bonds is based on the identification of particles and their neighbors, which is achieved by watershed segmentation, similar to the method described in Chapter 2.3.3 and 3.2.6. After the particles were identified and labeled, pairs of touching particles were extracted from the volume to examine their bond in a smaller subvolume.

The quantification of the bond porosity in a mechanical sense was impeded by the complex bond geometry of the randomly oriented spheres.

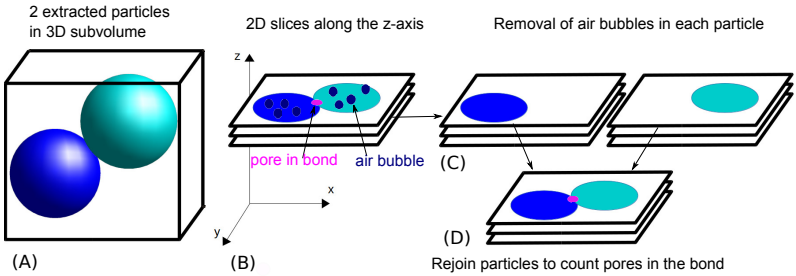

Fig. 5.1: Touching particles were extracted from the sample volume to examine the sintered bonds in a smaller subvolume (A). The porosity was quantified in 2D slices, in which air between protrusions appears as enclosed pores. By iterating through all slices along the three main axes (B, here z-axis), the air bubbles within the particle volume were removed from each particle (C), to only count the pores in the bond (D).

To obtain an estimate for the porosity in the bonds, two touching particles were analyzed by iterating through 2D slices along the main axes of the subvolume (sketched in Figure 5.1). This was required, since the bond porosity that formed during sintering, is not necessarily due to enclosed pores in the ice phase, but rather formed by several column-like structures that connect the two particles. In 2D, the air phase between two columns is separated from the main air phase around the particles and appears as enclosed pore - which makes it countable. To only investigate the pores in the bond, air bubbles in the ice volume of the particles should be excluded from the evaluation and had to be removed. This was done for each particle in a separate subvolume (Fig. 5.1(C)) by identifying the largest connected air region and assigning all other voxels to the ice phase. Afterwards, the two particles were rejoined and enclosed air pores remained only in the bond between the particles (Fig. 5.1(D)). A 2D slice of a subvolume containing two particles after elimination of the air bubbles is depicted in Figure 5.2. Then the closed pores in the ice volume of each 2D slice were counted as n_{pores}, as well as the number of slices n_{slices} in which the two 2D-particles were in contact, i.e. the slices that contain the actual bond. From this, we defined the bond porosity parameter χ by normalizing the number of pores in a bond by the bond

extension:

$$\chi = \frac{n_{\text{pores}}}{n_{\text{slices}}} \tag{5.3}$$

The identified pores are presented in different colors in the inset of Figure 5.2.

The entire evaluation was performed in all three main directions of the randomly oriented spheres, i.e. the volume was sliced along the x-, the y-, and the z-axis, to show the reliability of the results. The results of the three evaluations may deviate from each other for a single bond, but are highly correlated in the average over all bonds in the volume of interest. The presented results show the mean of all three evaluations and their standard deviation.

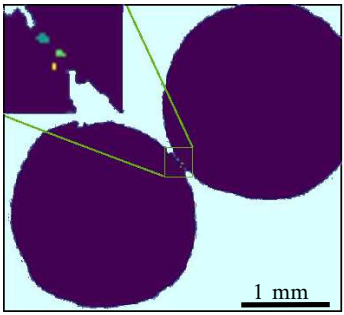

Fig. 5.2: Identification of pores in sintered contact between two particles that were extracted from the volume. The identified pores are presented in different colors and shown in the enlarged contact region in the upper left corner.

The estimate of the bond size r_{b} relies also on the watershed segmentation. The algorithm separates two identified particles by a one voxel thick area, the watershed, which we take as the bond between the particles. Due to the porosity of the bond, this contact area is not necessarily connected and may consist of several patches. By again separating two particles from the volume, all contact patches that belong to the bond between these two particles were identified. The total number of voxels within the contact area n_{vox}, was converted with the voxel size s_{vox} to a radius $r_{\text{b}} = (n_{\text{vox}}/\pi)^{1/2} \cdot s_{\text{vox}}$ of an area-equivalent circular contact area.

5.2.3 FEM simulations of the temperature field

In addition to the structural information from the binary images, we obtained insight into the thermal conditions from voxel-based FEM simulations of the temperature field in the digitized sample structures. Local temperature gradients play a key role in crystal growth during metamorphism (and sintering) in snow [59, 92, 113] and provide us information about the local growth conditions. Based on the assumptions that 1) the vapor density in the pore space is saturated for a given temperature [108] (equilibrium condition) and that 2) the ice-air interface evolves slow compared to vapor and heat diffusion [51, 68] (stationary diffusion approximation), it has been shown that the velocity of the ice-air interface during diffusion-limited crystal growth can be approximated as a function of only the local temperature gradient [59]. The leading order role of temperature gradients (in solid and vapor phases) has also been highlighted in an analysis of interface stability [113]. Accordingly, we used the temperature field within the sample to obtain insight into the evolution of the growth conditions and investigate the anticipated non-monotonic growth of the bonds and protrusions (Chapter 3, [1, 15]).

The FEM simulations were performed on all five time-lapse μCT images of the *t*S2.1 sample, similarly as described by Pinzer et al. [92]. All voxels (ice and air) were converted to eight-node brick finite elements, on which the steady-state temperature distribution equation was solved. The boundary condition (Dirichlet) was defined with fixed temperatures at the top and bottom nodes, according to the temperatures measured in the experiments with the iButtons at the sample top and bottom. The thermal conductivities of ice and air were assumed to be $\kappa_{\mathrm{ice}} = 2.34\,\mathrm{WK^{-1}m^{-1}}$ and $\kappa_{\mathrm{air}} = 0.024\,\mathrm{WK^{-1}m^{-1}}$. Heat transfer by advection was neglected.

From the resulting temperature field within the sample, the temperature gradients in all three main directions (x, y, z) were determined. Thus, the simulation results consist of 3D images of the temperature gradient in the three main directions and the respective heat flux q. The 3D images of the vertical temperature gradient (z-direction) were used for further evaluation. We determined the average $\langle \nabla T \rangle$ and the maximum ∇T_{max} of the temperature gradient in the entire sample and also in subvolumes of the bond regions, denoted as $\langle \nabla T^{\mathrm{b}} \rangle$ and $\nabla T^{\mathrm{b}}_{\mathrm{max}}$. The respective subvolumes for calculating these values in the bond regions

were identified in the watershed segmented images that were used for the evaluation of the bond properties. By evaluating the contours of adjacent particles using the `contours` function in the Python Skimage library, the contact between the particles and its extension in the x-, y-, and z-directions could be determined. This defines a volume around the bond, which was augmented by 10 voxels in each direction for the evaluation of the temperature gradient.

5.3 Results

A visual overview of all investigated samples is presented in Figure 5.3. It shows a 2D slice of each 3D μCT scan: the five images of the two time series (upper and middle row) show the same slice after 0, 3, 5, 7, and 10 days; the lower row shows one slice of each sample of the size series. The slices were taken from an x-z plane and are oriented such that the z-axis points upward, matching the vertical orientation of the samples in the scanner.

While the sphere surfaces in tS1 remain apparently smooth (top panel), the images of the tS2.1 sample (middle panel) reveal protrusions that can be seen on the top surface of the upper particle, as well as at the contact with the particle below where a porous bond is formed. These features, protrusions and porous bonds are most distinct in this sample. In the other samples, some protrusions (e.g. in dS2.3) and porous bonds (green circle in tS1) can be observed. In the following, we first present the results of the overall sample, then of the bond specific metrics.

5.3.1 Specific surface area

The measured specific surface area $\mathrm{SSA_{CT}}$ is evaluated by calculating the ratio with the $\mathrm{SSA_{ideal}} = 3/r_\mathrm{p}$ of a size-equivalent sphere, which was calculated with the known particle radius r_p ($= d_\mathrm{p}/2$) for all investigated samples. The ratio emphasizes the evolution of features on the particle surfaces. It is shown in Figure 5.4(A) for all samples against the sintering time and reveals contrarily evolving curves of the time series: from zero to ten days, the ratio increases for tS1 and decreases for tS2.1. For the dS samples, the ratio is shown at ten days, which decreases with increasing particle size d_p and lies consistently in between the two time series. This

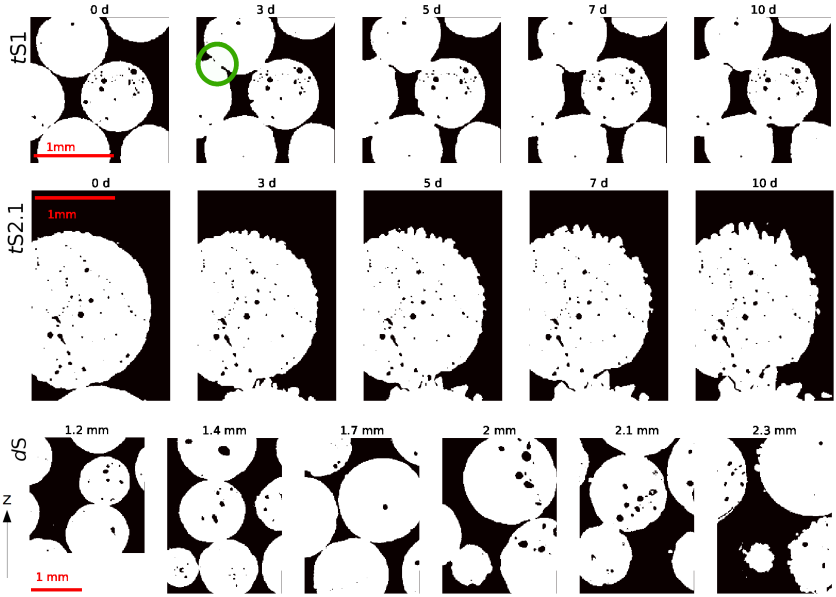

Fig. 5.3: Overview of all samples in 2D slices (x-z-plane, as oriented during sintering) of the 3D μCT images: the top row shows the time evolution of one slice of the tS1 sample, the middle row the one of the tS2.1 sample, and the bottom row shows the dS samples. White represents ice, black represents air.

size dependence becomes more clear in Figure 5.4(B), which shows the same data as a function of particle diameter d_p. The errorbars in the dS samples denote the size ranges of the sieves and show that the entire range from 1 to 2.3 mm is covered, with the largest uncertainty in the center.

A decreasing SSA-ratio, for tS2.1 in time and dS with size, implies an increase of the surface area. This increase can be caused by the growth of small structures on the particle surface, such as the protrusions observed on some particle surfaces, as well as the porous bonds. In the increasing SSA-ratio of tS1, we observe a decrease of the sample surface area in time. This indicates the formation of solid particle contacts, which reduces the surface area as it is known from normal sintering.

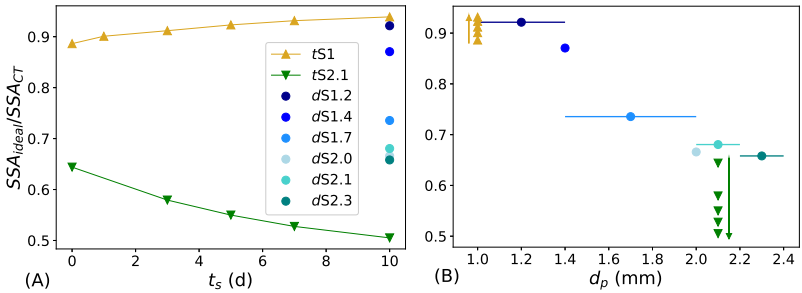

Fig. 5.4: Ratio of ideal and measured SSA as a function of time (A), and particle size (B). Errorbars in (B) denote the sieve sizes and the arrows besides the tS samples indicate the sintering time.

5.3.2 Surface curvature

Further evidence for the emergence of protrusions can be obtained from interfacial curvatures H. An illustrative example of the curvature evaluation is given in the 3D presentation of the surface in tS2.1 after seven days in Figure 5.5. It shows the neck region between two particles col-

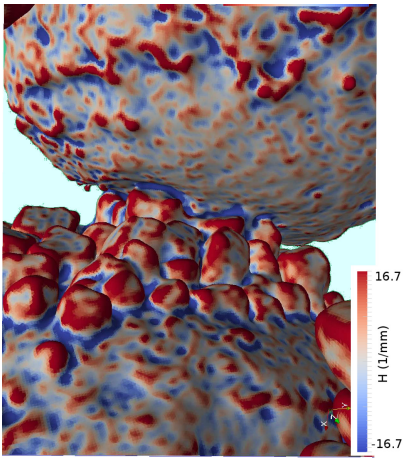

Fig. 5.5: Zoom into a bond region of the tS2.1 seven days image of the curvature analysis, with the curvature shown in color.

ored by the mean curvature. Dominant protrusions are on the surface of the lower particle, which seem to emerge from general (low amplitude) surface patterns which are visible on the remaining parts of the surface. This variety of features gives rise to a distribution of mean curvatures which is different from the one of a sphere. The distribution of the main surface curvature H is shown in Figure 5.6, in (A) for both time series and in (B) for all sizes after ten days. Negative values correspond to concave curvatures, and positive values correspond to convex curvatures. In all samples, the surface roughness gives rise to a maximum around $0\,\mathrm{mm}^{-1}$ and the characteristic curvature scale that corresponds to the particle size ($H = 1/r_\mathrm{p}$) cannot be derived. Aside from surface roughness, negative curvatures stem mainly from concave air bubbles within the ice and from the contact region between two particles. Positive curvatures are attributed to protrusions, besides surface roughness.

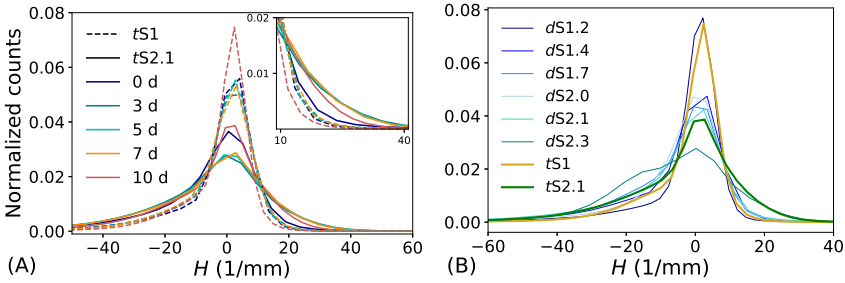

Fig. 5.6: Normalized curvature distribution H: for all investigated times of both time series (A); for all sizes after ten days sintering (B).

In time, the curvature of tS1 changes little. The most obvious changes are observed in the tS2.1 sample for small positive curvatures (inset in Fig. 5.6(A)). Initially, they are equally high in number as for tS1, but are distinctly higher at later times. Similarly increased positive curvatures were measured in the dS2.3 sample. This increase in the restricted range of small positive H between 15 and $40\,\mathrm{mm}^{-1}$ is attributed to the protrusions. These values correspond to the curvature of spheres with a radius of 0.025 to 0.07 mm, which gives us an estimate for the length scale of the protrusions that matches well the qualitative observations in the images.

5.3.3 Bond porosity and bond size

The bond porosity parameter χ and the bond size r_b were derived as bond-specific metrics for each bond. The average of χ for all bonds and the three directions is shown against sintering time for all samples in Figure 5.7(A). The errorbars (very narrow, only visible in $tS2.1$ at seven days) show the standard deviation of the three independent evaluations along the main directions. The value of χ decreases monotonically for the tS1 sample with an initial maximum of 0.38, which means that about 2/3 of the bonds sintered solidly, on average. In the tS2.1 sample, the average number of pores per bond increases from 1.3 to 2. The size series reveals increasing χ with increasing particle size. Almost no pores were measured in the smallest sample, while in the largest sample on average 3/4 of the bonds contain a pore.

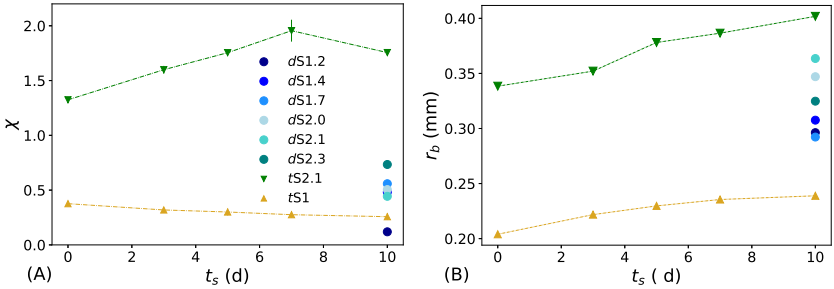

Fig. 5.7: Bond parameters: (A) mean of the bond porosity parameter χ and (B) mean of the bond size r_b of all samples against sintering time t_s.

The two time series tS show again opposite behavior for the evolution of χ. The constant decrease of χ in tS1 can be explained by filling of pores that might form initially due to surface roughness and non point-like contacts. An example of this is shown in the bond with a green circle in Figure 5.3. The development of χ in the tS2.1 sample is more interesting. An increase of χ corresponds to the formation of porous bonds, the growth of protrusions that form the contact. This is observed in tS2.1 up to seven days, as already indicated in previous metrics (SSA, H). Interestingly, χ decreases from seven to ten days. This could either

be explained by a closing of the pores, as described for tS1, or it could imply that the protrusions actually retreat, invert the formation of a contact, and then open the pores again.

The contact size is shown in Figure 5.7(B) against sintering time. The contact size is expressed as the radius r_b of an area-equivalent circular contact area. It increases for both time series and shows no clear tendency with particle size.

5.3.4 Temperature measurements

The logged temperatures are shown in Figure 5.8 for both 2.1 mm samples. For the dS sample that was stored in the Styrofoam box, top and bottom temperatures are rather constant with small fluctuations of $\pm 0.5\,°C$. The temperatures of the tS sample show generally higher de-

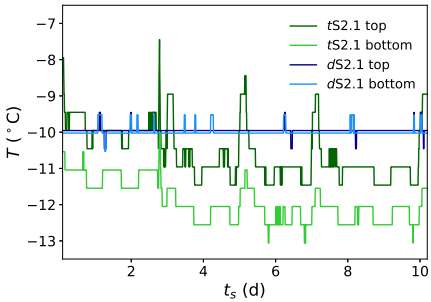

Fig. 5.8: Measured temperatures at the top and bottom of samples dS2.1 and tS2.1.

viations from an isothermal situation and are additionally affected by the μCT scans. Both temperatures rise several degree Celsius during scanning (0, 3, 5, 7, 10 d) and the difference between top and bottom temperature is larger than for the dS sample. Between the scans, the fluctuations are as well about $\pm 0.5\,°C$.

For both samples, the top temperature is higher than the bottom temperature. A larger temperature difference within the tS sample is obvious. From this differences, we calculated the temperature gradients within the samples and obtained an average of 0.015 K/m for the dS

samples and 0.87 K/m for the tS sample. The latter was used as input for the FEM simulations of the temperature field within the tS2.1 sample.

5.3.5 FEM simulations

The spatial pattern of the z-component of the temperature gradient around the spheres is visualized with colors in a 2D slice of the ten days image for sample tS2.1 in Figure 5.9(A). It shows largest temperature

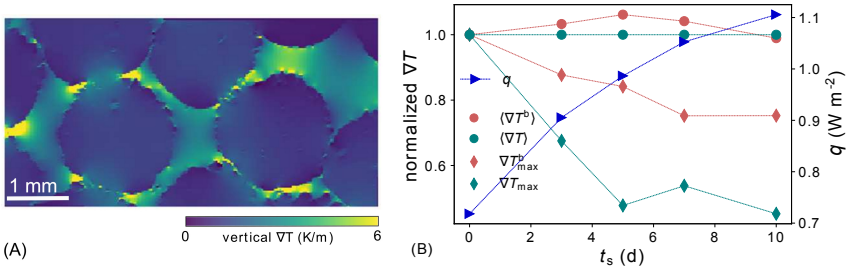

Fig. 5.9: Temperature gradient in tS2.1 from FEM simulations: 2D visualization in the ten days image (A); time evolution of average and maximal temperature gradient (normalized to initial values) in the entire sample ($\langle\nabla T\rangle$, $\nabla T_{\max}$), and in the bond-subvolumes ($\langle\nabla T^{\mathrm{b}}\rangle$, $\nabla T^{\mathrm{b}}_{\max}$), together with heat flux q in the sample (B).

gradients between the particles with local maxima at the protrusion tips. In the ice phase, the temperature gradient is minimal, indicating a rather homogeneous temperature distribution within each particle. The time evolution is shown in Figure 5.9(B) with the average $\langle\nabla T\rangle$ and maximum $\nabla T_{\max}$ of the vertical gradient for all five images of the tS2.1 sample (normalized by the initial value). The average is constant over time as it has to be due to the imposed simulation boundary conditions, but the maximum decreases towards ten days. The same evaluation of average and maximum values was performed on the subvolumes of all bonds and is shown in the same figure. The maximum $\nabla T^{\mathrm{b}}_{\max}$ decreases in time, similarly as $\nabla T_{\max}$ in the entire sample. In contrast, a non-monotonic behavior was found for the average temperature gradient around the bonds $\langle\nabla T^{\mathrm{b}}\rangle$, which initially increases and then decreases after five days. The temporary increase of $\langle\nabla T^{\mathrm{b}}\rangle$ in the bond volumes indicates a localization

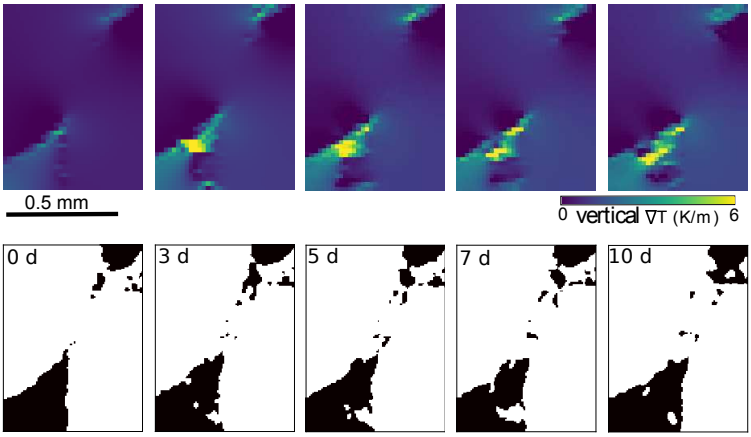

Fig. 5.10: Time evolution (from left to right) of one slice through a bond subvolume in tS2.1 sample. The lower row shows the subvolume around the bond from the binary μCT image (white = ice) and the upper row shows the corresponding slice from the FEM image. The temperature gradient is shown in color.

of the gradient in the contact regions. Its decrease after five days, as well as the decrease of the maximum, can be attributed to improved thermal contact during ongoing sintering, which is evidenced by the increasing heat flux q in the sample (Fig. 5.9(B)).

For one bond, the time evolution of the temperature gradient and the related structural changes are shown explicitly: 2D slices of the five FEM images are shown together with the equivalent 2D slices of the binary images in Figure 5.10, and the corresponding thermal ($\langle \nabla T^{\mathrm{b}} \rangle$ and $\nabla T^{\mathrm{b}}_{\mathrm{max}}$) and structural parameters (χ and r_{b}) from this 3D bond subvolume are plotted against the sintering time in Figure 5.11 (normalized to the initial values). This analysis reveals the concurrent evolution of the maximum temperature gradient, the extension of the protrusion at which it is located, and the bond porosity parameter χ. The 2D FEM images (Fig. 5.10 upper row) show the localization of the maximum temperature gradient at the protrusion tip that formed between zero and three days. The maximum temperature gradient in the entire subvolume $\nabla T^{\mathrm{b}}_{\mathrm{max}}$ slightly increases during the first three days and

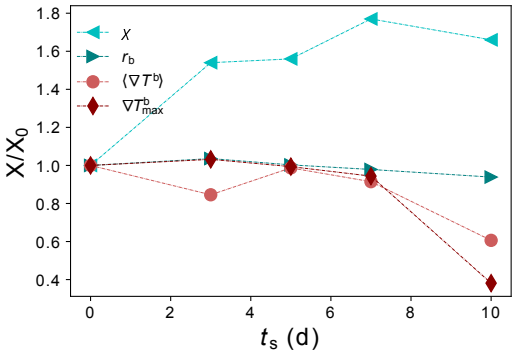

Fig. 5.11: Time evolution of the bond subvolume presented in Figure 5.10 measured by different quantities X normalized by their initial values X_0. The quantities (bond porosity parameter χ and bond size r_b, maximum temperature gradient $\nabla T^\mathrm{b}_\mathrm{max}$ and mean temperature gradient $\langle \nabla T^\mathrm{b} \rangle$) are listed in the legend.

decreases to the end of the experiment (Fig. 5.11). The respective protrusion grows in time but retreats again, without contacting the other particle (Fig. 5.10 lower row). Its maximum length seems to be reached after seven days. The evolution of χ in this bond, with its maximum at seven days, is in accordance with the average χ in this sample. The bond size reduces after three days again. In this bond, we observe the interrelation between growth and local temperature gradient. It seems in this particular case that the decrease in χ is caused by dissolving protrusions, as seen visually and in the measured r_b. In all investigated parameters, except for r_b, this bond is representative for the bonds in the tS2.1 sample.

5.4 Discussion

5.4.1 Sintering by unstable crystal growth

The two series of size and time dependent sintering experiments with ice spheres investigate sintering anomalies that have also been found in previous experiments [1, 15, 16]. The anomalies consist of the evolution

of protrusions on the particle surface and the formation of porous bonds between particles, instead of solidly sintered bonds. These features are visible in the 3D (and 2D) μCT images and were quantified via surface metrics (SSA, H) and bond metrics (χ, r_b) that characterize the evolution during sintering.

An estimate of the protrusion length scale λ (typical width of the protrusions) was obtained from the surface curvature distribution. If the range of curvatures that are affected by the protrusion evolution (H between 15 and 40 mm^{-1}, Fig. 5.6(A)) is converted to an equivalent radius R_H, we estimate $\lambda = 4R_H$. The values we obtain for λ are in the range of 0.1 to 0.27 mm. For these length scales, expressed as wavelengths of a sinusoidal perturbation on a growth interface, instability was predicted [16], using the dispersion relation of Mullins-Sekerka theory [85]. This theory of surface instability during diffusion limited crystal growth predicts the evolution of small surface perturbations (λ) for particles larger than a critical particle size D_c. The size of the particle dictates the local curvature. The local curvature, in turn, dictates the concentration fields above the surface, which are the driving forces for the local crystal growth. Crystal growth or sintering in snow is mediated by vapor diffusion, which is highly sensitive to temperature gradients and their impact on the vapor flux. Experimentally, a temperature gradient is hardly avoidable, as the top and bottom temperature measurements in the samples show (Fig. 5.8). Even if the average temperature gradient across the sample is very small (as for the *d*S2.1 sample), considerably higher gradients occur in the contact region due to the geometry (initial spheres in point contact) and large difference in thermal conductivities between air and ice [7]. The main heat flux occurs through the ice phase and the temperature in a particle is quasi homogeneous, except for the parts where it contacts other particles that have slightly different temperatures (cf. Figure 5.9 and [7]). These contact points are bottlenecks of the heat flow and therefore regions of high temperature gradients. They are the regions where sintering takes place. Therefore, although we aimed for isothermal sintering at -10°C, the unavoidable small experimental temperature fluctuations lead to significant temperature gradients at the particle contacts. The influence of the downward directed temperature gradient can be directly seen in the images in Figure 5.3: the gradient determines the growth direction, upwards, and amplifies the protrusion growth (cf. *t*S2.1 and *d*S2.3). This fact, however, provides interesting

insights into the relation of temperature gradients and critical particle size, since we measured different temperature gradients in the two sets of experiments, discussed in the next section.

5.4.2 Particle size dependence

The two samples of the time series bound the investigated particle size range and provide the upper and lower limits in most of the evaluated metrics. For both samples, the bond size r_b increases in time, as expected during sintering. In contrast, the other investigated parameters reveal a contrary evolution of the two samples. This is consistent with the growth of solid and porous bonds for tS1 and tS2.1, respectively. The specific surface area decreases for tS1 as the increasing contact area between touching particles vanishes from the surface, and the mean of the bond porosity parameter χ decreases due to the filling of initial pores (green circle in Figure 5.3). The mean curvature (not shown) of tS1 decreases in time as negative curvatures in the concave contact area gain weight in the H distribution (Fig. 5.6). In tS2.1, the opposite is observed. The SSA increases about 20% during the ten days, which can be ascribed to the growth of protrusions and porous bonds. Chen and Baker [16] measured the SSA explicitly in the bond region between two particles and observed a similar increase of the SSA with the evolution of a porous bond. We observed in χ an increasing bond porosity in time and the mean of χ is about ten times higher than in tS1 (Fig. 5.7(A)). The mean curvature increases in time due to the small positive curvatures of the convex protrusions. In the H distribution, the positive curvatures of the initial images were similar for both tS samples, but clearly increased in tS2.1 for all other times. This confirms the visual observation of the protrusion evolution in the 2D images (Fig. 5.3).

For the dS samples, the values of all parameters lie consistently in between those of both tS samples after ten days, mainly in order of particle size. For most parameters (r_b , SSA, χ), the values of the smallest sample are very close to those of tS1, whereas a larger difference was measured for the large particles. This can be explained by the higher temperature gradient in the tS sample (Fig. 5.8), which amplifies the growth of the protrusions. The results of both series show the roles temperature gradient and particle size play in the evolution of protrusions: a temperature gradient accelerates the process (comparison of tS and

*d*S samples) and dictates the growth direction (Fig. 5.3), but as seen in both series, despite similar temperature conditions only the large particles evolve protrusions while the small ones do not. This highlights the role of the particle size and indicates that the critical particle size D_c must lie between 1.2 and 2.1 mm for sphere packs which are subject to quasi-isothermal conditions with temperature fluctuations up to 1 K/m. An exact value is not resolved by the size series. The plot of SSA against particle size in Figure 5.4(B) shows the uncertainty of the particle sizes (sieve sizes) and the largest uncertainty occurring in the center of the investigated range. Nevertheless, the results allow for a significant reduction of the range of D_c from previously (0.7, 4) mm [15, 43] to (1.2, 2.1) mm.

It is important to point out here that D_c theoretically also depends on the concentration fields (eq. 5.2), in our case the excess vapor, which is influenced by the exact value of the temperature gradient. This cannot further be quantified by our experiments. Even in the FEM simulations, the limited accuracy of the applied voxel-based method raises a substantial error (up to a factor of 12.5 [59]) in the numerical solution at the interface, due to the two-phase nature of the system. However, we measured different temperature gradients in the two sets of experiments, but the results (SSA, H, χ, r_b) agree with the observations of solid bonds in small and porous for large particles. Thus, the range found for D_c does not seem to be heavily influenced by the precise value of the temperature gradient below 1 K/m. If we look at previous studies in the literature, we can assume: 1) similar conditions in the 4 mm spheres sintering experiments under "quasi-isothermal" conditions at -10°C , where porous bonds were observed [15]; 2) a saturated environment for the $d_p \leq 0.7$ mm spheres that sintered in a sealed container with ice-coated walls, where solid bonds developed [43]. Both are in accordance with our D_c-range. In contrast, the protrusions that were observed on non-spherical snow particles [1, 67] most likely grew on surfaces with higher curvatures compared to the curvature of 1 mm spheres (which would correspond to spheres with even smaller diameter than 1 mm). However, the particles were most likely exposed to higher supersaturation in both cases, which reduces the D_c according to equation 5.2. In one case [1] small, fractured ice particles with sharp edges that are prone to evaporation were mixed into the sample by sieving of the snow. In the other case [67], the samples were exposed to extreme temperature changes during

short transportation phases such that even frost was observed in the samples, which must have been induced by a high temperature gradient.

5.4.3 Retreating protrusions

The decrease in χ after seven days in the tS2.1 sample could be explained by retreating protrusions as it has been observed on similar time scales before [1, 15], or by filling of pores as in the tS1 sample. The answer to this question is not resolved by the structural metrics (χ, r_b), but the observed thermal conditions provide complementary information. In sintering experiments with 3 mm spheres and an externally applied sign-alternating temperature gradient, retreat was observed when the gradient was inverted [122], and explained by this obvious change in thermal conditions, which is crucial for protrusion growth. The existence of a temperature gradient in our experiments and its amplifying influence on protrusion growth has been discussed above. The time series of the 2.1 mm sample with the FEM simulations of the temperature field allow us to extend this discussion and point out the possibility of retreating protrusions with unidirectional temperature gradients.

The visualization of the FEM simulations reveals the localization of the temperature gradient in the bond region and especially at the protrusion tips (Fig. 5.9(A)), which drives the protrusion growth, as pointed out before. Its magnitude decreases over the course of the ten days, as we observed for ∇T_max in the entire sample, as well as for $\nabla T^\mathrm{b}_\mathrm{max}$ in the bond subvolumes (Fig. 5.9(B)). In a close-up analysis of one bond, we observed the interrelation of temperature gradient and protrusion growth (Fig. 5.10), where $\nabla T^\mathrm{b}_\mathrm{max}$ first increases as the protrusion forms, but decreases with time as the protrusion also decreases. With the decreasing temperature gradient, the driving force for protrusion growth weakens and may be overcome by the disposition of the system to reduce its surface area and energy by dissolving the protrusion (or filling the pore space). Although this visual observation is restricted to a 2D representation, the supporting metrics (χ, r_b, $\nabla T^\mathrm{b}_\mathrm{max}$, $\langle \nabla T^\mathrm{b} \rangle$) were taken in the 3D bond subvolume. The analysis of the entire sample and all other bond subvolumes, in terms of in χ, $\nabla T^\mathrm{b}_\mathrm{max}$, and $\langle \nabla T^\mathrm{b} \rangle$, is consistent with this particular observation.

The question remains why the magnitude of the temperature gradient decreases after five days. The key to the explanation lies in the dy-

namics of the system. While the bonds grow during sintering (porous or not porous), the thermal contact improves, as evidenced by the increasing heat flux q (Fig. 5.9(B)). From an analytical investigation of this problem [7], we estimate a q that is five times higher for a contact area of $r_\mathrm{b} = 0.4\,\mathrm{mm}$ (Fig. 5.7(B)) compared to a point contact (with $\kappa_\mathrm{ice} = 0.024\,\mathrm{WK^{-1}m^{-1}}$ and $\kappa_\mathrm{air} = 2.34\,\mathrm{WK^{-1}m^{-1}}$). The latter study concludes that the system's conductivity dominates over the material's conductivity and emphasizes the importance of the contact geometry. As a consequence of increased r_b and q, the local temperature gradient in the bond region decreases, which reduces the driving force for protrusion growth. Yet, a conclusion of whether the reduction in χ is induced by dissolving protrusions or filling of pores cannot be drawn. A combination of both is possible, as both would satisfy the system's desire to decrease surface area and energy.

Overall the results suggest the following mechanistic picture of anomalous sintering in ice spheres packs: Due to the initial singular geometry of large spheres with point contacts, small temperature gradients across the sample significantly increase the gradients in the vicinity of the bonds which are initially the bottlenecks of heat flow. The high values of local temperature gradients locally induce high supersaturations that fulfill the conditions for unstable growth. This situation is more favorable for large spheres. The onset of unstable protrusion growth leads to improved particle contacts which are porous in nature due to the underlying growth patterns. The growing particle contacts now improve the heat flow and thereby reduce the temperature gradients in the vicinity of the necks. This feedback acts as a self-inhibitor of the growth process as it reduces the driving force for unstable growth. The established, high curvature protrusions that form the neck relax thermodynamically and thereby retreat by minimizing their curvature and surface energy.

5.4.4 Implications

For various applications, it is of practical relevance to know that sintered contacts might differ from the theoretically predicted solid necks and monotonic evolution. Better knowledge about the size dependence, growth conditions, and retreat of bonds is important for their usage, design, and interpretation. The nature of the bonds governs the physical properties of the system: the mechanical (Chapter 3.3.4) and thermal

[7, 100] properties are affected by the bond porosity, and the optical properties are directly related to the SSA [123], which is considerably affected by the sintering anomalies. Theoretical investigations of surface instabilities are crucial to understand the growth mechanisms and estimate the occurrence, but exact predictions are hindered by unknown parameters [16, 84]. Previous experimental reports are very limited and leave a wide range for the critical particle size.

Our experiments provide help for selecting an appropriate particle size for future experiments, since ice spheres are a popular remedy for experimental investigations of simplified and well defined structures [15, 43, 62, 129]. The experiments presented here explain, with the measured bond porosity parameter, the weak sintering of the 2.1 mm ice bead samples in the compression experiments and the decreasing compressive strength between seven and ten days (Chapter 3.3.4). These ice bead samples sintered similarly to the *d*S samples at -10°C in a Styrofoam box. Since these compression experiments were designed for model calibration, and control of the bonds is crucial, we now know that particles with diameters less than 1.2 mm would be favorable. Yet, the compression experiments, together with the sintering experiments presented here, show the mechanical relevance of porous and even retreating bonds. This is significant for other systems of similarly sized particles, for example in the food industry while designing or preserving food [91, 109], or for the preparation of ski pistes or roads. The desired strength of a ski piste can often not be achieved in spring, when snow mainly consists of large melt form particles that do not sinter sufficiently over night [130]. Sintering of ice is also relevant for extra-terrestrial applications. The surface of planetary bodies often consists of sintered ice particles and the necessity of knowledge about sintering mechanisms and anomalies for investigating these remote objects is obvious. Sintered contacts and their physical properties are crucial for investigating planetary surfaces from telescopic or thermal observations, or for developing landing technologies of space craft [82, 100].

Our experiments further constrained the critical particle size for which surface instabilities may occur and provide evidence for a change in thermal conditions that allow for the retreat of bonds. The discussed image analysis methods are capable of resolving the protrusions as structures on the surfaces (SSA, H), and the porosity of the bonds (χ). These methods and metrics are applicable in further experiments for investiga-

tion of sintering anomalies. The discussion of protrusion retreat is based on FEM simulations of the temperature field within the tS2.1 sample. An automated method that explicitly resolves the protrusions would be necessary to further investigate this interesting process.

5.5 Conclusion and outlook

Two series of ice sphere sintering experiments rendered with μCT imaging, comprehensively illuminated sintering anomalies (protrusions and bond porosity) for different particle sizes and slightly different thermal conditions. A critical particle size D_c has to be exceeded for anomalies to occur, which can then be amplified by a temperature gradient. With the temperature gradient as the driving force, protrusion growth can reverse in time, as the gradient decreases due to improved thermal contact during the ongoing sintering. The occurrence of both size-dependent sintering anomalies and protrusion retreat is expected in a wide field of practical applications. Accordingly, the achieved reduction of the possible range of D_c from $(0.7,\ 4)\,\mathrm{mm}$ [15, 43] to $(1.2,\ 2.1)\,\mathrm{mm}$ matters. It is worthwhile to further investigate D_c and retreating protrusions to fully understand their occurrence (e.g. at different temperatures, or on longer time scales). This experimental approach augments the rather vague knowledge from theory. It is based on automated image analysis of the complex geometries in an arbitrary packing of spheres. The methods consistently resolve characteristics of anomalies in both time and size series and can be applied for future investigations. This work describes where and under which conditions sintering anomalies occur, which traces they leave, and which methods are capable of capturing them. Detailed, more quantitative investigations are necessary to obtain a quantitative understanding for the non-linear (self-inhibited) dynamics that lead to the retreat.

Microstructure-based validation of DEM models with ice sphere experiments

6

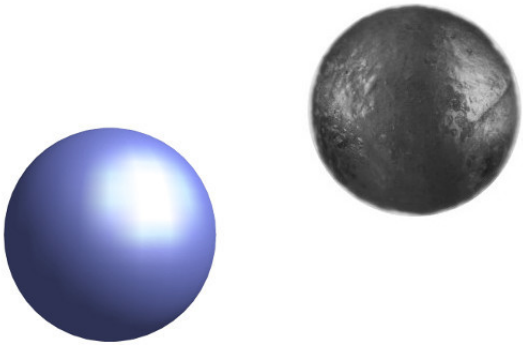

Abstract

Snow micro-mechanical models are difficult to validate with real experiments, due to the complex snow microstructure, which needs to be faithfully represented in models. In the Discrete Element Method (DEM), which is popular for numerical simulations of snow mechanics, the microstructure is commonly represented with discrete, spherical particles. Therefore, an unambiguous validation of a DEM model requires experiments using ice spheres. In this work we perform the first one-to-one comparison of model and experiment by simulating the ice sphere compression experiments for which the real microstructures are recreated in the model from 3D micro-computed tomography (μCT) images of the experimental samples. From the μCT images, position and size of the spheres were derived which define the microstructure geometry and a contact network. The DEM microstructures were created by connecting contacting particles with elastic-brittle beams to represent the sintered state. In this way, all microstructural parameters are predefined, except for the size of the beams, which could not be derived from the low resolution scans of the compression experiments. The experiments were simulated with two micromechanical DEM models, xDEM and Liggghts. For the Liggghts model, we used two parametrizations for the material properties of the bonds: in one parametrization (Liggghts-ice), bonds and particles have true ice properties (elastic modulus, Poisson's ratio, and strength), whereas in the other parametrization (Liggghts-snow), only the particles have ice properties while the bond properties were calibrated to match snow experiments. In the comparison with the experimental compression curves, only Liggghts-ice is able to reproduce the distribution of stress peaks during failure. The results underline the necessity of reproducing microstructural details for model validation. Well validated micromechanical snow models help to investigate processes that are experimentally difficult to access, such sintering during contact times of seconds, or the formation of stress-chains within the sample, and are necessary to upscale DEM models.

6.1 Introduction

For validating the formulation of micromechanical processes and calibrating snow models with experiments it is important to resolve the actual, physical particle contacts. Discerning the influence of micromechanical processes (e.g. friction or sintering) and non-spherical particle shapes on observable macroscopic behavior is difficult, but essential for validating contact formulation in models. Thus, the snow microstructure is the main input for micromechanical models, together with mechanical properties of ice, which are rather well understood (e.g. [20]). So far, validation of models of the discrete element method (DEM) has a rather qualitative character [36, 49, 77, 83, 118], since the snow microstructure representation in the model is generally simplified with the basic spherical DEM-particles. Finding a good microstructure representation is commonly a task on the modeling side [28, 33, 36, 75]. But neither of the present approaches render a microstructure-based comparison of simulations with real experiments possible.

In DEM models, both sintered and granular snow can be simulated, which makes DEM a powerful and popular tool to simulate snow mechanics with a wide range of loading rates. Another advantage of DEM is that the microstructure can either be roughly approximated, which allows for large-scale simulations [9, 27, 64, 83], or represented with high level of detail to investigate micromechanical processes [36, 77]. In the latter case, snow microstructure is represented with high degree of detail from 3D μCT images, by approximating irregular shaped snow grains with several overlapping DEM particles. Then the sample volume is restricted to several mm^3 for computational reasons but realistic snow microstructures could be investigated. In other micromechanical approaches [9, 49, 83, 118], the microstructure is simulated with assemblies of discrete spheres that are parametrized to represent the properties of a snow layer (e.g. density, elasticity) rather than resembling realistic snow structures. Both cases do not allow for experimental validation. Yet, it has been acknowledged that the key to successful modeling of snow mechanical problems lies in the snow microstructure [76, 83].

If microstructures are created with spherical particles, real grain shapes are oversimplified. Grain shapes dictate the geometry of the microstructure, as well as the actual inter-particle contacts. Consequently, grain

shapes affect the mechanics [36] and are important for realistic contact descriptions. Resolving the particle contacts is the basis for describing and investigating micromechanical processes in numerical models.

One microstructural process that is difficult to include in micromechanical DEM models is sintering. In snow, sintering connects contacting particles with solid, crystalline bonds which grow in time and are central to the determination of (macro-) mechanical properties, e.g. [6, 24, 38, 129]. In DEM models, a sintered microstructure is commonly constructed by bonding the discrete particles with beams [9, 49, 83, 118]. Then, the initial state, which changes with snow type and age of snow [41, 129] can be mimicked by the thickness of the bonds. But the estimation of an appropriate initial state is a difficult task for which model developers wish experimental background to obtain a less empirical approach [49, 64, 118]. Moreover, it was observed that ice particles sinter even within very short contact times [32, 114, 128], which affects structure and mechanics even during deformation [128]. The relevance of fast sintering during snow failure has recently been demonstrated in snow micromechanical DEM modeling [83]. In the latter study, the effect of fast sintering for contact times of seconds was simulated with a rather empirical description of this highly localized microstructural process. The mechanical relevance of short- and long-term sintering for snow micro- [83] and macromechanics [64, 112] has been acknowledged in recent works, which highlight the difficulty of including sintering in DEM models and the necessity of experimental information.

The spherical model snow introduced in this thesis is designed to tackle the problem of microstructure assimilation from the experimental side: with spherical ice beads, DE-like microstructures can be examined in real experiments. This approach provides microstructural as well as mechanical data for detailed model validation at the grain-scale. In unconfined compression experiments, ice bead samples were tested along with natural snow types, for comparison (Chapter 3). 3D μCT images were taken before compression for a faithful reconstruction of sphere positions and particle contacts. The bonds of contacting particles were varied by testing samples after different sintering times to investigate the influence of locally growing contacts on globally observed behavior.

In this chapter the potential and limitations of the ice beads as model snow are examined by investigating microstructure-based simulations of the unconfined compression experiments. Two micromechanical DEM

models are used, namely xDEM [48–50] and Liggghts [118], that were developed for simulating snow mechanics at the grain-level, i.e. snow grains are represented by spheres with material properties of ice. Both models use the μCT-derived microstructures as initial configurations of the particles. The sintered contacts are represented by elastic-brittle beams. The models differ in mechanical properties and geometry of the beams. The xDEM model uses the same ice properties for particles and bonds, but the bonding network was not derived from the μCT images. The Liggghts model [118] uses bonding network derived from the μCT images, but different material properties for particles and bonds. To overcome the limitations of both models, a second set of simulations with Liggghts has been conducted where the bond network is derived from μCT and the material properties of bonds and particles are the same. The two sets of Liggghts simulations differ only in the material properties of bonds, where the simulations with the parametrization of the previously published snow model [118] are referred to as Liggghts-snow, and the simulations with true ice properties for bonds and particles are referred to as Liggghts-ice. In both DEM models, the bond size (radius of cylindrical beam) is the only free parameter that must be used to fit the simulations to the experiments. Different bonding scenarios are simulated in sensitivity tests with Liggghts-ice and xDEM, by simulating different bond sizes in the predefined network (Liggghts-ice) and allowing rebonding of particles during the compression test, to mimic sintering during short contact times (xDEM). The Liggghts-ice model is able to reproduce the main features of the experimental compression curves. It yields realistic bond sizes by fitting the simulated curves to the experiment in terms of the main stress peak.

The chapter is structured as follows. The next section introduces the DEM models, with focus on Liggghts-ice and the new parametrization, and provides the experimental background with a summary of the compression experiments and a description of the microstructure generation via 3D μCT images. The results are presented and discussed with emphasis on the different realizations of the bond size parameter.

6.2 Methods

6.2.1 Simulation

The xDEM model was not available to conduct extensive simulations for the measurements presented in this thesis. Only two simulations with the xDEM model (conducted by Brice Kabore) are presented here. Instead, the open source DEM model Liggghts was used for a complementary DEM analysis of the ice bead compression tests. Liggghts has previously been used for developing a snow micromechanical model [118], which was the basis for the simulations presented here. However, the implementation of the bond model used in [118] has never explicitly been published and therefore lacks an independent validation.

In both DEM models discussed herein, an elastic-brittle material model is used for the implementation of the bonds that represent the long-term sintering in the initial state. The formulation of the bonds is based on the publication by Potyondy and Cundall [94].

Liggghts

The open source DEM model Liggghts [56] with bond-extension[1] was used for the development of a snow micromechanical model [118]. The model was parametrized for different snow types and validated with a variety of different laboratory experiments (confined and unconfined compression, shear, and angle of repose experiments). Snow grains are represented by elastic, spherical particles connected by elastic-brittle bonds. The bonds are cylindrical, elastic-brittle beams that are removed from the simulation when they break as the stress exceeds the strength. After fracture, the particle interaction is defined by the Hertzian contact model [40] and Coulomb friction. Energy dissipation during bond deformation (viscosity) is excluded and limits the model to high strain rate deformation.

To match the variety of experiments, it was necessary in [118] to use different parameters for bonds and particles. For the simulation of the ice bead experiments with true ice properties, the bond parametrization has been adapted accordingly. Thus, the Liggghts model was used with two

[1] retrieved from https://github.com/richti83/LIGGGHTS-WITH-BONDS; Version LIGGGHTS-PUBLIC-BONDS 3.3.0

different parametrizations for the bond material properties, referred to as Liggghts-snow if parametrized as in [118], or Liggghts-ice if parametrized with ice properties for particles and bonds.

The particles are described by the density ρ, elastic modulus E, Poisson's ratio ν, as well as coefficients of friction μ and restitution η. These parameters are identical in both parametrizations and are used as in [118] and presented in Table 6.1.

In Liggghts, the material parameters of the bonds are linked to the bond geometry. The bonds are assumed to be massless beams with material properties of ice. The beams have a cylindrical shape and connect the center points of the particles. They can transmit forces and torques, and break if the tensile strength σ_i or the shear strength τ_i is exceeded. The failure criterion [94] combining tensile and bending stresses is described by:

$$\frac{-F^\mathrm{n}}{A} + \frac{|M^\mathrm{s}|\, r_\mathrm{b}}{I} \geq \sigma_\mathrm{i}, \tag{6.1}$$

and for shear and torsion stresses by:

$$\frac{|F^\mathrm{s}|}{A} + \frac{|M^\mathrm{n}|\, r_\mathrm{b}}{J} \geq \tau_\mathrm{i}. \tag{6.2}$$

$A = \pi r_\mathrm{b}^2$, $I = \pi r_\mathrm{b}^4/4$, and $J = \pi r_\mathrm{b}^2/2$ are area, moment of inertia, and polar moment of inertia of the bond cross-section, defined by the bond radius r_b. F^n, F^s, M^n and M^s are the forces and moments in the normal and shear direction defined as:

$$F^\mathrm{n} = k^\mathrm{n} A U^\mathrm{n}, \qquad F^\mathrm{s} = -k^\mathrm{s} A U^\mathrm{s} \tag{6.3}$$

$$M^\mathrm{n} = -k^\mathrm{s} J \theta^\mathrm{n}, \qquad M^\mathrm{s} = k^\mathrm{n} A \theta^\mathrm{s}, \tag{6.4}$$

with stiffnesses k^n, k^s, displacements U^n, U^s, and rotations θ^n, and θ^s.

In Liggghts, the bonds are defined by the parameters k^n, k^s, σ_i, τ_i and the ratio between bond and particle radii, $r_\mathrm{b}/r_\mathrm{p}$. The latter is a pure microstructural parameter. The material strengths, σ_i and τ_i, were used as in the Liggghts-snow model [118] and their values are provided in Table 6.1. In order to use the same ice properties for the bonds and particles, the stiffnesses, k^n and k^s, have to be adapted to the respective microstructures. The bond stiffnesses and the bond moduli are

Tab. 6.1: Material parameters used in the Liggghts simulations.

	Liggghts-snow	Liggghts-ice
Density of particle	$917\,\mathrm{kg/m^3}$	"
Young's modulus of particle	9 GPa	"
Poisson's ratio of particle	0.3	"
Coefficient of friction	0.3	"
Coefficient of restitution	0.2	"
Young's modulus of bond	90 MPa	(9 ± 0.7) GPa
Poisson's ratio of bond	1	0.3
Tensile strength of bond	2 MPa	"
Shear strength of bond	2 MPa	"

connected through the particle radius:

$$k^{\mathrm{n}} = \frac{E}{2r_{\mathrm{p}}}, \quad \text{and} \quad k^{\mathrm{s}} = \nu k^{\mathrm{n}} \tag{6.5}$$

For the parametrization of Liggghts-ice, the stiffness k^{n} (with dimension $\mathrm{Pa\,m^{-1}}$) was calculated with $E = 9\,\mathrm{GPa}$ and the mean particle radius r_{p}, which was derived from the μCT images. Because the input parameter k^{n} is constant in the simulation, the particle polydispersity ($r_{\mathrm{p}} = (1.12 \pm 0.1)\,\mathrm{mm}$, Chapter 3.3.1) in fact translates via Equation 6.5 into a slightly varying bond modulus as listed in Table 6.1. The Table shows for Liggghts-ice only the parameters that differ from the parametrization in Liggghts-snow.

The microstructural parameters are deduced from the μCT images of the experimental samples and the spherical particle shape. The particles are defined by a position (x, y, z) and a radius r_{p}. Adjacency pairs describe particles in contact, where each contact is represented by a bond. Accordingly, the adjacencies define a beam network, where the only free parameter that remains is the bond size r_{b}, the radius of the cylindrical beam. This parameter strongly affects the global strength of the sample. The bond size was used to "fit" the simulations to the experiments: in several simulation runs it was optimized such that the main stress peak of the simulations matches the main stress peak of the experiments. After the bonds are defined as initial state, no new bonds are formed during the simulation.

The boundary conditions in the simulations were chosen to match the displacement controlled unconfined compression of the experiments (Chapter 3.2.4). The sample rested on a base and was vertically compressed with a constant speed of 10 mm/s. The resting base and the moving piston were represented as rigid objects with geometry specified using the STL file format. The time step was set to $10^{-7}\,\mathrm{s}^{-1}$ and the total force on the base, as well as the position of the compression tool, were saved every 10 000th time step, which corresponds to a sampling rate of 1 kHz (the experimental sampling rate was 10 kHz).

xDEM

A snow micromechanical model has been developed [50, 79] with the xDEM code and validated [49] by comparison with diverse snow mechanical experiments from literature. The model represents snow grains with spherical particles and mimics a sintered microstructure by bonding the particles with elastic-brittle beams. In addition to the long-term sintering, which is represented by the beams and defines the initial state, fast sintering was also implemented in the model and validated with experiments where sintering was observed on (sub-)second time scales [114, 128]. The implementation is based on the explanation of the experimental observations of fast sintering [114], where viscous deformation of contacting particles is assumed to cause an increasing contact area. The created contact area is then consolidated and can grow during further deformation of the particles. This rebonding effect can be switched on and off, and both cases will be shown for the compression tests.

For the simulation of the ice bead compression tests, the microstructures were created according to the μCT derived particle positions and sizes. In contrast to the Liggghts simulations, in xDEM the bonds were created between touching particles, only after the particles were allowed to settle. The simulations were carried out by Brice Kabore within the SnowDEM project. A full description of the compression test simulation and a parameter study can be found in [48].

6.2.2 Experiments

The experimental basis for the following simulations are the unconfined compression experiments of sintered ice bead samples, presented in

Chapter 3. The 3D μCT images and stress-strain curves from the experiments Chapter 3 provide the microstructural and mechanical data for the comparison with the models. Cylindrical samples with a diameter of 33.6 mm and a height of 14 mm were sintered for 3, 5, and 10 days and were then compressed at 10 mm/s. Two samples per sintering time were captured by μCT scanning just before compression. Figure 6.1 shows an ice bead sample from a photography of the experiment, a rendered μCT image, and the rendered initial state of the simulation.

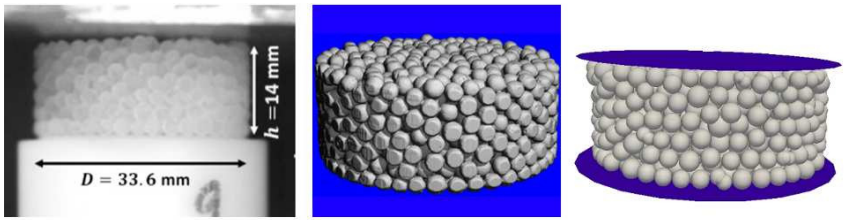

Fig. 6.1: Sintered ice bead sample before compression (A), imaged via μCT (B), and reconstructed with spherical DEM particles (C).

The available ice bead experiments can be classified by sintering times (3, 5, and 10 days) or sample densities ("poured" and "tapped" samples). In this Chapter, we only consider the "poured" samples and present the simulations of six samples (two per sintering time) with the Liggghts model. In the xDEM model, the focus was on one sintering time (5 days), thus, only two xDEM samples are shown here. The chosen samples are highlighted in Figure 6.2, which shows an overview of the compression experiments (main peak of the experiments, analogously to Fig. 3.9 in Chapter 3.3.4). Note that the experimental data set (Fig. 6.2) contains additional snow types compared to Chapter 3 which allows to discuss the simulations in the context of all available compression experiments. Compression experiments were actually performed with all three nature identical snow types that have been detailed in the angle of repose experiments in Chapter 4.2.1: rounded grain (RG), faceted grains (FC), and smaller faceted grains (FCS).

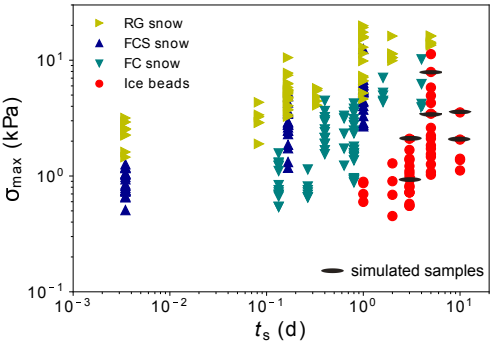

Fig. 6.2: Overview of all compression experiments with ice beads and nature identical snow types at different sintering times. The compressive strength $\sigma_{\max}$ was derived as described in Chapter 3.3.4 from the first main peak of all stress-strain curves.

Microstructure reconstruction

The high sphericity of the ice beads shown in Chapter 3.3.1 is key for an efficient reconstruction of the sample with spherical DEM particles. The microstructure of the ice bead samples is defined by the position and size of each particle. These parameters were assessed in 3D image analysis, using the programming language Python. In the watershed segmented images (Chapter 3.2.6), the particles were identified and could be individually analyzed. For the position (x, y, z), we derived the center of mass using the `regionprops` function in the `Skimage` library. For the particle size r_{p}, the radius of a volume equivalent sphere, $r_{\mathrm{p}} = (3/4\pi n_{\mathrm{vox}})^{1/3} s_{\mathrm{voxel}}$, was determined from the number of voxels n_{vox} that make up the particle and the voxel size s_{voxel}. Accordingly, a particle is described by the tuple $((x, y, z), r_{\mathrm{p}})$.

In the next step, the distances between particles were analyzed, to a) detect overlap and b) determine adjacency pairs. Overlap between DEM particles could occur, because the experimental particles were not perfect spheres. This overlap had to be removed, because it would lead to numerical instabilities in the Liggghts model. If overlap occurred between two particles, the radii of both were reduced by half of the overlap length, such that they were only touching without overlap in the final state. The bond size r_{b} could not be derived from the μCT

images, because the resolution was too low. The bond size was therefore used here as a free parameter that was later compared to the radius of available high resolution scans from Chapter 5.

The tuples of position and size ((x, y, z), r_p) were used to define the particles in all models. The bonds were created according to the adjacencies in Liggghts. In xDEM they were created at true particle contacts, after the particles were allowed to settle.

6.3 Results

6.3.1 Ice bead compression simulated by DEM

The simulations are compared to the unconfined compression experiment via stress-strain curves. In the following we focus on the results of one sample. An overview of the results of all six samples is provided in the Appendix.

For one ice bead sample after five days sintering, the four stress-strain curves are shown in Figure 6.3: (A) the entire compression test, (B) a zoomed in view of the first 10% strain. The experimental curve exhibits very pronounced stress peaks, in between the stress almost drops to zero. The maximum is reached within 5% strain. After 10% strain, the stress peaks decrease in number and height. It is shown and discussed in Chapter 3.3.4 that the high sampling rate fully resolves the peaks, and that the peaks stem from clusters of particles that break out of the structure.

In all simulations, the main fracture (stress-maximum as defined in Chapter 3.3.4) occurs within 10% strain as well. However, only the Liggghts-ice simulation visually reproduces similarly strong stress-drops, whereas the curves of the other two models form the envelop of the experimental curve. The xDEM model exhibits very pronounced peaks for higher strains that exceed by far (up to 4.5 kPa) the experimental main peak, the highest peak within first 10% of strain. The curves of both Liggghts simulations contain significantly more noise than the xDEM simulation, which might be due to the higher sampling rate and the absence of damping through a bond viscosity.

These visual observations can be made quantitative by analyzing the stress-distributions as shown in Figure 6.4. The left figure shows the

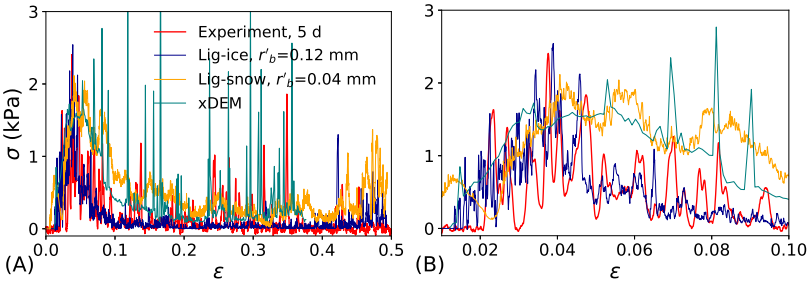

Fig. 6.3: Simulated and experimental stress-strain curves of unconfined compression tests of one ice bead sample after five days sintering. All three simulations were fitted using the bond size to the first main peak of the experiment. (A) shows the entire deformation and (B) a zoomed in view of the initial 10% strain. (In (A), the peaks of the xDEM curve lie outside the shown range but are presented in Figure 6.4).

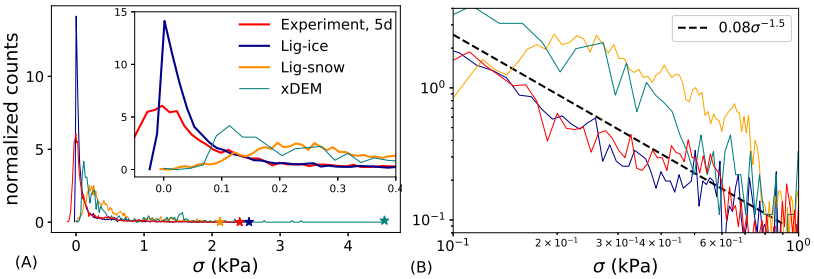

Fig. 6.4: Stress distributions of the experimental and the three simulated curves, (A) shows the entire range where the stars denote the stress maxima, with a zoom into the low stress range in the inset, and (B) shows the same data in log-log scale. The distributions (normalized counts) are normalized that the area is unity.

entire stress range, where a star marks the maxima, and a zoomed in view of the low stress range in the inset. The right figure shows the same curves on a log-log scale. Apart from the differences of the stress distributions for small stresses (dominated by noise in the experiment), the tail of the distribution for large stresses of the Liggghts-ice simulation

is very similar to the experimental distribution and approximately follows a power law $\sim \sigma^b$, with $b = -1.5$ (dashed line in Fig. 6.4(B)). This indicates that Liggghts-ice seems to reproduce the essential failure characteristic during the compression tests. In contrast, the distributions of xDEM and Liggghts-snow simulations are shifted to higher stress values.

The analysis suggests that only Liggghts-ice, i.e. the combination of the true bond network and the true ice parameters, is able to reproduce the key features of the experiments. This is representative for all six simulated ice bead samples.

Bond sizes

The main peak of the simulated curves (highest peak within the first 10% of strain) was fitted with the bond size parameter r_b to match the peak of the experimental curve. In both Liggghts simulations, all bonds in the sample have the same radius, r'_b=0.12 mm in Liggghts-ice and r'_b=0.04 mm in Liggghts-snow. This factor of three is due to the differences in material properties of the bonds.

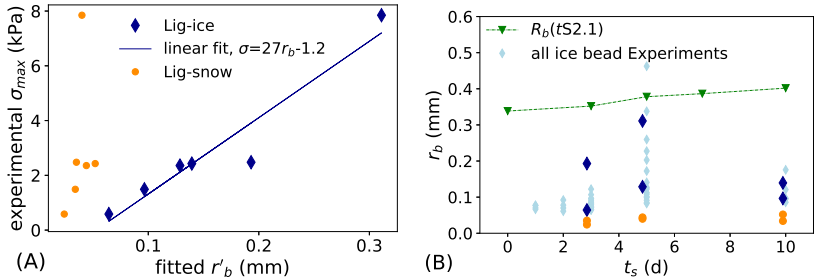

Fig. 6.5: Fitted bond radii r'_b from both versions of Liggghts simulations: with experimental strength (first main peak) in (A); against the sintering time together with the measured bond sizes from Chapter 5.3.3 in (B). With equation 6.6 (fit in A), the strengths of all conducted ice bead experiments presented in Figure 6.2 are translated to a bond radius and are shown in (B) as well.

For both versions of Liggghts simulations, the obtained values for r'_b of the six samples are presented in Figure 6.5. The plot in (A) shows the relation with the experimental peak σ_max and illustrates the different

ranges in bond size of the two sets of simulations. For Liggghts-ice, we obtain a linear relation between r'_b and σ_max. A linear fit yields

$$\sigma_\mathrm{max} = (27.23 \cdot r_\mathrm{b} - 1.26)\,\mathrm{kPa} \tag{6.6}$$

with r'_b in mm and a correlation coefficient $r^2 = 0.91$. For Liggghts-snow, the relation of σ_max and r'_b is not as clear.

In Figure 6.5(B), the fitted value of r_b is shown against the sintering time t_s of the respective samples. We can now compare these values to the results of the estimated bond sizes R_b from the tS2.1 sample presented in Chapter 5.3.3, which was scanned with a three times higher resolution. The tS2.1 sample has similarly sized particles (2.1 mm diameter) and was also sintered at -10°C. The fitted bond sizes r'_b of the Liggghts-ice model are of the same order of magnitude, but smaller than R_b. We do not have enough points to derive a relation between r'_b with t_s. A monotonic increase of r'_b in time, similarly as for R_b, cannot be observed. With the relation between r'_b and σ_max, the obtained r'_b mirror the large scatter of σ_max in all experiments and the decrease of σ_max between seven and ten days (c.f. Figure 6.2).

6.3.2 Sensitivity tests

The comparison of the three simulations in the previous section revealed differences in reproducing the ice bead compression experiments. The differences can be attributed to the way the bonds are simulated, since all models have the same initial particle configurations. This underlines the crucial role of the bonds. Therefore, the sensitivity on bond parameters should be further investigated.

In Liggghts-ice, the bond sizes in the predefined bond network were varied to obtain a more realistic initial sintering state. Mono-sized bonds were considered unrealistic for a naturally sintered ice bead sample, where local differences in sintering conditions exist (c.f. Chapter 5). Moreover, the sensitivity to variation in the material properties of the bonds was tested.

In xDEM, the possibility of switching on the rebonding was used to assess the influence of fast sintering during the compression test, which affects the number of bonds.

Liggghts-ice: Inhomogeneity in bond network

In the following we focus on the pronounced peaks in the experiments, which were attributed to the fracture of clustered particles (Chapter 3.3.4). To create inhomogeneity in the sample that could favor clustered fracture, the bond sizes were varied, while the geometry of the bond network remained the same. The uniform bond sizes were re-

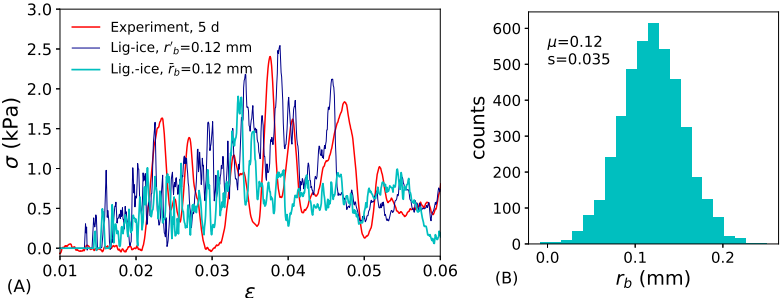

Fig. 6.6: Stress-strain curve from simulation with random bond sizes ($\bar{r}_\mathrm{b}$) compared to the simulation with mono-sized bonds (r'_b) and the experiment (A). To create inhomogeneity within the sample, values for r_b were taken from a Gaussian distribution (with $r'_\mathrm{b} = 0.12\,\mathrm{mm}$ as mean and $s = 0.035\,\mathrm{mm}$ as variance shown in (B)) and were distributed randomly in the beam network.

placed with a Gaussian distributed bond size with the same mean value (Figure 6.6(B)). The resulting stress strain curve is presented in Figure 6.6(A), together with the simulation of mono-sized bonds (presented above, Fig. 6.3). Aside from slight variation in the height of the peaks and stress-drops, the main fracture pattern of the curves do not differ significantly. This comparison however shows that bond size disorder has an influence on the peak stress which is reduced here compared to the mono-sized bonds.

Liggghts-ice: Sensitivity of bond strengths

The robustness of the Liggghts-ice parametrization was further examined by varying consecutively the bond strengths (σ_i, τ_i) for $\pm 10\%$, while all

other parameters were kept constant (as listed in Table 6.1). The resulting stress-strain curves in Figure 6.7(A) show a generally similar pattern and considerably lower variations when compared to the inter-model differences found in Figure 6.3(B). The stress-distributions of these curves are plotted in Figure 6.7(B), together with the data of the experiment and the Liggghts-ice simulation with mono-sized bonds (on the same scale as in Figure 6.4(B)). The simulations again show a consistent behavior of the stress distributions (in contrast to the inter-model differences from Fig. 6.4). This underlines the robustness of the Liggghts-ice parametrization, as well as the significance of the bond size parameter.

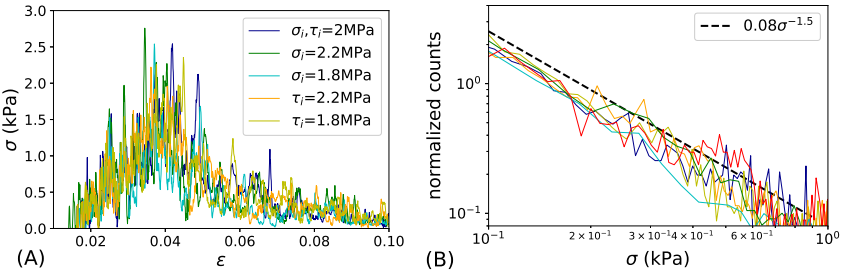

Fig. 6.7: Sensitivity study on material parameters (σ_i, τ_i $\pm 10\%$) of the bonds in Liggghts-ice: (A) shows stress-strain curves and (B) shows the stress distributions (same scale as in Fig. 6.4(B)), together with the experimental curve and the Liggghts-ice simulation with mono-sized bonds (here denoted as σ_i, $\tau_\mathrm{i} = 2\,\mathrm{MPa}$).

xDEM: Rebonding as fast sintering

The xDEM simulations with and without rebonding are presented in Figure 6.8. Qualitatively, the curves are similar and both envelop the experimental curve. The simulation with rebonding leads to some additional stress peaks.

6.3.3 Compression of natural snow

To discuss the results later in the context of snow compression in general, examples of representative stress-strain curves of different snow types are

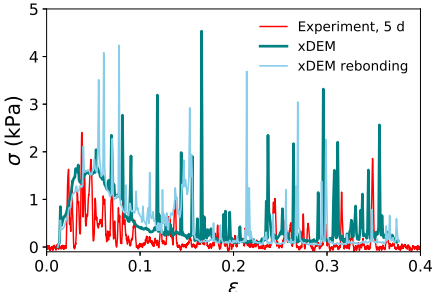

Fig. 6.8: xDEM simulations with and without rebonding.

shown together with the ice bead experiment that was analyzed by the simulations in Figure 6.9.

Not all of the snow types were investigated after five days sintering, which is why different sintering times are shown. However, these curves are typical for the respective snow type, sintering mainly changes the magnitude of stress. Despite partially shorter sintering times, all snow samples were significantly stronger than the ice bead sample (also c.f. Figure 6.2). None of the snow samples exhibited stress-drops as strong as the ice bead samples. The signature of clustered fracture is less dominant within the overall higher stress-signal.

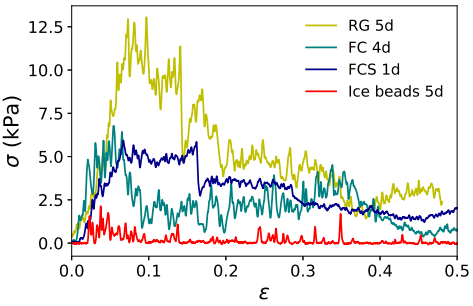

Fig. 6.9: Experimental stress-strain curves of each nature identical snow type and the previously shown ice bead sample.

Tab. 6.2: Mean sample densities.

Snow type	Density [kg/m^3]
Ice beads	546
Rounded grains RG	409
Faceted small FCS	402
Faceted grains FC	355

The mean densities of the snow types are given in Table 6.2. The table and the compression curves reveal the well established relation between strength and density for natural snow: the higher the density, the higher the compressive stress (c.f. Fig. 6.9 and 6.2). However, the small facets have similar densities to the rounded grain snow, but exhibit stresses in the range between rounded and faceted grains (better seen in Figure 6.2, for equal sintering times). This fact has to be attributed to the microstructure. For the ice beads, this relation does not hold; the ice bead samples have the highest densities, but the lowest stresses.

6.4 Discussion

The ice bead compression experiments presented in Chapter 3 were simulated with two micromechanical DEM snow models. Via the 3D μCT images of the experimental samples, all microstructural parameters were constrained except for the bond sizes that are used to account for the sintering state. The bond size could not be derived from the μCT images of the compression experiments because the resolution was too low. The detailed sphere sintering experiments presented in Chapter 5, which were conducted under similar conditions (particle size, temperature), were instead used to provide missing information about the quality of the bonds and their size. Based on these two sets of experiments, compression tests and sintering studies, we can now discuss the first microstructure-based comparison of DEM simulations with snow micromechanical experiments. The compression experiments with natural snow types investigated together with the ice bead experiments provide the experimental foundation for this analysis.

6.4.1 Microstructure-based DEM simulations

With a predefined beam network and true ice properties for particles and bonds, the Liggghts-ice model must be regarded as the most faithful representation of the experimental conditions. In the comparison of experimental and simulated compression curves, the Liggghts-ice model is the only model that reproduces the characteristic fracture behavior of the ice bead samples, namely, the pronounced peaks and stress-drops that dominate the first 10% of strain (Fig. 6.3). This behavior is attributed to the fracture of clustered particles, which could clearly be observed in the ice bead experiments (c.f. high-speed imaging movie provided in the supplementary material of [129]). The signature of such clustered fracture can also be seen in the compression curves of the natural snow types (Fig. 6.9), but less dominant within the overall stronger signal. These peaks are most prominent in the ice bead samples, which have the smallest sample volume relative to their representative elementary volume (Chapter 3.4.2). Accordingly, breaking of a single cluster strongly affects the stress signal. The clustered fracture may be caused by fracture of a stress-chain [60], of which only few are formed in the comparable small volume of the ice bead samples. The stress-chains are formed by the particle configurations and stress is transmitted via the bonds in the simulations. Liggghts-ice seems to be capable of reproducing this behavior. The other two simulations, with xDEM and Liggghts-snow, fail to simulate the clustered fracture. Instead, they have the tendency to consistently exceed the measured stress without forming pronounced peaks. This difference in DEM model behavior is consistently found for all samples (see Appendix 6.6.1). In summary, the Liggghts-ice model reproduces the experimental curves best.

These observed differences in the simulations were further quantified by analyzing the stress distributions (Fig. 6.4). The Liggghts-ice simulation yields a very similar stress distribution to the experiment, except for the low stresses (close to zero) that are influenced by noise and the details of the contact model. The simulations with xDEM and Liggghts-snow miss the low stresses. It remains to be discussed if the observed -1.5 power-law decay of the stress distribution (indicated in black dashed line in Fig. 6.4(B)) is coincidence or can be related to similar power-laws for energy distributions of failure in granular materials (e.g. [18]), as it has also been measured for snow failure [12].

The beam network seems to constitute a crucial aspect of the microstructure in the ice bead samples. This can be concluded from the fact that all three simulations used the same sphere configurations and differed only in the way the beams were simulated. Still, two simulations failed in reproducing the experimental observations. The two sets of Liggghts simulations were carried out on the exact same microstructures, they differed only in the material parameters (E and ν) of the bonds and consequently in the bond sizes r_b. The bonds in xDEM are based on the same description [94] as the bonds in Liggghts but are additionally equipped with viscous damping. Moreover, the geometry of the bond network differs in xDEM and Liggghts, since the xDEM bonds were created only after the particles settled, in contrast to the μCT-derived bond network used in Liggghts. This settling process may be comparable to the tapping that was used to densify some of the ice bead samples presented in Chapter 3, which resulted in higher contact densities (Fig. 3.6) and compressive strengths (Fig. 3.9).

Introducing inhomogeneity in the beam network of Liggghts-ice (analogously to the observed dispersity in the measured bond sizes, Fig. 6.10), affected the stress-strain curves and led to steeper stress-drops compared to the simulation with uniform bond sizes (Fig. 6.6). Here, only the bonds sizes in the predefined bond network were changed, even within a realistic range of bond sizes and with the same average bond size. In contrast, the xDEM simulation with rebonding that affects the number of bonds during the compression test, did not differ significantly from the simulation without rebonding (Fig. 6.8).

6.4.2 Bond sizes

With the Liggghts models, two samples per sintering time (3, 5, and 10 days) were simulated by fitting the main peak to the experimental peak via the bond size parameter r_b . The values of r'_b obtained with the Liggghts-snow model are significantly lower for all samples than the ones of the Liggghts-ice model. This is due to the different bond properties (E and ν, Tab. 6.1). An estimate of the real bond sizes can be obtained from the results for R_b from Chapter 5.3.3, which provide a valuable source of information. The results show that the bond sizes in Liggghts-ice are of the same order of magnitude as R_b. The slightly lower values of r'_b might be due to the mechanical relevance of the porosity in the bonds.

This indicates that r'_{b} mirrors the sintering state of the experimental sample fairly well and leads to realistic values when the bond size is used to match peak stress of experiment and simulation. With this, another microstructural feature of the experiments is approximated very well and the only free microstructural parameter is consistent with the values obtained from higher resolution measurements. The significance of these values is underlined by the shown robustness of the Liggghts-ice parametrization (Fig. 6.7).

6.4.3 Suggestions for future research

The presented simulations illustrate the central role that r_{b} plays in snow mechanical modeling and emphasize that a very high level of microstructural detail is necessary for model validation. The fracture characteristics of the ice bead samples are affected by changing only the bond sizes, even within a range of realistic values. In the presented simulations and method for microstructure generation, microstructural and mechanical uncertainties of bond properties remain, due to the randomness in the bond size distributions (in all presented simulations) and the presumed porosity in the bonds. Reducing these uncertainties seems feasible and worthwhile. Using smaller ice beads with $r_{\mathrm{p}} < 0.6\,\mathrm{mm}$ in the experiments could solve both problems: with smaller particles, the issue of bond porosity would be eliminated, as we know now from Chapter 5.4.2, and the sample volume could be reduced while still fulfilling requirements of an representative elementary volume. A smaller sample volume would allow for μCT scans with higher resolution, such that the bond sizes in the actual sample could be resolved and transfered to the simulations.

By eliminating the uncertainties in the bond parameter on the experimental side, DEM models could be validated towards a physical description of snow micromechanics. This is beneficial for a) using reliable micromechanical models for general micromechanical investigations (similar to well validated FEM models [29, 38]); b) finding correct descriptions of micromechanical processes, which can then be adapted for simulations on larger scales (e.g. sintering [64, 83]); c) gaining profound knowledge about microstructural and mechanical relations for simulating real snow with simplified microstructures.

6.4.4 Towards simulating snow

The compression experiments of the natural snow types (Fig. 6.2 and 6.9) and the sample densities (Table 6.2) confirm the common believe that the strength increases with density (e.g. [78]). The ice bead samples are not in line: they are denser and weaker than the natural snow. In the ice bead samples, the bonds are a major component of the microstructure. As shown in the previous sections, they are crucially important for simulating the ice bead behavior. In the ice bead samples, large parts of the particles contribute to the sample density but the deformation and failure is essentially restricted to the bonds. While the notion of "particles and bonds" is unambiguous for ice beads, this picture cannot be directly applied to real snow. However, the comparison of RG and FCS shows that there must be another parameter beyond density which makes the difference: RG and FCS exhibit significant differences in σ with quasi the same sample densities. This difference has its origin in the microstructure. In the ice bead samples, the difference in σ could successfully and plausibly be simulated by changing r_b, while density and contact density were constrained by μCT images. A similar approach for the snow samples seems not as straightforward, as we know that contact density plays a crucial role as well, which is expected to differ for these snow types [6, 24, 28, 121].

Understanding the main microstructural parameters (density, number of contacts, and size of contacts) as indicators in snow micromechanics is crucial for simulating natural snow realistically with simplified, well parametrized microstructures. Ice bead experiments can be used for this intermediate step. In measuring the real bond sizes as suggested above, we could achieve control of the main microstructural parameters. Variation in these parameters can be obtained by tapping of the samples, which changes density and number of contacts (Chapter 3.3.1, [63]), and different sintering times, which changes contact sizes. In this way, a well controlled and easily measurable system can be generated to further investigate the main microstructural parameters and their role in snow mechanics.

6.5 Conclusion

The main characteristics of the micromechanical experiments can be reproduced in DEM with true microstructures and mechanical properties of ice. By only fitting the main peaks of experiment and simulation with the bond size yielded similar stress-distributions of the compression signals. The bonds that are used to represent the effect of sintering are an important part of the microstructure. The bond size was found to play a crucial role in the simulations. Changing the bond size within a predefined bond network affected the compression behavior, even if the bond sizes were chosen within a realistic range. This underlines the necessity of detailed microstructural information for model validation and a reliable description of micromechanical processes. The remaining (structural and mechanical) uncertainties in the bonds can further be eliminated on the experimental side. This seems worthwhile towards comprehensive understanding of microstructural parameters for investigating micromechanical processes and to simulate natural snow with well parametrized, simplified microstructures.

Ice beads can serve as model snow for snow model validation. Investigating controllable inter-particle contacts helps to understand fundamental micromechanical processes, which are difficult to examine in real experiments, but are crucial for understanding and simulating snow mechanics.

6.6 Appendix

6.6.1 Compression results of all six samples

Two ice bead samples per sintering time are available with 3D μCT scan. All six samples were simulated with the Liggghts models (with both parametrizations). In xDEM only the two samples after five days sintering were simulated. The results of one sample after five days sintering are detailed in the results section. The results of all samples are shown here in similar presentations: stress-strain curves and stress distributions of experiments and simulations. The Liggghts-snow simulations are only shown in the stress distributions, for clarity (they are qualitatively similar for all samples, enveloping the experimental curves). The curves of all samples differ in shape and stress maxima. This variation is already indicated in the overview plot (Fig. 6.2) of all experiments, which exhibits large scatter in compressive strength at all sintering times.

Three day sintering samples

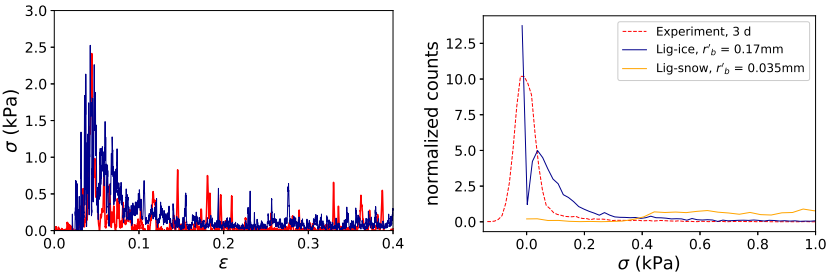

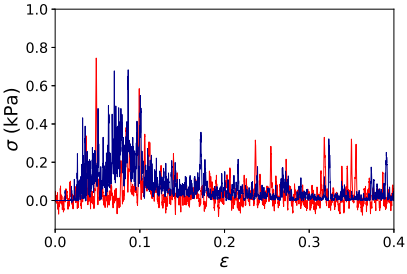

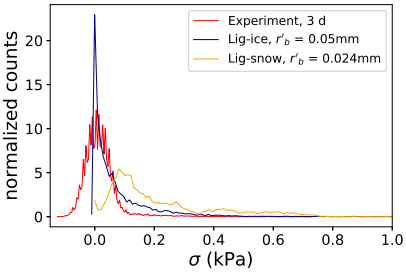

Five day sintering samples

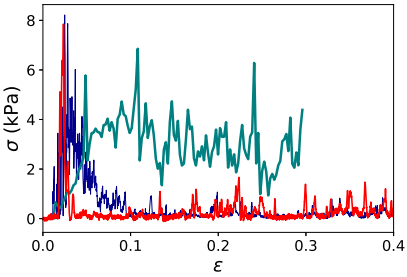

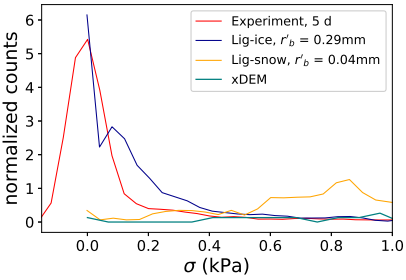

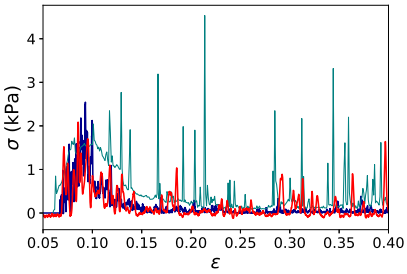

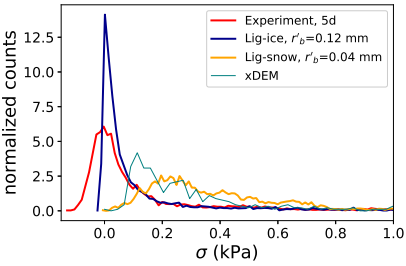

Ten day sintering samples

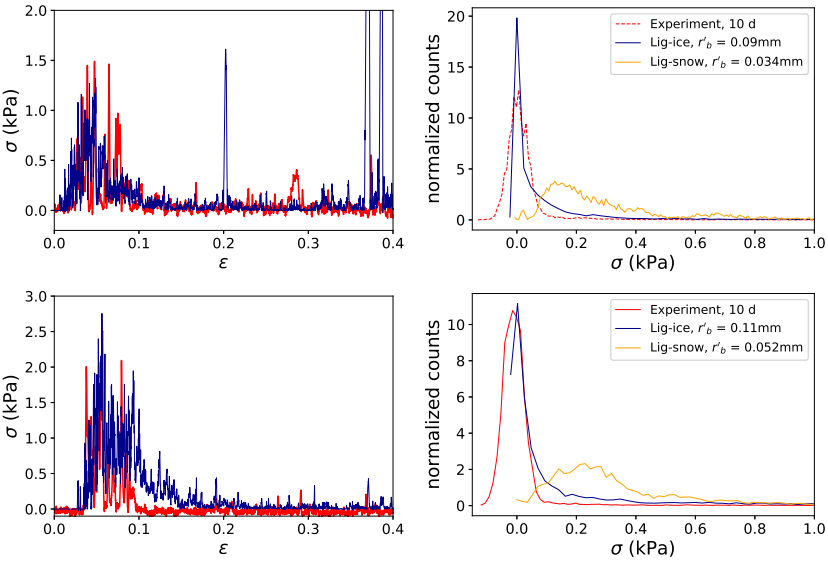

6.6.2 Bond size distribution

Measured bond size distribution in the *t*S2.1 sample of Chapter 5 with 2.1 mm after five days sintering.

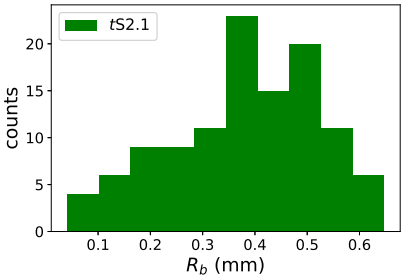

Fig. 6.10: Bond size distribution in ice bead sample.

7 Conclusion

The goal of this thesis was to advance snow micromechanics by investigating the relation of microstructural and mechanical properties in view of simulating snow mechanics with the discrete element method (DEM). Understanding fundamental micromechanical processes and the requirements of microstructure representation is essential for interpreting and predicting macroscopically observable behavior of snow. Simulating material behavior with DEM is based on the concept of particles and contacts. This concept, however, is ambiguous for natural snow and leads to a gap between experiments and DEM simulations. To bridge this gap, a new snow type consisting of spherical ice beads was designed and analyzed to enable an unambiguous representation of the microstructure in DEM. This model snow was analyzed through mechanical experiments, 3D image analysis of μCT data, and numerical simulations. The conclusions for the individual analysis steps (Chapters 3, 4, 5, and 6) allow for a summary of the thesis in the following way:

Ice beads facilitate a generic investigation of particle and contact properties and allow for a one-to-one validation of DEM models when care is taken to avoid the anomalous sintering process.

The following discussion will summarize the key findings of this thesis as they relate to DEM with focus on the particles, their shapes, and the contacts between them.

Particles, shapes, and contacts were the focus of the microstructure characterization. Thus, the objective identification of particles in the continuous 3D μCT imaged structure was the basic step for all parts of this thesis. The developed image processing routine accomplished the

particle identification with a watershed algorithm. The ice beads were taken as a reference for developing the routine, which could then also be applied to natural snow.

The shape characterization of the watershed-segmented particles confirmed high sphericity of the ice beads, the main requirement for comparison with DEM (Chapter 3.3.1). Sphericity was necessary for extracting the microstructures from the 3D μCT images of the compression samples as a list of particle positions and sizes. In this way, the experimental samples could be efficiently transferred to the DEM models (Chapter 6.2.2). While particle geometries and the adjacencies for the contact network could be successfully derived from μCT data, the size of the contacts in these weakly bonded spheres remained a problem due to insufficient image resolution. With the unknown contact sizes, one parameter remained unspecified in the DEM simulations.

The sintered contacts of the ice beads were investigated in additional experiments at higher μCT resolution, to estimate the missing parameter and shed more light on the structural evolution during sintering (Chapter 5). The image analysis revealed porously sintered bonds, a phenomenon that could be identified as a particle-size dependent instability in crystal growth. The observed porosity explained the peculiar, non-monotonic time-evolution (Chapter 5.4.3 and 3.3.4) of unconfined compressive strength of the ice bead samples, which underscores the mechanical relevance of the bonds. As a result, the detailed bond analysis not only provided an estimate of the contact sizes (Chapter 5.3.3) for the comparison with the simulated bond sizes in DEM, but also suggested a remedy (Chapter 5.4.2) for avoiding bond porosity in future ice bead experiments (detailed in the Outlook in Chapter 8).

Overall, the particle-based 3D μCT image analyses significantly contributed to understanding the experimental observations by quantifying the microstructure as particles in contact with each other, with defined sizes and shapes. This was key to understanding the mechanical behavior of snow in the sintered (Chapter 3) and in the granular states (Chapter 4), and was the basis for the microstructure representation in DEM (Chapter 6).

The contact network: key to the sintered state. The ultimate comparison of ice bead snow with DEM simulations was conducted on the sintered state in unconfined compression experiments and revealed

the importance of the size and configuration of the bonds that form the contact network (Chapter 6).

The bond sizes had to be adapted in the simulations to match the peak stresses of the experiments, since they could not be derived from the μCT images of the compression samples. However, the bond size, if determined by fitting the peak stress, yielded realistic values, as confirmed by the comparison with the additional contact characterization (Chapter 6.3.1). From the simulations of six ice bead samples, we observed an increasing relation of bond size and compressive strength. The experimental scatter in the compressive strength thus translates to a scatter in the bond sizes with realistic values (c.f. Fig. 3.9 and 6.5). The experimental scatter was originally attributed to microstructural variations between the samples, i.e. presumed differences in the sample-to-sample variations in particle positions. However, the simulations were performed with the same particle configurations as in the experiments, but led to a similar scatter only if different bond sizes were used. This implies that the scatter might rather originate from inhomogeneity in the sintered contacts.

The configuration of the bonds was crucial for reproducing the typical fracture pattern of the ice bead samples. In the experiments, the compressive behavior was dominated by the fracture of stress-chains leading to clustered particle fragments. Similar behavior in the simulations could be obtained only if the bonds were exactly inferred from the μCT images and parametrized with realistic material properties of ice. Fulfilling these conditions in the simulated microstructures resulted in stress-strain curves and stress distributions that were similar to the experimental ones (Fig. 6.3 and 6.4). These results are robust under different variations of other bond material parameters (Fig. 6.7).

The comparison of simulations of the ice bead compression experiments with two DEM models (in three configurations) showed that very detailed bond network representation is necessary for model validation. If microstructures are adequately represented and parametrized with the true mechanical properties of ice, the experimental key features can be reproduced.

Grain shape: key to the granular state. The granular state of snow was characterized in angle of repose experiments with different snow types (Chapter 4). Differences between ice beads and natural snow

in the angle of repose experiments highlighted the importance of particle shape. Shape parameters were found that reliably predicted these differences for the investigated snow types (Fig. 4.6).

In contrast to the large differences in mechanical behavior observed for natural snow types in the sintered state (Fig. 6.2 and 6.9), the experiments in the granular state showed only minor differences between these snow types (Fig. 4.4). Though surprising at the first sight, this is consistent with the shape parameter which was found to be similar for the natural snow types in the granular state. In the sintered state, grain shape seems to play a minor role besides the contact network (if the contacts can be simulated adequately). However, the contact formation depends on grain shapes. This is indicated in the observed effect of sintering on the angle of repose that varied with snow types (Fig. 4.6).

The angle of repose experiments showed that grain shape and fast sintering affect the flowability of snow equally. How grain shape affects sintering could not be resolved in the experiments.

Towards simulating natural snow. In this thesis, the mechanical behavior and microstructural characteristics of the ice beads were always investigated alongside with natural snow in the sintered and granular states. Grain shape was considered only in granular snow, while the contact network was analyzed only for sintered snow. Natural snow types could be consistently compared to ice beads for granular snow, through the shape parameters. For sintered snow a consistent comparison would require to carry out the watershed-based computation of the contact network (including contact size) on the natural snow types. If the DEM bond parameters would be adapted accordingly (while still using spherical DEM-particles) it is expected that further differences in the observed compression curves (Fig. 6.9) between ice beads and different snow types could be explained. It is, however, also expected that it would be required to translate the shape parameter into an "effective" particle friction parameter, to consistently predict the sintered and granular behavior of natural snow within a sphere-based DEM model.

8 Outlook

Through mechanical and structural analyses of the ice beads, their performance and limitations as model snow were investigated. Although limitations were found in the unexpected porosity of their sintered bonds, the ice beads are clearly promising for investigations of generalized microstructures and validation of numerical models. While the present work focused on the experimental characterization of the ice beads, the first comparison to DEM simulations demands further numerical studies which, in turn, may benefit from further experiments.

Suggestions for further experiments. Both the aim to achieve a microstructure-based one-to-one comparison of experiment and simulation, and the general interest in studying microstructural and mechanical properties of snow motivate further experiments.

In view of an improved one-to-one comparison of DEM with experiments, well-constrained microstructural parameters are essential. The unexpected porosity of the sintered bonds between ice beads led to a remaining microstructural uncertainty. To overcome this limitation, the bond porosity was investigated and found to occur only if particles are larger than a critical particle size. With this information, microstructural uncertainty can be further reduced. Choosing ice bead sizes that support sintering of solid bonds would allow for determining the bond size, the last free microstructural parameter in ice bead samples. By fully controlling the main (and unambiguously defined) microstructural parameters, their interrelations and their influence on macroscopic behavior can be examined, and all model parameters would be predefined.

In view of the general understanding of microstructural and mechanical properties of snow, the ice beads also provide new opportunities. As shown in this thesis, the bond network constitutes a crucial part of

the microstructure (Chapter 6). It is defined by the number and size of bonds. These parameters can be manipulated in the experiments, as shown in the structural analysis of the ice bead samples (Chapter 3.3.2). By creating variation in these microstructural bond parameters, their influence on the macroscopical behavior could experimentally be analyzed. This is crucial for advancing snow micromechanics, but is yet possible only for idealized model snow.

Microstructural variation can be further enhanced by using non-spherical model snow. In the present work, the developed tumbling method was optimized for producing spherical particles. The main goal was to obtain spheres as they have the simplest shapes and facilitate DEM validation. However, depending on the base particles filled into the tumbler, particles with non-spherical shapes can also be produced by tumbling. The ellipsoidal particles (described in Chapter 2.1.1) would form microstructures in which particles and contacts are defined and can be identified by image analysis, similar to the spherical particles. Using ellipsoidal, or spherical and ellipsoidal model snow in experiments would enhance the microstructural variation, e.g. in the numbers and sizes of contacts. The "potato snow" shown in Figure 2.2 could be used as an intermediate step to go from spheres (or ellipsoids) towards natural snow: grains can be still clearly defined, but shapes are non-spherical.

Suggestions for further simulations. The comparison of experiments and simulations can still be improved, which is promising for snow micromechanics and simulations with numerical models. In the simulations with the Liggghts-ice model, which yielded the best comparison with the experiments (Chapter 6), the noise in the compression-curves could be reduced by including also a damping in the bonds to yield a better comparison with the experiments. With this and fully constrained microstructure parameters (as suggested above) a peak-by-peak comparison of the compression tests seems feasible. This would allow to investigate the roles of friction, sintering, and particle shape in the post-peak-regime with snow in the granular state. Distinguishing these factors is necessary to decide if sintering during (sub-)second contact times needs to be taken into account, and whether non-spherical particle shapes can be empirically accounted for by a rolling friction parameter or need a more detailed representation. Moreover, the sensitivity of the simulations to structural changes could be examined. Gaining profound

knowledge and control of these influencing factors is essential for finally simulating natural snow with simplified microstructures of spheres, as discussed at the end of Chapter 7.

In this thesis, ice beads were used for snow mechanical investigations and model validation. But ice beads might also serve as an interesting, experimental system for other applications in snow, for example, for investigating optical properties, where sphere based models are still widely used.

References

[1] Adams, E., S. M. Jepsen, and B. Close (2008), "A bonding process between grains in mechanically disaggregated snow," Annals of Glaciology **48**, 6–12.

[2] Akitaya, E. (1974), "Studies on depth hoar," Contributions of the Institute of Low Temperature Science, Hokkaido University **26**, 1–67.

[3] Al-Hashemi, H., and O. Al-Amoudi (2018), "A review on the angle of repose of granular materials," Powder Technology **330**, 397–417.

[4] Albert, R., I. Albert, D. Hornbaker, P. Schiffer, and A.-L. Barabási (1997), "Maximum angle of stability in wet and dry spherical granular media," Phys. Rev. E **56**, R6271–R6274.

[5] Bader, H. P., R. Haeferli, E. Bucher, C. Thams, J. Neher, and O. Eckel (1939), "Der Schnee und seine Metamorphose," Kümmerly & Frey, Zürich .

[6] Bartelt, P., and M. Lehning (2002), "A physical snowpack model for the swiss avalanche warning: Part I: numerical model," Cold Regions Science and Technology **35**, 123–145.

[7] Batchelor, G. K., and R. W. O'Brien (1977), "Thermal or electrical conduction through a granular material," Proceedings of the Royal Society of London. Series A, Mathematical and Physical Sciences **355** (1682), 313–333.

[8] Blackford, J. R. (2007), "Sintering and microstructure of ice: a review," Journal of Physics D: Applied Physics **40** (21), R355–R385.

[9] Bobillier, G., B. Bergfeld, A. Capelli, J. Dual, J. Gaume, A. van Herwijnen, and J. Schweizer (2020), "Micromechanical modeling of snow failure," The Cryosphere **14**, 39–49.

[10] Botz, J., C. Loudon, J. Barger, J. Olafsen, and D. Steeples (2003), "Effects of slope and particle size on ant locomotion: Implications for choice of substrate by antlions," Journal of the Kansas Entomological Society **76**, 426–435.

[11] Brzoska, J.-B., C. Coleou, S. Borel, O. Brissaud, W. Ludwig, E. Boller, and J. Baruchel (1999), "3d visualization of snow samples by microtomography at low temperatures," ESRF Newsletter (April), 2–3.

[12] Capelli, A., I. Reiweger, and J. Schweizer (2019), "Modelling snow failure behavior and concurrent acoustic emissions signatures with a fiber bundle model," Geophysical Research Letters **46** (12), 6653–6662.

[13] Capelli, A., I. Reiweger, and J. Schweizer (2020), "Studying snow failure with fiber bundle models," Frontiers in Physics **8**, 236.

[14] Chandel, C., P. K. Srivastava, and P. Mahajan (2014), "Micromechanical analysis of deformation of snow using x-ray tomography," Cold Regions Science and Technology **101**, 14 – 23.

[15] Chen, S., and I. Baker (2010), "Structural evolution during ice-sphere sintering," Hydrological Processes **24** (14), 2034–2040.

[16] Chen, S., I. Baker, and H. Frost (2013), "Surface instability and mass transfer during the bonding of ice spheres," Philosophical Magazine **93**, 3177–3193.

[17] Cundall, P. A. (1971), "A computer model for simulating progressive large scale movements in blocky rock systems," Proceedings Symposium Int. Soc. Rock Mechanics, Nancy **1**, Paper II–8.

[18] Dahmen, K. A., J. T. Uhl, and Y. Ben-Zion (2011), "A simple analytic theory for the statistics of avalanches in sheared granular materials," Nature Physics **7**, 554–557.

[19] Doeppenschmidt, A., and H.-J. Butt (2000), "Measuring the thickness of the liquid-like layer on ice surfaces with atomic force microscopy," Langmuir **16** (16), 6709–6714.

[20] Duval, P., and E. M. Schulson (2009), *Creep and Fracture of Ice* (Cambridge University Press, Cambridge).

[21] Fierz, C., R. Armstrong, Y. Durand, P. Etchevers, E. Greene, D. McClung, K. Nishimura, P. Satyawali, and S. Sokratov (2009), *The International Classification for Seasonal Snow on the Ground*, IHP-VI Technical Documents in hydrology (UNESCO/IHP).

[22] Filhol, S., and M. Sturm (2019), "The smoothing of landscapes during snowfall with no wind," Journal of Glaciology **65** (250), 173–187.

[23] Frankowski, P., and M. Morgeneyer (2013), "Calibration and validation of DEM rolling and sliding friction coefficients in angle of repose and shear measurements," AIP Conference Proceedings **1542** (1), 851–854.

[24] Fukue, M. (1979), "Mechanical performance of snow under loading," Technical report, Tokai University Press .

[25] Garboczi, E. (1998), "Finite element and finite diierence programs for computing the linear electric and elastic properties of digital images of random materials," Report NISTIR, Gaithersburg, MD: National Institute for Standards and Technology, U.S. Department of Commerce .

[26] Gaume, J., A. van Herwijnen, G. Chambon, K. W. Birkeland, and J. Schweizer (2015), "Modeling of crack propagation in weak snowpack layers using the discrete element method," The Cryosphere **9** (5), 1915–1932.

[27] Gaume, J., A. van Herwijnen, G. Chambon, N. Wever, and J. Schweizer (2017), "Snow fracture in relation to slab avalanche release: critical state for the onset of crack propagation," The Cryosphere **11** (1), 217–228.

[28] Gaume, J., H. Löwe, S. Tan, and L. Tsang (2017), "Scaling laws for the mechanics of loose and cohesive granular materials based on baxter's sticky hard spheres," Phys. Rev. E **96**, 032914.

[29] Gerling, B., H. Löwe, and A. van Herwijnen (2017), "Measuring the elastic modulus of snow," Geophysical Research Letters **44** (21), 11,088–11,096.

[30] German, R. (1996), *Sintering Theory and Practice* (Wiley).

[31] Gillespie, L. K. (2007), *Mass Finishing Handbook* (Industrial Press).

[32] Gubler, H. (1982), "Strength of bonds between ice grains after short contact times," Journal of Glaciology **28** (100), 457–473.

[33] Hagenmuller, P., N. Calonne, G. Chambon, F. Flin, C. Geindreau, and M. Naaim (2014), "Characterization of the snow microstructural bonding system through the minimum cut density," Cold Regions Science and Technology **108**, 72 – 79.

[34] Hagenmuller, P., G. Chambon, F. Flin, S. Morin, and M. Naaim (2014), "Snow as a granular material: Assessment of a new grain segmentation algorithm," Granular Matter **16**, 421–432.

[35] Hagenmuller, P., G. Chambon, B. Lesaffre, F. Flin, and M. Naaim (2013), "Energy-based binary segmentation of snow microtomographic images," Journal of Glaciology **59** (217), 859–873.

[36] Hagenmuller, P., G. Chambon, and M. Naaim (2015), "Microstructure-based modeling of snow mechanics: A discrete element approach," Cryosphere **9** (5), 1969–1982.

[37] Hagenmuller, P., M. Matzl, G. Chambon, and M. Schneebeli (2016), "Sensitivity of snow density and specific surface area measured by microtomography to different image processing algorithms," The Cryosphere **10** (3), 1039–1054.

[38] Hagenmuller, P., T. C. Theile, and M. Schneebeli (2014), "Numerical simulation of microstructural damage and tensile strength of snow," Geophysical Research Letters **41** (1), 86–89.

[39] Hansen, A., and R. Brown (1986), "The granular structure of snow: An internal-state variable approach," Journal of Glaciology **32**, 434–438.

[40] Hertz, H. (1882), "Über die Berührung fester elastischer Körper," Journal für die Reine und Angewandte Mathematik **1882** (92), 156–171.

[41] Herwijnen, A. v., and D. A. Miller (2013), "Experimental and numerical investigation of the sintering rate of snow," Journal of Glaciology **59** (214), 269–274.

[42] Hildebrand, T., A. Laib, R. Müller, J. Dequeker, and P. Rüegsegger (1999), "Direct three-dimensional morphometric analysis of human cancellous bone: Microstructural data from spine, femur, iliac crest, and calcaneus," Journal of Bone and Mineral Research **14** (7), 1167–1174.

[43] Hobbs, P. V., and B. J. Mason (1964), "The sintering and adhesion of ice," Philosophical Magazine **9** (98), 181–197.

[44] Jellinek, H. (1967), "Liquid-like (transition) layer on ice," Journal of Colloid and Interface Science **25** (2), 192 – 205.

[45] Jellinek, H. H. G. (1959), "Compressive strength properties of snow," Journal of Glaciology **3** (25), 345–354.

[46] Johnson, J. B., and M. A. Hopkins (2005), "Identifying microstructural deformation mechanisms in snow using discrete-element modeling," Journal of Glaciology **51** (174), 432–442.

[47] Johnson, J. B., and M. Schneebeli (1999), "Characterizing the microstuctural and micromechanical properties of snow," Cold Regions Science and Technology **30**, 91–100.

[48] Kabore, B. (2020), "Microstructure-based multiscale modeling of mechanical response for materials with complex microstructures," Thesis, University of Luxembourg .

[49] Kabore, B., and B. Peters (2019), "Micromechanical model for sintering and damage in viscoelastic porous ice and snow. part II:

Validation," International Journal of Solids and Structures **185-186**, 281–291.

[50] Kabore, B. W., and B. Peters (2020), "Micromechanical model for sintering and damage in viscoelastic porous ice and snow. part I: Model and calibration," International Journal of Solids and Structures **185-186**, 324 – 333.

[51] Kaempfer, T., and M. Plapp (2009), "Phase-field modeling of dry snow metamorphism," Physical review. E, Statistical, nonlinear, and soft matter physics **79**, 031502.

[52] Kaempfer, T., M. Schneebeli, and S. Sokratov (2005), "A microstructural approach to model heat transfer in snow," Geophysical Research Letters **32**, L21503 1–L21503 5.

[53] Kaempfer, T. U., M. A. Hopkins, and D. K. Perovich (2007), "A three-dimensional microstructure-based photon-tracking model of radiative transfer in snow," Journal of Geophysical Research: Atmospheres **112** (D24), 1–14.

[54] Kingery, D. W. (1960), "Regelation, surface diffusion, and ice sintering," Journal of Applied Physics **31**, 833 – 838.

[55] Kirchner, H. K., G. Michot, H. Narita, and T. Suzuki (2001), "Snow as a foam of ice: Plasticity, fracture and the brittle-to-ductile transition," Philosophical Magazine A **81** (9), 2161–2181.

[56] Kloss, C., C. Goniva, A. Hager, S. Amberger, and S. Pirker (2012), "Models, algorithms and validation for open source DEM and CFD-DEM," Prog. Comput. Fluid Dyniamics **12**, 140.

[57] Köchle, B., and M. Schneebeli (2014), "Three-dimensional microstructure and numerical calculation of elastic properties of alpine snow with a focus on weak layers," Journal of Glaciology **60** (222), 705–713.

[58] Köhler, A., J.-T. Fischer, R. Scandroglio, M. Bavay, J. Mcelwaine, and B. Sovilla (2018), "Cold-to-warm flow regime transition in snow avalanches," The Cryosphere **12**, 3759–3774.

[59] Krol, Q., and H. Löwe (2016), "Analysis of local ice crystal growth in snow," Journal of Glaciology **62** (232), 378–390.

[60] Kry, P. R. (1975), "The relationship between the visco-elastic and structural properties of fine-grained snow," Journal of Glaciology **14** (72), 479–500.

[61] Kuczynski, G. (1949), "Self-diffusion in sintering of metallic particles," Transactions of the American Institute of Mining and Metallurgical Engineers **185** (2), 169–178.

[62] Kuroiwa, D. (1961), "A study of ice sintering," Tellus **13** (2), 252–259.

[63] Kuroiwa, D., Y. Mizuno, and M. Takeuchi (1967), "Micromeritical properties of snow," Physics of Snow and Ice (1(2)), 751–772.

[64] Kyburz, M., B. Sovilla, J. Gaume, and C. Ancey (2020), "Decoupling the role of inertia, friction and cohesion in dense granular avalanche pressure build-up on obstacles," Journal of Geophysical Research: Earth Surface **125** (2), e2019JF005192.

[65] Landauer, J., M. Kuhn, D. S. Nasato, P. Foerst, and H. Briesen (2020), "Particle shape matters – using 3D printed particles to investigate fundamental particle and packing properties," Powder Technology **361**, 711 – 718.

[66] Langlois, A., A. Royer, B. Montpetit, A. Roy, and M. Durocher (2020), "Presenting snow grain size and shape distributions in northern canada using a new photographic device allowing 2D and 3D representation of snow grains," Frontiers in Earth Science **7**, 347.

[67] Lever, J. H., S. Taylor, G. R. Hoch, and C. Daghlian (2019), "Evidence that abrasion can govern snow kinetic friction," Journal of Glaciology **65** (249), 68–84.

[68] Libbrecht, K. (2003), "Growth rates of the principal facets of ice between -10°C and -40°C," Journal of Crystal Growth **247** (3), 530 – 540.

[69] Libbrecht, K. (2005), "The physics of snow crystals," Rep. Prog. Phys. **68**, 10.1088/0034-4885/68/4/R03.

[70] Louchev, O. A. (1994), "Diffusion, heat transfer, equilibrium molecular density and kinetic mechanism of morphological instability in physical vapor deposition," Journal of Crystal Growth **140** (1), 219 – 236.

[71] Löwe, H., F. Riche, and M. Schneebeli (2013), "A general treatment of snow microstructure exemplified by an improved relation for thermal conductivity," The Cryosphere **7** (5), 1473–1480.

[72] Löwe, H., and A. van Herwijnen (2012), "A poisson shot noise model for micro-penetration of snow," Cold Regions Science and Technology **70**, 62 – 70.

[73] Löwe, H., M. Zaiser, S. Mösinger, and S. Schleef (2020), "Snow mechanics near the ductile-brittle transition: Compressive stick-slip and snow microquakes," Geophysical Research Letters **47** (4), e2019GL085491.

[74] McGlinchey, D. (2005), *Characterisation of bulk solids* (Blackwell and CRC Press, Oxford and Boca Raton, Cambridge).

[75] Mede, T., G. Chambon, P. Hagenmuller, and F. Nicot (2018), "A medial axis based method for irregular grain shape representation in DEM simulations," Granular Matter **20**, 16.

[76] Mede, T., G. Chambon, P. Hagenmuller, and F. Nicot (2018), "Snow failure modes under mixed loading," Geophysical Research Letters **45** (24), 13,351–13,358.

[77] Mede, T., G. Chambon, F. Nicot, and P. Hagenmuller (2020), "Micromechanical investigation of snow failure under mixed-mode loading," International Journal of Solids and Structures **199**, 95 – 108.

[78] Mellor, M. (1975), "A review of basic snow mechanics," IASH pub **114**, 251–291.

[79] Michael, M. (2014), "A discrete approach to describe the kinematics between snow and a tire tread," Thesis, University of Luxembourg .

[80] Michael, M., F. Nicot, and B. Peters (2015), "Advanced micromechanical description of snow behaviour — part I — mechanical and numerical modelling," Preprint submitted to International Journal of Solids and Structures .

[81] Miyazaki, K. (2015), "Diffusion-controlled growth and degree of disequilibrium of garnet porphyroblasts: is diffusion-controlled growth of porphyroblasts common?" Progress in Earth and Planetary Science **2** (25), 313–333.

[82] Molaro, J. L., M. Choukroun, C. B. Phillips, E. S. Phelps, R. Hodyss, K. L. Mitchell, J. M. Lora, and G. Meirion-Griffith (2019), "The microstructural evolution of water ice in the solar system through sintering," Journal of Geophysical Research: Planets **124** (2), 243–277.

[83] Mulak, D., and J. Gaume (2019), "Numerical investigation of the mixed-mode failure of snow," Computational Mechanics **6**, 439–447.

[84] Mullins, W. W., and R. F. Sekerka (1963), "Morphological stability of a particle growing by diffusion or heat flow," Journal of Applied Physics **34** (2), 323–329.

[85] Mullins, W. W., and R. F. Sekerka (1964), "Stability of a planar interface during solidification of a dilute binary alloy," Journal of Applied Physics **35** (2), 444–451.

[86] Narita, H. (1984), "An experimental study on tensile fracture of snow," Contributions from the Institute of Low Temperature Science **32**, 1–37.

[87] Nowak, S., A. Samadani, and A. Kudrolli (2005), "Maximum angle of stability of a wet granular pile," Nature Physics **1**, 50–52.

[88] Peinke, I., P. Hagenmuller, E. Andò, G. Chambon, F. Flin, and J. Roulle (2020), "Experimental study of cone penetration in snow using x-ray tomography," Frontiers in Earth Science **8**, 63.

[89] Peinke, I., P. Hagenmuller, G. Chambon, and J. Roulle (2019), "Investigation of snow sintering at microstructural scale from micro-penetration tests," Cold Regions Science and Technology **162**, 43–55.

[90] Petrovic, J. J. (2003), "Review mechanical properties of ice and snow," Journal of Materials Science **38**, 1–6.

[91] Pinzer, B., A. Medebach, H. Limbach, C. Dubois, M. Stampanoni, and M. Schneebeli (2012), "3D-characterization of three-phase systems using x-ray tomography: Tracking the microstructural evolution in ice cream," Soft Matter **8**, 4584–4594.

[92] Pinzer, B. R., M. Schneebeli, and T. U. Kaempfer (2012), "Vapor flux and recrystallization during dry snow metamorphism under a steady temperature gradient as observed by time-lapse microtomography," The Cryosphere **6** (5), 1141–1155.

[93] Pittenger, B., S. Fain, M. Cochran, J. Donev, B. Robertson, A. Szuchmacher, and R. Overney (2000), "Premelting at ice-solid interfaces studied via velocity-dependent indentation with force microscope tips," Physical Review B **6320**, 134102.

[94] Potyondy, D., and P. Cundall (2004), "A bonded-particle model for rock," International Journal of Rock Mechanics and Mining Sciences **41** (8), 1329 – 1364.

[95] Proksch, M., H. Löwe, and M. Schneebeli (2015), "Density, specific surface area, and correlation length of snow measured by high-resolution penetrometry," Journal of Geophysical Research F: Earth Surface **120** (2), 346–362.

[96] Rackl, M., F. Grötsch, and W. A Günthner (2017), "Angle of repose revisited: When is a heap a cone?" EPJ Web of Conferences **140**, 02002.

[97] Riche, F., M. Schneebeli, and S. Tschanz (2012), "Design-based stereology to quantify structural properties of artificial and natural snow using thin sections," Cold Regions Science and Technology **s 79–80**, 67–74.

[98] Roch, A. (1966), "Les variations de la resistance de la neige," IAHS Publ. **69**, 86–99.

[99] Salm, B. (1982), "Mechanical properties of snow," Reviews of Geophysics **20** (1), 1–19.

[100] Schaible, M., R. Johnson, L. Zhigilei, and S. Piqueux (2017), "High energy electron sintering of icy regoliths: Formation of the pacman thermal anomalies on the icy saturnian moons," Icarus **285**, 211 – 223.

[101] Schleef, S., M. Jaggi, H. Löwe, and M. Schneebeli (2014), "Instruments and methods: An improved machine to produce nature-identical snow in the laboratory," Journal of Glaciology **60** (219), 94–102.

[102] Schneebeli, M. (2004), "Numerical simulation of elastic stress in the microstructure of snow," Annals of Glaciology **38**, 339–342.

[103] Schweizer, J. (1998), "Laboratory experiments on shear failure of snow," Annals of Glaciology **26**, 97–102.

[104] Schweizer, J., S. Bellaire, C. Fierz, M. Lehning, and C. Pielmeier (2006), "Evaluating and improving the stability predictions of the snow cover model snowpack," Cold Regions Science and Technology **46** (1), 52 – 59.

[105] Shapiro, L. H., J. B. Johnson, M. Sturm, and G. L. Blaisdell (1997), "Snow mechanics:review of the state of knowledge and applications," World Wide Web Internet And Web Information Systems , 40.

[106] Shertzer, R. H., and E. E. Adams (2011), "Anisotropic thermal conductivity model for dry snow," Cold Regions Science and Technology **69** (2), 122 – 128.

[107] Shmulik, P. F., and D. A. Robinson (2002), "Particle shape characterization using angle of repose measurements for predicting the effective permittivity and electrical conductivity of saturated granular media," Water Resources Research **38** (11), 18–1–18–11.

[108] Shreve, R. L. (1967), "Migration of air bubbles, vapor figures, and brine pockers in ice under a temperature gradient," Journal of Geophysical Research (1896-1977) **72** (16), 4093–4100.

[109] Sman, R. v. d., A. Voda, G. van Dalen, and A. Duijster (2013), "Ice crystal interspacing in frozen foods," Journal of Food Engineering **116** (2), 622 – 626.

[110] Spettl, A., S. Bachstein, M. Dosta, M. Goslinska, S. Heinrich, and V. Schmidt (2016), "Bonded-particle extraction and stochastic modeling of internal agglomerate structures," Advanced Powder Technology **27** (4), 1761 – 1774.

[111] Srivastava, P. K., C. Chandel, P. Mahajan, and P. Pankaj (2016), "Prediction of anisotropic elastic properties of snow from its microstructure," Cold Regions Science and Technology **125**, 85 – 100.

[112] Steinkogler, W., J. Gaume, H. Loewe, B. Sovilla, and M. Lehning (2015), "Granulation of snow: From tumbler experiments to discrete element simulations," Journal of Geophysical Research - Earth Surface **120** (6), 1107–1126.

[113] Style, R. W., and M. G. Worster (2010), "Linear stability of a solid-vapour interface," Proceedings of the Royal Society A: Mathematical, Physical and Engineering Sciences **466** (2116), 1005–1025.

[114] Szabo, D., and M. Schneebeli (2007), "Subsecond sintering of ice," Applied Physics Letters **90** (15), 3–5.

[115] Theile, T., H. Löwe, T. Theile, and M. Schneebeli (2011), "Simulating creep of snow based on microstructure and the anisotropic deformation of ice," Acta Materialia **59** (18), 7104 – 7113.

[116] Theile, T., and M. Schneebeli (2011), "Algorithm to decompose three-dimensional complex structures at the necks: Tested on snow structures," Image Processing, IET **5**, 132 – 140.

[117] Theile, T., D. Szabo, A. Luthi, H. Rhyner, and M. Schneebeli (2009), "Mechanics of the ski–snow contact," Tribology Letters **36** (3), 223–231.

[118] Theile, T., D. Szabo, C. Willibald, and M. Schneebeli (2020), "Discrete element model for high strain rate deformations of snow," arXiv:2007.01694 [physics.geo-ph] .

[119] Voitkovsky, K. F., A. N. Bozhinsky, V. N. Golubev, M. N. Laptev, A.-A. Zhigulsky, and Y. Y. Slesarenko (1975), "Creep-induced changes in structure and density of snow," Symposium on snow mechanics, Grindelwald 1974 .

[120] Wadell, H. (1935), "Volume, shape, and roundness of quartz particles," The Journal of Geology **43** (3), 250–280.

[121] Wang, X., and I. Baker (2013), "Observation of the microstructural evolution of snow under uniaxial compression using x-ray computed microtomography," Journal of Geophysical Research: Atmospheres **118** (22), 12,371–12,382.

[122] Wang, X., and I. Baker (2017), "Comparison of the effects of unidirectional and sign-alternating temperature gradients on the sintering of ice spheres," Hydrological Processes **31** (4), 871–879.

[123] Warren, S. G. (1982), "Optical properties of snow," Reviews of Geophysics **20** (1), 67–89.

[124] Wautier, A., C. Geindreau, and F. Flin (2015), "Linking snow microstructure to its macroscopic elastic stiffness tensor: A numerical homogenization method and its application to 3-d images from x-ray tomography," Geophysical Research Letters **42** (19), 8031–8041.

[125] Wensrich, C. M., and A. Katterfeld (2012), "Rolling friction as a technique for modelling particle shape in DEM," Powder Technology **217**, 409 – 417.

[126] Wiacek, J., and M. Molenda (2016), "Representative elementary volume analysis of polydisperse granular packings using discrete element method," Particuology **27**, 88 – 94.

[127] Wiese, M., and M. Schneebeli (2017), "Snowbreeder 5: A micro-ct device for measuring the snow-microstructure evolution under the simultaneous influence of a temperature gradient and compaction," Journal of Glaciology **63**, 1–6.

[128] Willibald, C., H. Löwe, T. Theile, J. Dual, and M. Schneebeli (2020), "Angle of repose experiments with snow: role of grain shape and cohesion," Journal of Glaciology **66** (258), 658–666.

[129] Willibald, C., S. Scheuber, H. Löwe, J. Dual, and M. Schneebeli (2019), "Ice spheres as model snow: Tumbling, sintering, and mechanical tests," Frontiers in Earth Science **7**, 229.

[130] Wolfsperger, F., H. Rhyner, and M. Schneebeli (2019), *Slope preparation and grooming. A handbook for practitioners* (WSL Institute for Snow and Avalanche Research SLF).

[131] Zhou, Y. C., B. H. Xu, A. B. Yu, and P. Zulli (2001), "Numerical investigation of the angle of repose of monosized spheres," Phys. Rev. E **64**, 021301.

Acknowledgments

This PhD has been a new kind of "adventure in snow" for me. After four years, I am still convinced that no other material would have been better to investigate during a PhD. I am grateful for this opportunity and for the support of many people who were involved in this adventure.

Although he appeared last in this story, I first want to thank Henning Löwe, as supervisor of this thesis during the last two and most exciting years. Thank you for your great support, for developing ideas and clarifying questions in our countless discussions - I appreciate to learn from and with you about snow, physics, and scientific working. It was great to have freedom in the choice of topics and research questions, but with someone at the side who sees a "bigger picture".

Martin Schneebeli offered me this opportunity in the first place and has been there during the four years. Thank you for inviting me into the team and supporting me so generously, as a patient supervisor, with conferences and workshops. The discussions with you and your enthusiasm about snow inspired and motivated me throughout the years.

I am grateful for the support of my supervisor at the ETH, Jürg Dual, who has also been there from the beginning on with helpful input and interesting discussions.

Thank you to Johan Gaume for the interest in my work and for accepting to be part of my committee.

Thiemo Theile welcomed me at the SLF, introduced me to the topic and showed interest in my work even after his time at the SLF. Denes Szabo introduced me to Liggghts. Thank you!

Thanks to all the people that make working at SLF so pleasant, with the workshop and house services, good coffee and lunch breaks. In particular, I would like to thank the snow physics team in all its different shapes. Jaggi, if not at the poles, was there throughout the years and

helped by knowing and finding everything in the lab! Thanks to Margret who introduced me patiently to the μCT. Sophia came to the team to do her Master's thesis within my project - I am grateful for her trust and help. Michael was not only a great office-mate, but also greatly helped me by proof-reading this thesis - thanks a lot!

Adu, you had various, and also very contrasting roles in this adventure. During times of home-office, you were an awesome office-mate and IT support (providing technology for easy backups that let me sleep better at night!). Thank you for your help in reading parts of this manuscript, for so many inspiring discussions, for encouraging me. Thank you also for letting me forget my work, for smiling at me, for cooking deliciously again and again, for coming in the snow with me.

Thanks to my Freiburg-physics-crew for their support and encouragement. It was great to study together with you and learn to laugh about spherical cows in vacuum.

Thanks to my family and in particular my grandmothers for supporting me on this long, long way.

Davos, January 2021 *Carolin*